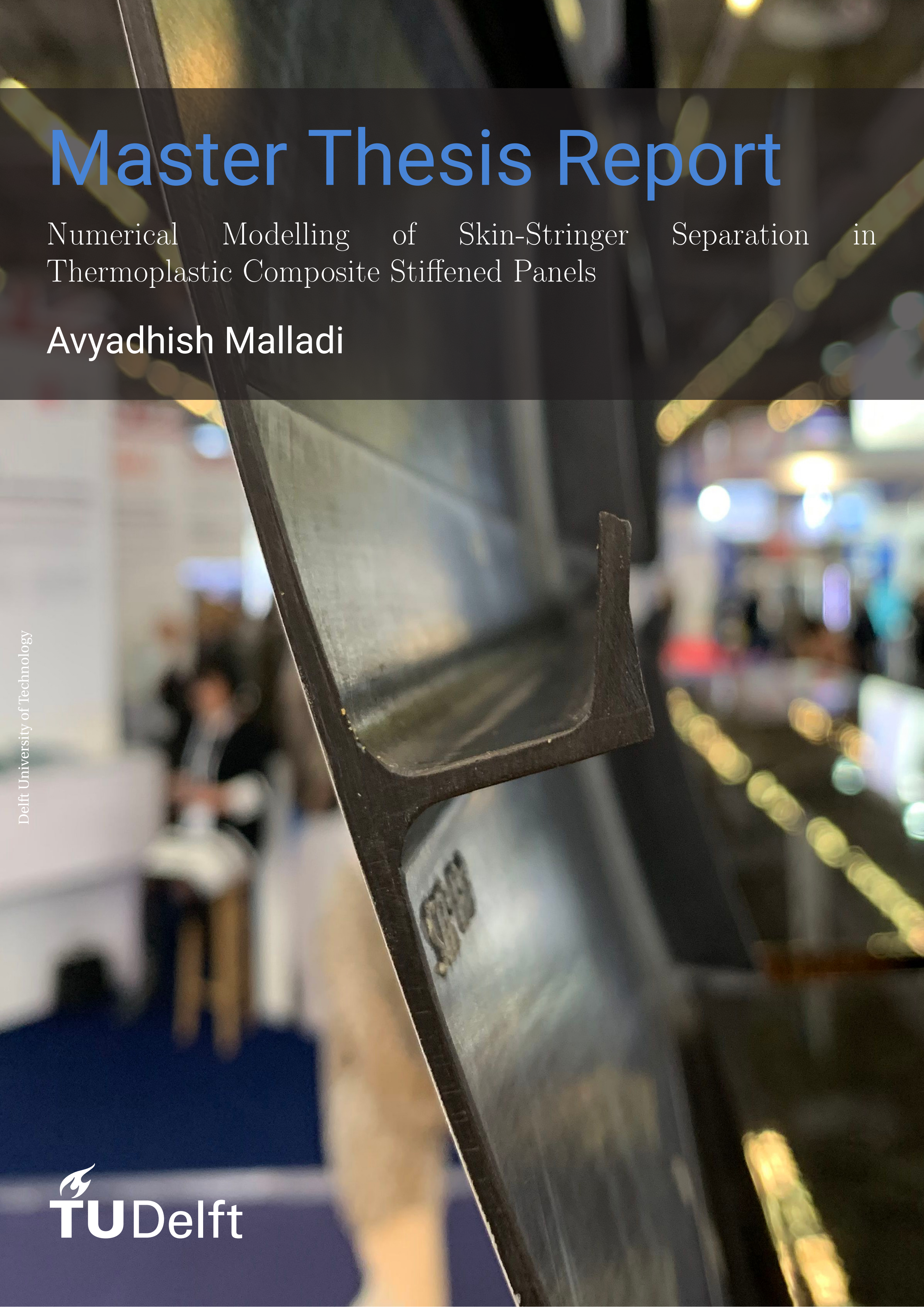

Master Thesis Report

Numerical Modelling of Skin-Stringer Separation in Thermoplastic Composite Stiffened Panels

Avyadhish Malladi

Delft University of Technology

Master Thesis Report

Numerical Modelling of Skin-Stringer Separation in Thermoplastic Composite Stiffened Panels

Author:	Avyadhish Malladi - 5509599
Course:	Master of Science Thesis
Institution:	Delft University of Technology
Place:	Faculty of Aerospace Engineering, Delft
Thesis Supervisors:	Dr. Sergio Turteltaub & Dr. Chiara Bisagni
Cover Image Source:	CompositesWorld.com

Delft University of Technology
Faculty of Aerospace Engineering
Department of Aerospace Structures and Materials

GRADUATION COMMITTEE

Dated: 22-02-2024

Committee Chair:

Dr.Ir. René Alderliesten

Committee Members:

Dr. Sergio Turteltaub

Dr. Chiara Bisagni

Dr. Bianca Giovanardi

Preface

The following report presents the results of my MSc thesis, which I conducted at the Faculty of Aerospace Engineering at TU Delft. The focus of my research was to assess the effectiveness of two techniques, the Extended Finite Element Modelling (XFEM) technique, in modelling the skin-stringer separation in Thermoplastic Composite stiffened panels. This thesis report concludes my wonderful journey at TU Delft. When I decided to pursue my master's degree at TU Delft, it was to challenge myself and step out of my comfort zone. However, it turned out to be a transformative period for me. I strongly believe that this experience has helped me grow both as an engineer and as an individual in many ways.

This journey and my master's thesis would not have come to fruition without the contribution of several people. In this regard, I would like to express my heartfelt gratitude to all those who played a role in guiding and supporting me over the last two and a half years.

I want to express my sincere gratitude to my supervisors, Dr. Chiara Bisagni and Dr. Sergio Turteltaub, for their guidance throughout this project. I am grateful to Dr. Chiara Bisagni for introducing me to this topic and providing valuable feedback whenever required. I would also like to thank Dr. Sergio Turteltaub for his keen interest in my thesis project. Our interactions during our numerous meetings have not only enabled me to step out of my comfort zone but have also been crucial in dealing with the challenges involved in implementing the XFEM. Their insights were highly valuable in ensuring the completion of this thesis project. I would also like to thank Andres Pereira and Kevin van Dooren for their practical inputs during the modelling stage of this thesis project.

I want to express my gratitude towards my family for their unwavering love and support. I would also like to extend my heartfelt thanks to my friends who have supported me personally and professionally during my MSc program. The past two and a half years have been a memorable journey, and I feel fortunate to have experienced them with my friends. Their guidance and support have helped me grow and become a better person. As I approach the end of my student life, I cannot forget to acknowledge my late grandmother, Eleswarupu Pushpavati, for her unconditional love throughout my childhood and academic journey.

Delft University of Technology
February 14th, 2024

Avyadhish Malladi

Abstract

In this thesis project, the effectiveness of the Extended Finite Element Model (XFEM) approach with cohesive segments, as implemented in Abaqus, in modelling the skin-stringer separation behaviour in thermoplastic composite stiffened panels was evaluated. The interest in considering XFEM stems from its ability to model cracks along an arbitrary solution dependent. This contrasts with the widely used damage modelling techniques in literature, where the damage is modelled along a pre-defined fracture plane. Since an experimental exercise was out of scope for the purpose of this thesis study, the test results corresponding to a stiffened panel reported in the literature were taken as a reference. The reference study under consideration tested two fast crystallysing PolyEtherKetoneKetone (PEKK-FC) carbon composite panels with three stringer with an angled cap on one side. The stringers were joined to the skin using a short-fibre reinforced butt-joint and an initial delamination of 70 mm was introduced between the middle skin-stringer interface. The reference study considered Virtual Crack Closure Technique (VCCT) to model the evolution of the skin-stringer debond in the post-buckling domain. Hence, VCCT was also considered for comparison against XFEM.

Before developing the finite element models for the stiffened panel under consideration, the modelling strategy for implementing VCCT and XFEM to model delamination growth was developed using simple double cantilever beam (DCB) specimens. The results were compared with literature data. Upon developing the modelling strategy, a VCCT-based finite element model was developed for the stiffened panel under consideration. Given the lack of geometric imperfections from the test panels from the reference study, an imperfection study was carried out using the VCCT-based model by varying the fraction of mode 1 deformation introduced to the panel as imperfections. Upon finding the suitable imperfection, XFEM-based finite element models were developed for the stiffened panel under consideration using two different damage initiation criteria: (1) Quadratic Stress Criterion (QUADS) and (2) Maximum Principal Stress Criterion (MAXPS). The load-displacement curves, the post-buckling deformations, and the evolution of skin-stringer separation leading up to the final failure, predicted by the XFEM-based models, were compared with the VCCT-based model and the test results reported in the literature.

The study concluded that the XFEM-based model with the QUADS criterion predicts the post-buckling deformations and the load-displacement curve, as well as the VCCT-based model considered in the literature. Both models, XFEM (QUADS Criterion) and VCCT, underestimate the crack length at the final failure compared to the test results reported in the literature. It must be noted that the VCCT-based model predicted the crack length at the final failure closer to the test results. This, in part, could be attributed to the lack of damage initiation stress parameters utilised to define the QUADS-based damage initiation criterion used in XFEM which meant that they were approximated based on a similar material found in the literature. The XFEM-based model with the MAXPS criterion, as implemented in Abaqus, was limited in its ability to model crack growth at the skin-stringer separation. This was due to the challenges posed by the technique in modelling crack growth along multi-material interfaces wherein the crack tip would impinge on the joint interface with no further crack growth. The UDMGINI subroutine was subsequently used to define a modified MAXPS damage initiation criterion to test three different strategies to overcome the crack tip impingement problem: (1) using a user-defined fracture plane parallel to the length of the panel; (2) using a bias factor to influence the fracture plane and (3) defining an angle to deflect the crack tip when it approaches the joint interface. Only the first approach could predict the post-buckling behaviour leading to the final failure without any convergence issues, although the model significantly overestimated the final failure load. While this exercise serves as a proof of concept to use the UDMGINI subroutine to overcome the challenges presented by implementing the MAXPS damage initiation algorithm in Abaqus, the development of an algorithm rooted in physics remains to be considered for future studies. Currently, the QUADS-based criterion can be used to model cracks using XFEM with relative ease and can offer further insights into fracture development at the skin-stringer interface in a 3D space.

Contents

List of Figures

List of Tables

Glossary of Abbreviations

η	BK curve fit parameter
G_C	Mixed-mode fracture toughness
G_{IC}	Mode I fracture toughness
G_{IIC}	Mode II fracture toughness
G_{IIIC}	Mode III fracture toughness
G_{III}	Mode III SERR
G_{II}	Mode II SERR
G_I	Mode I SERR
G_T	Total energy release rate
l_{fpz}	Length of the fracture process zone
AR	Aspect Ratio
BK	Fracture criterion defined by Benzeggah and Kenane
C	Carbon
CFRP	Carbon Fibre Reinforced Polymers
CFRP	Glass Fibre Reinforced Polymers
CTE	Coefficient of Thermal Expansion
CZM	Cohesive Zone Models
DIC	Digital Image Correlation
FEM	Finite Element Models
FI	Failure Index
LATP	Laser Assisted Tape Placement
MAXPS	Maximum principal stress criterion
PEAK	Polyaryletherketone
PEEK	Polyetheretherketone
PEKK	Polyetherketoneketone
PEKK-FC	Fast Crystallising Polyetherketoneketone
QUADS	Quadratic nominal stress criterion
SERR	Strain Energy Release Rate
VCCT	Virtual Crack Closure Technique
XFEM	Extended Finite Element Models

Part I

Literature Review

1

Introduction

In the aerospace industry, the evolution of aircraft manufacturing has been marked by a shift towards composite materials. These materials offer weight-saving ability, tailor-ability, and improved specific properties. Among these, thermoplastic composites have recently gained attention due to their toughness, recyclability, and ability to achieve rivet-free joints through techniques like induction welding. However, despite the potential, the current design philosophy restricts the full utilisation of the weight-saving potential of these materials [1]. This is primarily due to the limitations of current analysis tools in accurately predicting the behaviour of composite stiffened panels, leading to their final failure. This chapter highlights the advantages of adopting thermoplastic composites for aircraft structures and provides a brief overview of the limitations presented by current analysis tools.

1.1. Thermoplastic Composites for Aerospace Structures

During the early years of aerospace manufacturing, metals were the go-to materials for aircraft structures. However, in recent times, composite materials have become increasingly popular due to their weight savings, tailor-ability, and better specific properties offered by fiber-reinforced polymer matrix materials. For instance, approximately 50% of the structural weight (excluding engines) of Airbus A350 and Boeing 787 Dreamliner is made using composite materials [2]. Although composite materials can be made using either thermosetting or thermoplastic polymer matrices, these commercial aircrafts primarily use thermoset composites. The reluctance to adopt thermoplastic matrix composites has been related to affordability [3]. Thermoplastics are more expensive than the traditionally used epoxy-resin-based thermosets. Additionally, standard epoxy resin requires processing temperatures around 180°C, but high-performance thermoplastic composites suitable for aerospace applications require processing temperatures close to 380°C [3]. Expensive tools with low Coefficients of Thermal Expansion (CTE) are necessary to facilitate the required high processing temperatures. However, with the increasing interest in developing faster manufacturing techniques and a focus on the recyclability of structures, thermoplastics have become more appealing than before.

Thermoplastic materials are highly suitable for automated processes owing to their processing advantages, like thermo-foldability and weldability. Furthermore, the use of thermoplastics allows for the application of new manufacturing techniques, such as hot press forming and induction welding, as stated in several research studies [4] [5] [6] [7] [8]. The extent of manufacturing possibilities enabled by using thermoplastic materials can be realised from Figure 1.1. Even though the material cost of thermoplastics is high if exploited well, the cost savings achieved through these processes can effectively compensate for it [3]. Additionally, thermoplastics in their fully cured state can be used as woven tapes to manufacture tailored composites using automated processes [9].

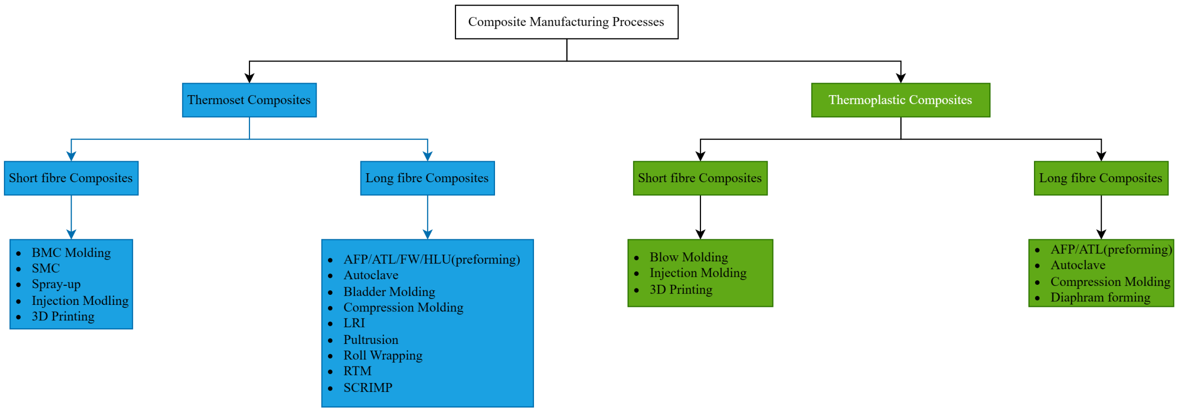

Figure 1.1: Manufacturing processes suited for thermoplastic and thermoset composites [3]

Thermoplastics can help reduce the number of assembly parts needed to manufacture complex structures. For example, skin-stiffened structures can have rivet-free joints by co-consolidating sub-parts using a filler material. For instance, Fokker Aerostructures has developed a new manufacturing method called the butt-joint technique. This method involves co-consolidating skin and stiffener laminates with injection-molded filler at the joint interface [4]. The filler is made using short carbon fibre-reinforced thermoplastic material. With conventional thermoset composites, specific flanges are first produced and then bolted, bonded or co-cured to the skin. However, specific flanges are not needed with the butt-joint technique, making manufacturing simpler and significantly less expensive (see Figure 1.2a). This technique is also suitable for high-volume manufacturing. Furthermore, using this technique eliminates the need to continue outer plies for load transfer, allowing web and flange layups to be optimised separately. Tests show that the filler joint can transfer high loads [10]. The independent tailoring of laminates used for web and flange has been found to lead to weight savings of up to 5% [11].

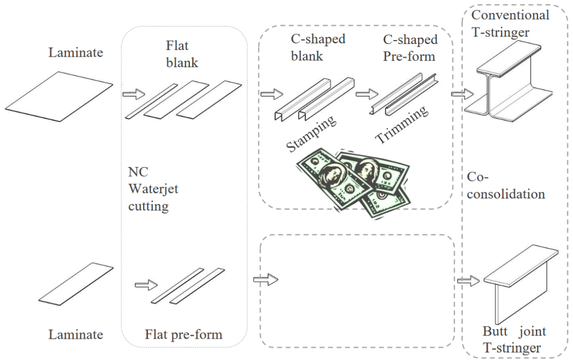

(a) Comparison of steps involved in manufacturing a stringer: Conventional approach (top); Butt-Join approach (bottom) [11]

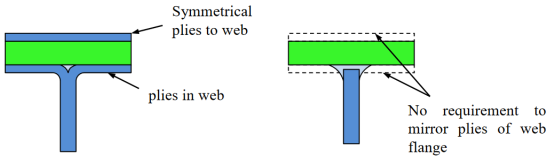

(b) Butt-joint technique: difference in web and flange layups [11]

Thermoplastic materials are generally tougher than thermosets due to a lack of cross-links. This means that they are more damage-tolerant. Moreover, thermoplastic composites have low moisture absorption capabilities, which results in minimal degradation of mechanical properties when they are used in hot or humid conditions. Sudhin et al. studied thermoset and thermoplastic materials used in aerospace applications [12]. They found that thermoplastic composites have superior fracture toughness, tensile strength, indentation resistance, and flame-retardant behaviour.

Thermosetting polymers are not environmentally friendly because the cross-links created during the curing process are irreversible. Recycling these composites involves high-temperature acids or thermal degradation techniques, but only partial fibre recovery is possible. As a result, thermoset composites are usually disposed of in landfills at the end of their life cycle. This is not an ideal option from an environmental, legislative, or resource management perspective, but it is currently the only feasible option. In contrast, thermoplastics offer new opportunities for recycling and economic benefits. For instance, long fibre-reinforced composites can be transformed into short fibre-reinforced pellets for use in injection moulding or thermo-forming processes. These recycling possibilities also create new economic opportunities [3].

High-performance thermoplastic materials are preferred for aerospace applications due to their unique advantages. The benefits provided by each polymer type are specific to its composition. For example, Polyaryletherketones (PAEKs) are known for their excellent strength, stiffness, and hydrolysis resistance over a wide range of temperatures, making them ideal for extreme applications. Polyetheretherketone (PEEK) is another popular thermoplastic material used for structural applications due to its enhanced rigidity, resulting from aromatic rings and a ketone group in its molecular structure. Recently, Polyetherketoneketone (PEKK) has gained popularity due to its potential use in primary structures manufactured using out-of-autoclave processes [3].

The advantages of thermoplastic composites, including their suitability for automated processes and recycling possibilities, have positioned them as a promising alternative in aerospace structures. However, the limitations in current analysis tools restrict the utilisation of their full potential. The subsequent section will delve into these challenges.

1.2. Challenges in Modelling Thermoplastic Stiffened Panels

Historically, in specific cases, highly efficient metallic structures could be designed to withstand loads significantly higher than buckling loads by utilising their residual strength beyond buckling [1]. However, with the advent of composite structures, current analysis tools have struggled to accurately capture the damage mechanisms that lead to final collapse under compression. This can be associated with the lack of proper understanding of advanced composites to characterise damage mechanisms in the post-buckling range [13]. Through tests, it has been observed that composite stiffened panels have enough residual strength to ensure final failure at significantly higher loads compared to the initial buckling load [14]. The lack of ability to use the analysis tools to predict the behaviour leading up to the final failure accurately has resulted in the adoption of conservative designs and heavier structures. Developing analysis tools to characterise the damage mechanisms in composite stiffened panels more accurately can allow engineers to design lighter structures.

Composite structures are susceptible to in-service and manufacturing damages. Some of the common damages observed in the case of composite stiffened panels have been skin delaminations, and stiffener debonds. Although matrix cracking can present significant local effects, they are not considered important in terms of structural collapse [1]. In the presence of damage, the post-buckling behaviour of the stiffened panels leading to the final collapse depends on the interaction of the post-buckling deformations with the damage [15]. For instance, the post-buckling deformation of the skin can cause an opening at the skin-stringer interface and promote further damage evolution [16] [14].

One way to understand the post-buckling behaviour of the stiffened panels would be to manufacture prototype structures and perform high-fidelity tests [15]. Such an exercise would, however, be both expensive and time-consuming. The issue is further exacerbated due to the complexity of measuring the failure and delaminations at critical interfaces under mixed mode conditions [17]. Analytical and numerical models can be used to predict the damage onset and propagation in the post-buckling field at relatively low costs [18]. The use of an analytical approach can be very quick and computationally efficient but generally lacks the ability to capture complex non-linear damages. Further, the interaction of inter-laminar and intra-laminar damages is not adequately captured. In contrast, finite element models are more effective in predicting complex post-buckling responses under arbitrary loading conditions. The intra-laminar delaminations can be effectively captured using tools such as Virtual Crack Closure Technique, Cohesive Zone Models and Extended Finite Element Models.

When modelling thermoplastic composites, further considerations have to be made. The influence of processing conditions on the material behaviour becomes important to consider [6]. For instance, in the case of out-of-autoclave manufacturing techniques, the process can influence the fibre direction and can sometimes introduce wrinkles and waviness in the laminate. The processing conditions can also affect the mechanical properties of the resultant structure. For instance, the lower cooling rates characteristic of the autoclave process tend to produce a high level of crystallinity in the semi-crystalline PEEK polymer when compared to the faster cooling rates in the case of Laser Assisted Tape Placement (LATP) [19]. Generally, the fracture toughness for PEEK becomes lower with high crystallinity [20]. But simultaneously, PEEK's elastic modulus and tensile/compressive strength tend to increase with higher crystallinity. Therefore, the influence of the manufacturing process, unintended damages, temperature and environmental conditions should be considered while developing a predictive model for certification purposes.

1.3. Conclusion

In this chapter, the discussion focused on the advantages associated with adopting thermoplastic composites for aircraft stiffened panels. Subsequently, in section 1.2, the challenges and considerations related to predicting post-buckling behaviour leading to final failure were outlined. These challenges hinder the predictive capabilities of analysis tools, preventing accurate capture of the damage mechanisms and culminating in collapse under compression.

To address these limitations, a comprehensive literature review explored current trends in modelling the post-buckling response of composite stiffened panels and skin-stringer separation behaviour. Additionally, damage modelling techniques suitable for modelling the skin-stringer separation behaviour were explored during the literature review. Based on this review, a research plan was developed to conclude Part I of the report. Later in the report, finite element models were developed at the coupon level (DCB specimen) and at the panel level (Multi-stringer stiffened panel).

2

Crack Propagation and Damage Modelling: Insights into VCCT, CZM, and X-FEM

This chapter delves into three prominent techniques used for modelling crack propagation in Abaqus: the Virtual Crack Closure Technique (VCCT), Cohesive Zone Modelling (CZM), and the Extended-Finite Element Method (XFEM). Each of these techniques offers a unique approach to the problem. The VCCT, based on linear elastic fracture mechanics, provides an efficient way to study crack growth behaviour. CZM, grounded in damage mechanics, enables the prediction of delamination initiation and evolution of multiple delaminations along arbitrary directions. Lastly, XFEM offers the potential to model the initiation and propagation of cracks along an arbitrary, solution-dependent path within bulk materials. This chapter aims to provide a comprehensive understanding of these techniques, their advantages, and their limitations.

2.1. Virtual Crack Closure Technique (VCCT)

The Virtual Crack Closure Technique (VCCT) is based on linear elastic fracture mechanics and posits that the strain energy released upon crack extension is equivalent to the energy required to close the crack by the same amount [21] [22]. In other words, if an initial crack of length x grows by an amount Δx, the energy released by this growth is the same as the energy needed to close the gap between points i and $i*$ (as shown in Figure 2.1). Figure 2.1 represents a 3D crack model with thickness Δz in the z-direction. The total work required to close the crack along one element, i.e. between elements E1 and E2, is given by Equation 2.1. Here, $F_{x,j}$, $F_{y,j}$ and $F_{z,j}$ are the forces acting on node j along the x, y and z-directions respectively. Further, u_i, v_i and w_i are the displacements at node i and similarly, u_{i^*}, v_{i^*} and w_{i^*} are the displacements at node i^* along x, y and z-directions.

$$\Delta E = \frac{1}{2}\left[F_{x,i}(u_i - u_{i^*}) + F_{y,j}(v_i - v_{i^*}) + F_{z,k}(w_i - w_{i^*})\right] \tag{2.1}$$

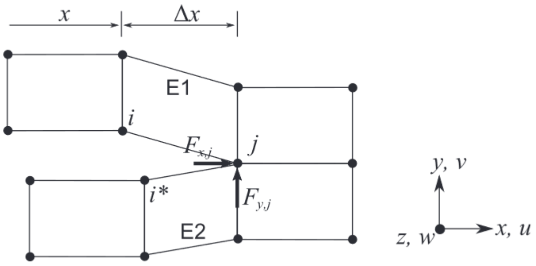

Figure 2.1: Representative VCCT crack [23]

Strain energy release rate (G) is the ratio between total work (ΔE) and crack surface area ($\Delta x \Delta z$). The components of strain energy release rate (SERR) corresponding to Mode I (G_I), Mode II (G_{II}) and Mode III (G_{III}) can be calculated using Equation 2.2, Equation 2.3 and Equation 2.4 respectively.

$$G_I = \frac{1}{2\Delta x \Delta z}[F_{y,j}(v_i - v_{i^*})] \tag{2.2}$$

$$G_{II} = \frac{1}{2\Delta x \Delta z}[F_{x,j}(u_i - u_{i^*})] \tag{2.3}$$

$$G_{III} = \frac{1}{2\Delta x \Delta z}[F_{z,j}(w_i - w_{i^*})] \tag{2.4}$$

It is often considered reasonable to ignore mode III contribution ($G_{III} = 0$) for thin-walled structures [24]. With this assumption in mind, the failure evaluation for a 2D case is explained here. Considering the crack in Figure 2.1, total energy release rate (G_T) is calculated at node j (G_T being the summation Mode I and Mode II SERR, assuming G_{III} is zero). Then, interlaminar fracture toughness G_C corresponding to the mixed mode ratio G_{II}/G_T is obtained using a fracture criterion. For instance, the 2D fracture criterion defined by Benzeggah and Kenane is considered here (see Equation 2.5) [25]. Fracture initiation is expected when the calculated total energy release rate (G_T) exceeds the interlaminar fracture toughness (G_C) i.e. $G_T/G_C \geq 1$.

$$G_C = G_{IC} + (G_{IIC} - G_{IC})\left(\frac{G_{II}}{G_T}\right)^{\eta} \tag{2.5}$$

The 2D fracture criterion presented using Equation 2.5 is determined experimentally and is specific to the material under consideration. The criterion is obtained using experimental data. To begin with, G_{IC} and G_{IIC} represent the fracture toughness of the material for pure Mode I and Mode II. η is a curve fit factor which is obtained using an experimentally obtained interlaminar fracture toughness (G_C) versus mixed-mode ratio (G_{II}/G_C) plot. The plot is generated using pure Mode I ($G_{II}/G_C = 0$) Double Cantilever Beam (DCB) tests [26], pure Mode II ($G_{II}/G_C = 1$) End-Notched Flexure (ENF) tests [27] and Mixed Mode Bending (MMB) tests [28] of varying ratios of G_I and G_{II}. Then, a curve fit for the fracture criterion (Equation 2.5 here) is done to obtain the curve fit factor factor η. The processes can be well understood in reference to Figure 2.2, which illustrates the curve fit obtained for T300/914C carbon epoxy material.

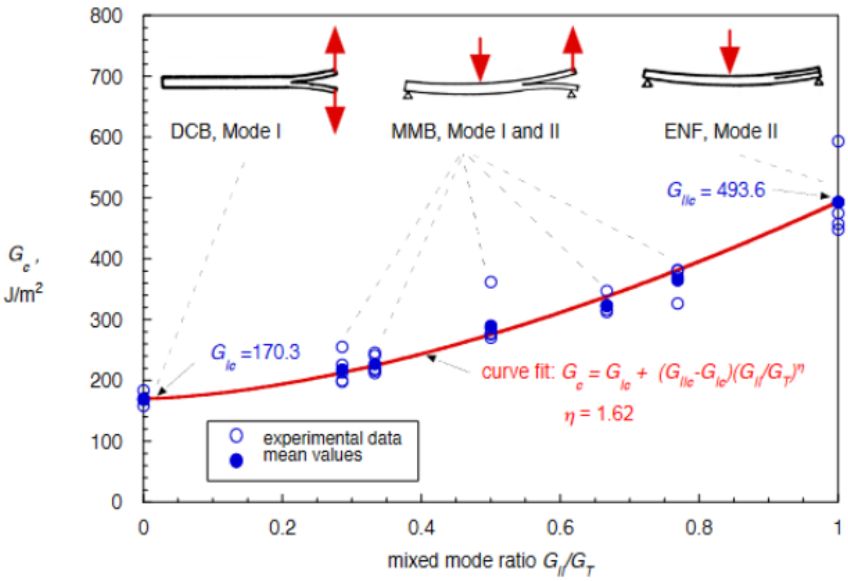

Figure 2.2: Mixed-mode fracture criterion obtained for T300/914C carbon epoxy material [29]

The same idea can be extended for three-dimensional analysis by including Mode III contribution. This is done using a fracture criterion that takes G_{III} into consideration. For instance, the failure creation presented by Reeder et al. is considered here (see Equation 2.6) [30] This criterion is an extension of the 2D fracture criterion suggested by Benzeggah and Kenane to take into account mode III scissoring shear. G_T in Equation 2.6 represents the summation of Mode I, Mode II and Mode III SERR.

$$G_C = G_{IC} + (G_{IIC} - G_{IC})\left(\frac{G_{II}+G_{III}}{G_T}\right)^{\eta} + (G_{IIIC} - G_{IIC})\left(\frac{G_{II}+G_{III}}{G_T}\right)^{\eta} \tag{2.6}$$

The VCCT approach presented here is a combination of the information obtained from [23] and [29]. The VCCT approach is well suited to study the crack growth behaviour in the presence of an initial crack [31]. The computational efficiency of Virtual Crack Closure Technique and Cohesive Zone Model (another technique to model damage evolution, see section 2.2), to model skin-stiffener dobonds were compared in the references [1] [32] [33]. The authors found that the VCCT models perform faster than the CZM models; however, VCCT lacks the ability to predict delamination initiation.

2.2. Cohesive Zone Modelling (CZM)

Based on damage mechanics, cohesive zone models are used to model the initiation and propagation of delaminations/debonds along a defined plane. This is done by defining cohesive elements (assigned at the interfaces) and the associated traction-separation law. Unlike VCCT, CZM enables the prediction of delamination initiation and evolution of multiple delaminations along arbitrary directions [34]. The concept is explained here using a linear elastic traction separation law, which can be used for numerical modelling of mixed-mode progressive damage initiation and propagation.

An uncoupled elastic relation exists between the nominal traction stress vector **t** and the corresponding separations δ as shown in Equation 2.7. The nominal traction stress vector consists of three components along the normal (t_n) and two shear (t_s and t_t) directions while δ_n, δ_s and δ_t represent the corresponding separations. In Equation 2.7, K_{nn}, K_{ss} and K_{tt} are the uncoupled contact stiffness components (pure normal or tangential separations do not result in cohesive forces in other directions). The damage is initiated when the contact stresses meet the chosen damage initiation criteria. For context, a quadratic stress criterion (see Equation 2.8) is considered here. $\overset{\circ}{t_n}$, $\overset{\circ}{t_s}$ and $\overset{\circ}{t_t}$ in Equation 2.8 represent the interface strength along the normal and two shear directions of the cohesive surface.

$$t = \begin{Bmatrix} t_n \\ t_s \\ t_t \end{Bmatrix} = \begin{bmatrix} K_{nn} & 0 & 0 \\ 0 & K_{ss} & 0 \\ 0 & 0 & K_{tt} \end{bmatrix} \begin{Bmatrix} \delta_n \\ \delta_s \\ \delta_t \end{Bmatrix} \tag{2.7}$$

$$\left(\frac{t_n}{\overset{\circ}{t_n}}\right)^2 + \left(\frac{t_s}{\overset{\circ}{t_s}}\right)^2 + \left(\frac{t_t}{\overset{\circ}{t_t}}\right)^2 = 1 \tag{2.8}$$

Once the damage is initiated, the cohesive element is degraded based on a fracture criterion. For instance, one may consider the Benzeggagh-Kenane (BK) criteria (Equation 2.9) to define the mixed-mode softening post-damage initiation. In the criterion, G_{mc} represents the mixed-mode critical energy release rate while G_{Ic}, G_{IIc} and G_{IIIc} are the critical energy release rates corresponding to pure Mode I, II and III respectively. Lastly, η is the BK curve fit parameter. The mixed mode damage evolution can be depicted using a traction-separation curve as shown in Figure 2.4. The area under the curve represents the work done to degrade the element completely and also represents the mixed-mode fracture toughness G_{mc}. Further, $\overset{\circ}{t_m}$ represents the peak mixed-mode contact stress, and δ_m^f represents the corresponding effective complete separation. If the model is unloaded after damage initiation, the unloading follows a linear path towards the origin of the traction-separation plot as shown in Figure 2.4. Any reloading after unloading also follows the same linear path until the softening envelope (line AB in Figure 2.4) is reached. A mixed mode damage evolution is shown in Figure 2.3.

$$G_{mc} = G_{Ic} + (G_{IIc} - G_{Ic})\left(\frac{G_{II}+G_{III}}{G_I+G_{II}+G_{III}}\right)^{\eta} \tag{2.9}$$

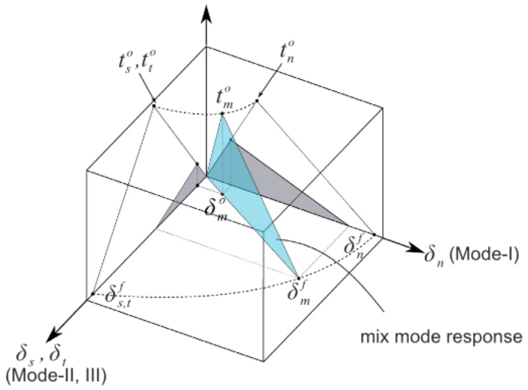

Figure 2.3: Mixed-mode damage evolution [23]

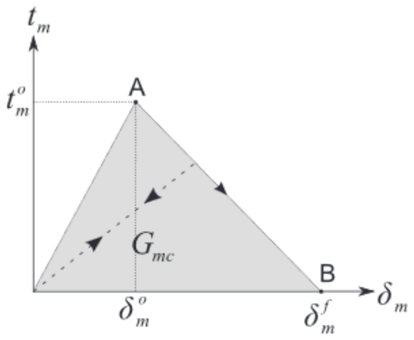

Figure 2.4: Mixed-mode linear softening law [23]

Cohesive Zone Models (CZMs) are commonly utilised to simulate delamination at interfaces. For stiffened panels, incorporating geometric imperfections shows improved correlation between CZMs and test results [35]. However, CZMs have limitations. A fine mesh is necessary to adequately represent the cohesive zone, making implementation challenging for large composite structures [6]. This also makes the CZMs slower when compared to VCCT. Additionally, commercial implementations have not been thoroughly evaluated under mixed-mode loading conditions, with mode III often being neglected. The CZM approach discussed in this section was used by Baran et al. to predict delamination at the skin-filler interface of a C/PEKK butt joint specimen in a 3-point bending test, is one of many interpretations found in literature [23] [36] [37] [38] [34]. Nonetheless, it captures the fundamental concept of the model. For non-linear post-buckling analysis, an incremental arc-length method combined with Newton-Raphson iteration can be employed with CZMs to trace the load direction and path, accurately capturing post-buckling behaviour [31].

2.3. Extended Finite Element Method (XFEM)

The VCCT and CZM techniques require pre-defined interface elements along the interface where delaminations are expected. Further, the crack propagation predicted using these models is self-similar and confined along the edges of the elements. VCCT, in particular, could require constant re-meshing to conform the mesh to changes in the discontinuity geometry as the crack propagates. The extended finite element method, which was proposed by Belytschko et al., differs from other methods that limit the growth of cracks along predefined paths. This method can predict the initiation and propagation of cracks along an arbitrary, solution-dependent path within bulk materials without tying it to the element boundaries. This means that the method does not require the mesh to conform to the discontinuity geometry as long as the mesh is sufficiently small [39]. A brief explanation of the XFEM implementation in Abaqus is provided in this section [40]. There are two approaches that can be used to model crack growth using XFEM in Abaqus: the linear elastic fracture mechanics (LEFM) approach and the cohesive segments method based on a traction-separation approach.

The extended finite element method can be used to model moving cracks by using phantom nodes. These nodes are superposed on the original real nodes and represent the discontinuity of the cracked elements. When the element is intact, each phantom node is constrained to its corresponding real node. However, when a crack cuts through the element, it splits into two parts, each formed by a combination of real and phantom nodes. The separation between the nodes is governed by a cohesive law or the strain energy release rate until the traction on the cracked element is zero. At this point, the phantom and real nodes move independently.

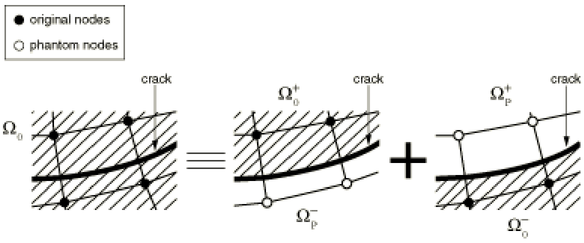

Figure 2.5: Illustration of phantom node concept [40].

To have a set of full interpolation bases, the part of the cracked element that belongs to the reference domain, Ω_0, is extended to the phantom domain, Ω_p. This allows for displacement in the real domain to be interpolated using degrees of freedom for the nodes in the phantom domain. The jump in the displacement field is integrated over the area from the side of the real nodes up to the crack, which is Ω_p^+ and Ω_p^-. The equivalent polynomial methodology, originally developed by Ventura et al. for a cracked element enriched with a Heaviside enrichment function, is used to evaluate the stiffness matrix for the cracked element composed of real and phantom nodes [41]. This method exhibits almost no mesh dependence when the mesh is sufficiently refined.

The phantom nodes approach in Abaqus is used in conjunction with the cohesive segments method or Linear Elastic Fracture Mechanics (LEFM) principles. In both cases, the near-tip asymptotic singularity is not taken into consideration. Instead, only the displacement jump across a cracked element is considered. As a result, the crack needs to propagate across an entire element at a time to avoid the necessity of modelling the stress singularity. When used with the cohesive segments method, the separation between the cracked surfaces is governed by a cohesive law. This means that the initiation of the crack is determined using a damage initiation criterion. The evolution of damage within the element is then governed using a fracture criterion. This process is similar to the one described in section 2.2.

When used in conjunction with LEFM principles, the real node and the corresponding phantom node will separate when the equivalent strain energy release rate exceeds the critical strain energy release rate at the crack tip in an enriched element. The traction initially is carried as equal and opposite forces on the two surfaces of the cracked element. The traction is then ramped down linearly over the separation between the two surfaces. The dissipated strain energy equals either the critical strain energy required to initiate the separation or the critical strain energy required to propagate the crack. This depends on whether the VCCT or the enhanced VCCT criterion is specified.

XFEM has the potential to offer various benefits, but the current implementation in Abaqus has some limitations. It is best suited for modelling a single crack within an enriched region, which is a predefined area in the model where the extended finite element method (XFEM) is used to model a crack. The current implementation does not support the branching of a single crack or interaction among multiple cracks. Moreover, a new crack cannot initiate within the enriched region until the existing crack propagates through the boundary of the enriched feature. Additionally, crack initiation is not possible near a pre-existing crack, and a newly initiated crack cannot approach or enter an already cracked element. Although defining multiple enriched regions can mitigate some of these limitations to a limited extent, the interaction between multiple cracks is still limited.

2.4. Conclusion

This chapter explored three different techniques for modelling crack propagation: the Virtual Crack Closure Technique (VCCT), Cohesive Zone Modelling (CZM), and the Extended-Finite Element Method (XFEM). Each of these techniques offers unique advantages and has its own set of limitations.

The VCCT, based on linear elastic fracture mechanics, provides an efficient way to study crack growth behaviour in the presence of an initial crack. However, it lacks the ability to predict delamination initiation and could require re-meshing to conform the mesh to changes in the discontinuity geometry as the crack propagates. Based on damage mechanics, Cohesive Zone Modelling (CZM) enables the prediction of delamination initiation and evolution of multiple delaminations along arbitrary directions. However, it requires a fine mesh to adequately represent the cohesive zone, making implementation challenging for large composite structures. Moreover, commercial implementations have not been thoroughly evaluated under mixed-mode loading conditions. The Extended-Finite Element Method (XFEM) offers the potential to model the initiation and propagation of cracks along an arbitrary, solution-dependent path within bulk materials without tying it to the element boundaries. However, the current implementation in Abaqus has some limitations, particularly when it comes to modelling the branching of cracks and the interaction among multiple cracks.

In conclusion, while each technique has its strengths and weaknesses, they all provide valuable tools for studying crack propagation. The choice of technique will depend on the specific requirements of the study and the limitations that can be accommodated.

3

Computational Studies on Composite Stiffened Panels

The previous chapter discussed the numerical techniques used for modelling damage. This chapter presents insights from various computational studies conducted on composite stiffened panels. The literature review reveals that VCCT and CZM methods were commonly used to predict the post-buckling behaviour of the panels.

3.1. Computational Studies Based on Virtual Crack Closure Technique

This section presents a comprehensive review of computational studies utilising the Virtual Crack Closure Technique (VCCT) to investigate the behaviour of stiffened panels with skin-stringer debonds. The studies are categorised based on the shape of the stiffened panels: Omega-shaped, T-shaped, and J-shaped.

3.1.1. Omega-Shaped Stiffened Panels

Dávila et al. studied single stringer hat stiffened specimens with an embedded debond created using a Teflon insert at the skin-stringer interface on one side [15]. Two finite element models were made with 40 mm (16.67% length) and 20 mm (8.33% length) skin-stringer debonds. Geometric imperfections were not considered in the models. The results of the finite element model with a 40 mm debond were compared with those obtained from a quasi-static compression test. The finite element model of the specimen with 40 mm debond showed that the fracture criterion is met at 80% of the collapse load at the inner corner of the insert. Beyond this, the delamination begins to propagate both towards the free edge of the flange and the longitudinal direction (see Figure 3.1). No delamination propagation was observed for the model with a 20 mm debond until the collapse load. When the collapse load was reached, a sudden change in the post-buckling mode introduced peeling stresses at the interface and caused a sudden collapse of the panel. During the quasi-static compression test, buckling was observed at 28.1% of the collapse load, with three half-waves along the free edges of the specimen. As the load increased, the out-of-plane deformation increased gradually while the number of half-waves remained the same. At the final failure load sudden extension of the initial delamination to 30 mm occurred (see Figure 3.2). This causes a load drop. After a UT scan, the specimen was reloaded. In this case, the stringer detached from the skin suddenly when the applied load was close to the previous failure load (28.38 kN). This led to the creation of a tunnel under the stringer and a second load drop to 21.02 kN (refer to Figure 3.3).

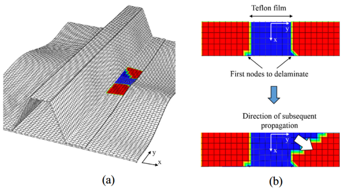

Figure 3.1: Opening of the 40 mm embedded debond in the post-buckling range: (a) View of the model; (b) Propagation details [15]

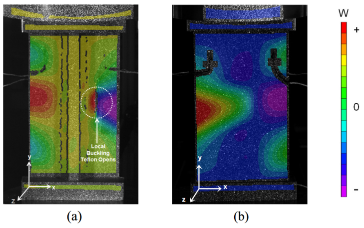

Figure 3.2: Post-buckling displacements after opening of debond in quasi-static compression test at 24.65 kN: (a) Stringer Side; (b) Skin side [15]

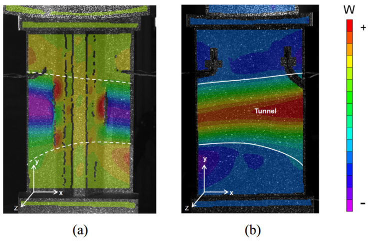

Figure 3.3: Post-buckling displacements after tunnelling (second load drop) at 21.02 kN kN: (a) Stringer Side; (b) Skin side [15]

The study conducted by Bisagni et al. aimed to examine the impact of skin/stringer debond on a single stringer hat stiffened compression specimen [42]. The specimen in question had a skin-stringer debond of 20 mm (8.33% of the panel length), created using a Teflon insert. The authors compared the models with the results from a quasi-static compression test. The predicted and experimental buckling loads were in good agreement. However, the final collapse load was under-predicted by 4% (see Figure 3.4). Regarding damage propagation, the model showed that debonding began at a corner node on the free edge, followed by stress redistribution (see Figure 3.5). The debond progressed inwards at a 45°angle and was mode I dominant. The authors noted that this occurred in the post-buckling field. As part of their study, the researchers also compared the effect of the two debonding options available in Abaqus: (a) RAMP option, where tension is gradually released when the energy release rate reaches the critical value at the crack tip. This improves convergence and requires fewer iterations. The crack front can assume a curved shape close to the experimentally observed shape. (b) STEP option, the default option, where the constraint holding the crack tip closed is suddenly released once the critical energy release rate is reached. This results in sudden load drops and reloading in the load-displacement curve and causes numerical convergence issues. The resultant delamination front is aligned with the mesh and is inconsistent. The comparison was done by modelling delaminations in DCB specimens. An irregular mesh was used to show the crack tip shape in the DCB specimen and highlight the shortcomings of the STEP option (refer to Figure 3.6 and Figure 3.7).

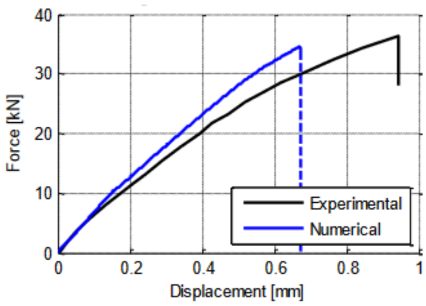

Figure 3.4: Comparison of load-displacement curves obtained experimentally and numerically [42]

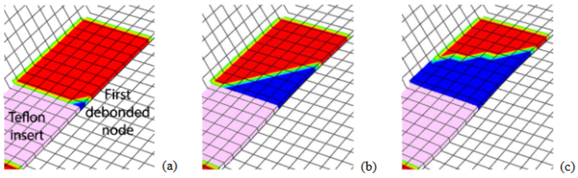

Figure 3.5: Evolution of debond at the skin/stringer interface (FE Model) [42]

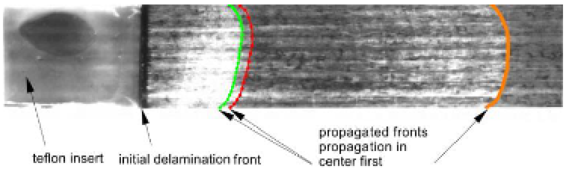

Figure 3.6: Crack tip shape for a DCB test specimen [42]

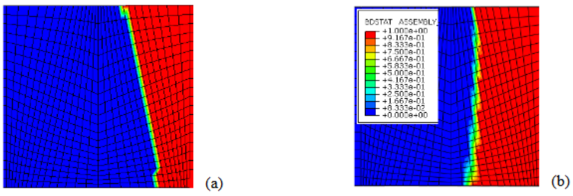

Figure 3.7: Shape of the delamination front in a DCB with a non-regular mesh: (a) STEP option; (b) RAMP option [42]

Raimondo et al. studied the post-buckling behaviour of a single stringer omega stiffened panel using quasi-static compression tests and an FE model [43]. The specimen studied had an initial 40 mm (13.34% panel length) skin-stringer debond under one of the flanges. For the model, initial imperfections were introduced using 1% of the out-of-plane displacements of the first-buckling mode. The load-displacement curves obtained from the quasi-static tests and FE model were compared (see Figure 3.8). The model underestimated the first load-drop corresponding to the delamination onset, which the authors attributed to the difference in fracture toughness values obtained through ASTM standard coupon tests where delamination was positioned between 0° plies, while the delamination in the specimen occurred between +45°/-45° plies at the skin-stringer interface. The skin initially buckled in three half-waves in the shape of the initial imperfections. Corresponding to the first load drop, the delaminated region of the stringer flange buckled into a single half-wave, and the skin on the delamination side changed to a single half-wave while the mode shape on the other side inverted. The local buckling shape of the stringer flange then shifted to two and eventually three half-waves corresponding to the second and third load drops. Before the final failure, a final mode shift happened on the stringer flange to three half-waves. The post-buckling shapes obtained from the numerical model and experiments matched well, but the direction of numerical displacements was opposite to that from experimental displacements before delamination growth onset. When studying mode I, II, and III contributions along the flange width at different load drops, it was found that mode I had a high contribution at the first load drop, and subsequent load drops saw an increasing dominance of mode II and III contributions until mode III became dominant nearing the end of the post-buckling field. The higher contribution of mode III could also contribute to inaccuracies in a model using B-K failure relation since the criterion used by the authors considered modes II and III together.

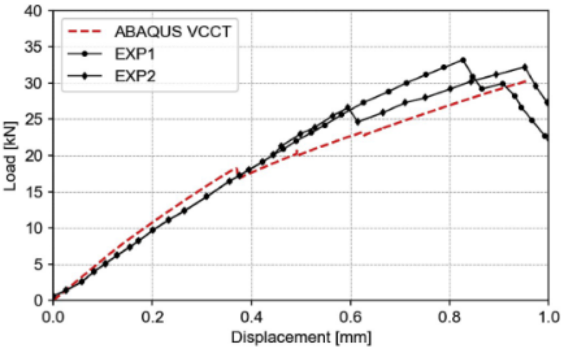

Figure 3.8: Load displacement curves of the specimen obtained using the quasi-static tests and the model [43].

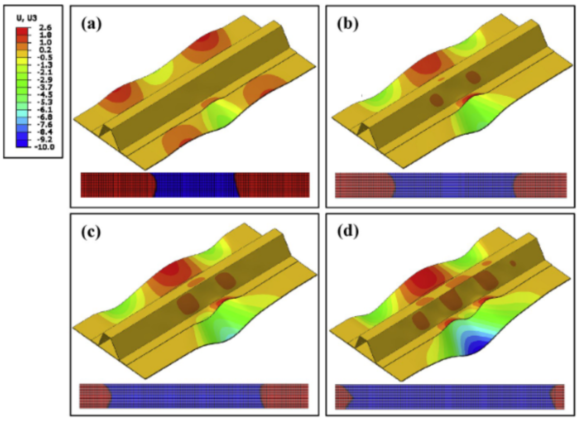

Figure 3.9: Out-of-plane displacements and delamination of the specimen at applied displacements of: (a) 0.37 mm; (b) 0.49 mm; (c) 0.62 mm and (d)0.97 mm [43].

3.1.2. T-Shaped Stiffened Panels

Orifici et al. used a global-local approach to study the behaviour of single T-stiffened panels in both damaged and undamaged states [1]. Two damaged panels with skin-stringer debond of 80 mm (for a 400 mm long panel) and 105 mm (for a 500 mm long panel) located mid-length were analysed. FE models were created to obtain the deformation field using a global shell model. The boundary conditions from the global model were introduced to a local 3D brick model of a skin-stiffener interface. In order to determine the initiation of delamination or skin-stiffener separation, the Degenerated Tsai equation was utilized. For the ply damage degradation model, the Hashin failure criteria equations were employed [44] [45]. The inter-laminar growth was modelled using VCCT in combination with the BK criterion [25]. The models predicted crack growth to occur after buckling of the debonded area, and further compression caused matrix cracking and an increase in the debonded area. Later in the post-buckling process, fibre failure occurred in the stiffener, resulting in a final collapse. The observed damage evolution leading to the final collapse matched well with tests. For one of the panels, a good correlation was achieved using nominal toughness values, but in the other, toughness values had to be increased by 5 times to achieve a good correlation with the delamination area. The final collapse loads also matched well with the tests.

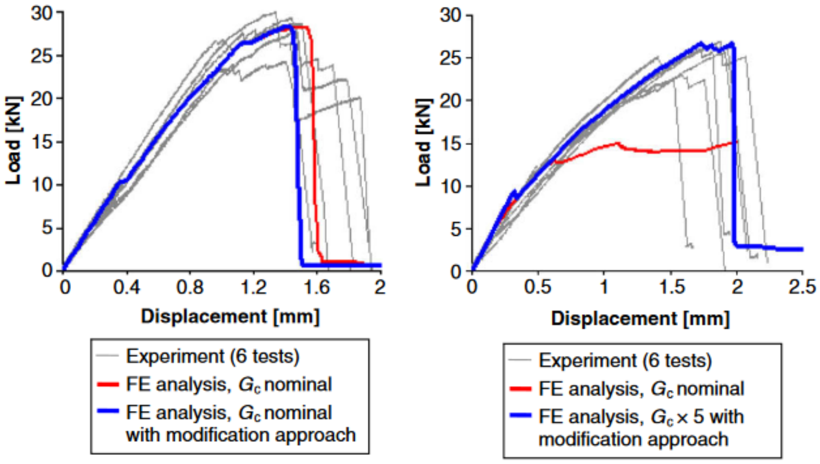

Figure 3.10: Load displacement curves for panels with 80 mm debond (left) and 105 mm debond (right) [1].

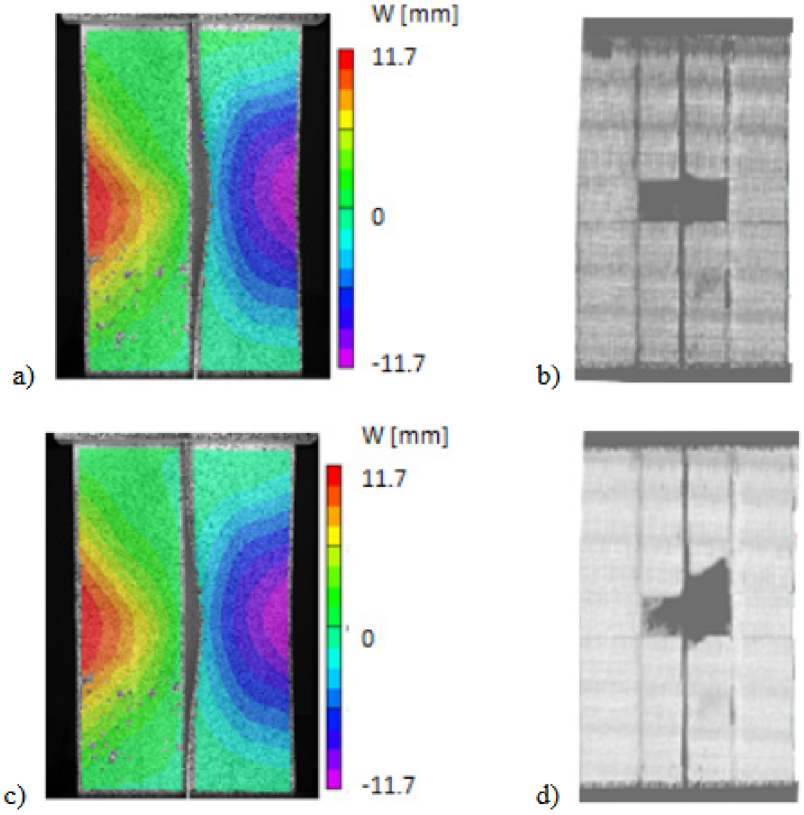

Figure 3.11: Propagation of delamination in the second specimen: (a) Out-of-plane displacements at 35.12 kN; (b) delamination on set at 35.12 kN; (c) Out-of-plane displacements at 37.58 kN and (d) delamination propagation at 37.58 kN [46].

Zou et al. modelled and tested three single stringer compression specimens with T-stiffener with 30mm (10% panel length) Teflon inserts placed mid-length at the skin-stringer interface [46]. The first specimen's initial buckling mode was asymmetric with respect to the stiffener along the longitudinal direction with a single half-wave located at the mid-length of the free edges. Upon further compression, skin deflection increased until the stiffener web bent towards the side with the most negative out-of-plane displacement. Skin-stringer separation was then initiated on that side, and final collapse occurred due to separation and transverse fracture on the stiffener web and flange. The second specimen's out-of-plane displacements and skin-stringer debonds are presented in Figure 3.11. Finite element models made with VCCT accurately captured structural response, skin-stringer separation, and delamination initiation location. Skin-stringer separation initiation observed using the finite element model was overestimated by 3.6%, and stiffness was also overestimated. The authors hypothesise that the overestimation could have been because material non-linearity arising from damage propagation was ignored in the model.

Riccio et al. applied a three-module modification to the standard VCCT approach [47]. When used to model a single stringer specimen with a T-stiffener, the modified VCCT approach was found to better approximate the delamination growth compared to the standard VCCT approach, which overestimated the delamination growth (refer to Figure 3.12).

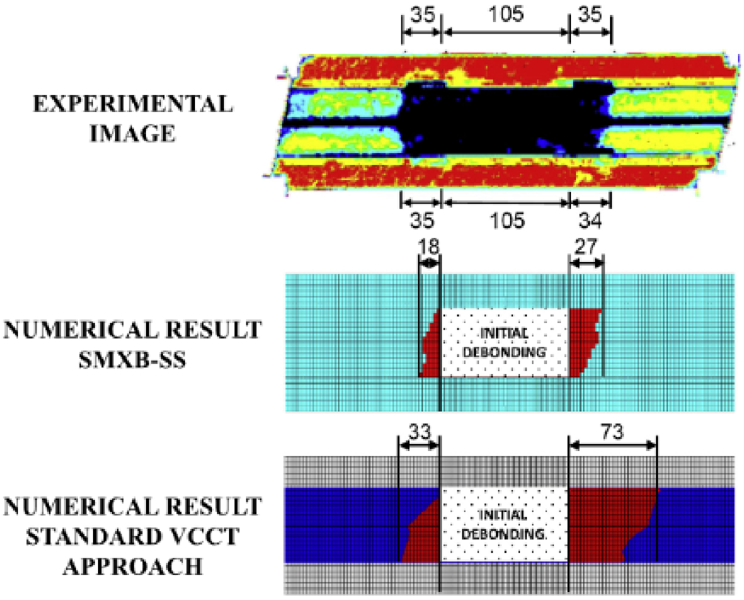

Figure 3.12: Comparison of the debonded area: (Top) Experimental; (Middle) Modified VCCT method and (Bottom) Standard VCCT approach [47].

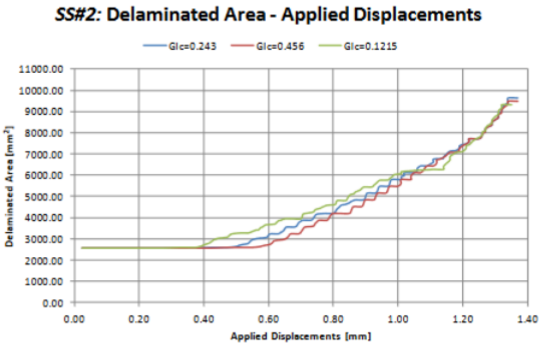

Figure 3.13: Delaminated area versus applied displacement for SS2 specimen modelled by Riccio et al. [48].

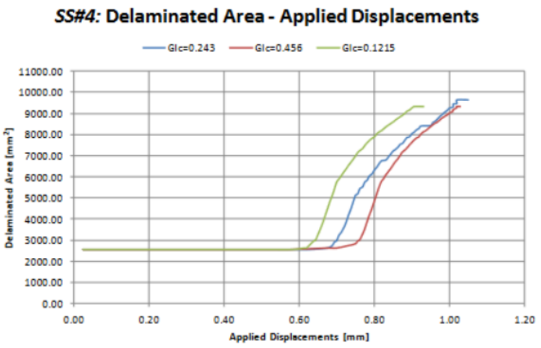

Figure 3.14: Delaminated area versus applied displacement for SS4 specimen modelled by Riccio et al. [48].

During the evolution of mode I delamination in composite structures, fibre bridging may occur and increase the material's resistance to crack opening [49]. This increases the material's mode I critical energy release rate and delays crack propagation. Riccio et al. studied the influence of fibre bridging on skin-stringer debonding in a composite panel [48]. They considered the influence of fibre bridging by increasing G_{IC}

based on a G_{IC} vs crack opening curve obtained by performing polynomial regression on several DCB test results. When this approach was applied to single-stringer T-stiffened panels, it was found that the change in G_{IC} value due to fibre bridging had a significant effect when the skin-stringer debond was the mode I dominated. However, if the delamination was not mode I dominated, the effect on the delamination area was insignificant. This can be observed when comparing the delamination areas in Figure 3.13 and Figure 3.14, where the delamination evolution was only driven by the mode I component for the SS4 specimen.

3.1.3. J-Shaped Stiffened Panels

Dooren et al. manufactured and tested two Fast Crystallising PolyEtherKetoneKetone (PEKK-FC) carbon composite stiffened panels [50]. The 445.3 mm long panels had three stringers with an angled cap on one side and were joined to the skin with a short-fibre reinforced butt-joint (refer to Figure 3.15). A 40 mm Teflon insert was placed under the middle stringer and later extended to 70 mm by applying out-of-plane displacement to the skin to represent barely visible impact damage (BVID). The panels were subjected to compression until the final collapse. A finite element model using VCCT and the B-K failure criterion was also developed. Geometric imperfections obtained from the panel using 3D Digital Image Correlation (DIC) were introduced to the model. When the model's results were compared with the tests, it was found that the linear stiffness before buckling was accurately predicted while the buckling load was over-predicted by 5.3%. The loss in stiffness due to crack growth, although slightly over-predicted, was close to the test results. The final failure load for both panels was over-predicted. Regarding the buckling mode, anti-symmetric buckling with three half-waves in each bay area was observed. Due to the outward half-wave and tunnelling, a crack opened between the web of the middle stringer and the skin. As the panel was further compressed, the right stringer web separated from the skin, followed by the separation of the cap and web of the middle stringer. Before final failure, the left stringer separated from the skin, and simultaneously, the cap and web of the right stringer also separated. A mode shift also occurred during post-buckling, where a fourth half-wave appeared on top of the right bay. The model accurately predicted the structural behaviour and sequence. The out-of-plane displacements of the first panel obtained from tests and the model are shown in Figure 3.16.

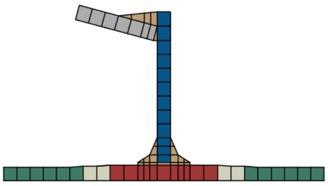

Figure 3.15: Angled cap stringer cross-section [50].

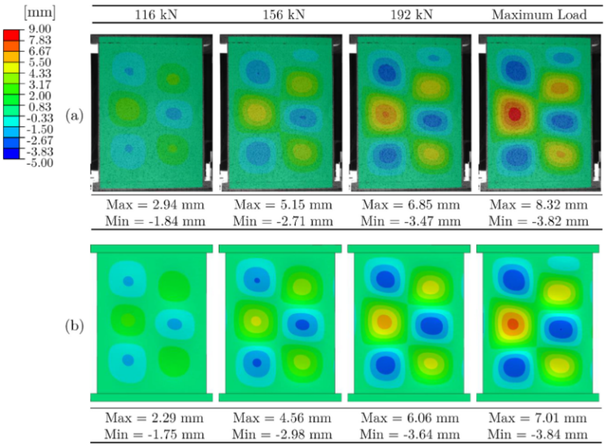

Figure 3.16: Out-of-plane displacements: (a) Panel A: test (b) Panel A: FE Model [50].

3.2. Computational Studies Based on Cohesive Zone Modelling Technique

3.2.1. Omega-Shaped Stiffened Panels

Vescovini et al. studied the post-buckling response of a multi-stringer panel (consisting of 5 hat stiffeners) using FE models [18] using a global-local approach. The global model of the panel, made with a relatively coarse mesh of shell elements, computed the displacement field but was not meant to capture damage initiation and delaminations. The local model analysed a small portion of the panel in detail, considering damage initiation and delamination. The stringer in the area of interest was divided into five small local models with four additional overlapping sections. Cohesive elements were used between the skin and the stringer with a finer mesh. The model was loaded using boundary conditions with displacements obtained from the global model. If there is a change in the stiffness of the local model due to damage, the global model is modified iteratively based on the results from the local analysis by conducting the global and local analysis in series. The analyses indicated that the panel's collapse was influenced by its post-buckling deformation. A post-buckling mode transition in the skin between the two stringer webs caused a mode I delamination of the stringer. The collapse of the panel was observed to be sudden and was governed by unstable delamination growth.

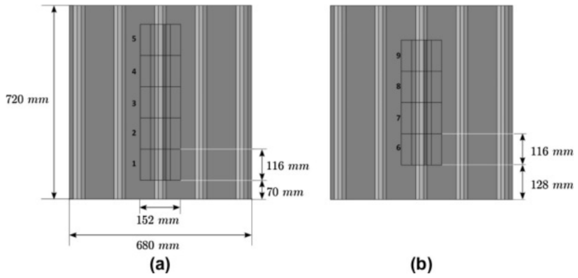

Figure 3.17: Local model division: (a) local models 1-5 (b) overlapping models 6-9 [18]

Kootte et al. modelled a four-stringer omega stiffened panel to find a critical location of skin-stringer separation during post-buckling [16]. To reduce computational requirements, the panel was divided into inner and outer sections (see Figure 3.18). The authors reasoned that skin-stringer separation primarily occurs in the inner section and hence implemented the damage model there. The outer section did not require a damage model and was tied to the inner section using a rigid body tie constraint to prevent separation. A cohesive zone was introduced between the top nodes of the skin and the bottom nodes of the stringer in the inner section. The panel was subjected to a quasi-static displacement of 1 mm/s. Figure 3.19 represents the out-of-plane buckling deformation and the interface separation in the panel. The red areas in the inner section represent skin-stringer separation, and the blue areas represent intact regions. The authors noted that the interface was subjected to combined mode II + III opening due to high shear stresses caused by skin twisting at the inflexion point of the buckling wave. In the model, the separation did not grow beyond the inner radius of the stringer because the innermost element of the stringer was tied to the skin, restricting growth. However, if the separation was allowed to extend from one flange to another, a tunnel could have been created underneath the stiffener, leading to panel collapse.

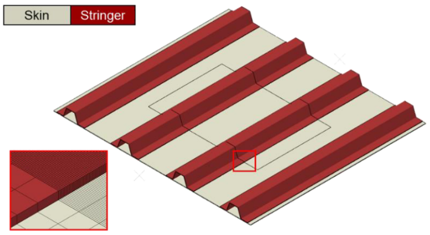

Figure 3.18: Separation of the inner and out sections in the four-stringer panel studied by Kootte et al. [16].

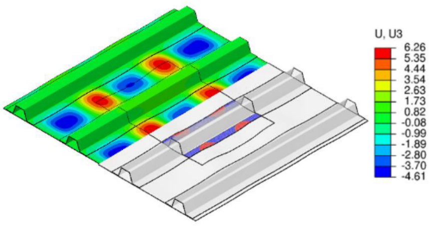

Figure 3.19: Out-of-plane buckling deformation and interface separation obtained using the FE model [16].

Bisagni et al. studied the post-buckling response of composite co-cured hat stringer specimens experimentally [51]. They compared pristine panels with panels that had a Teflon insert between the stringer flange and skin. The panel's collapse load decreased by 17% and 28% with 20mm and 40mm Teflon inserts, respectively. The authors also studied the effect of initial imperfections on post-buckling mode shape using finite element models in combination with cohesive elements. Two imperfections were considered: 1) deformation due to thermal cool down from thermal loads and 2) imperfections as a linear combination of the first three eigenmodes scaled to 1% of skin thickness. Variations in initial imperfections and thermal cycles resulted in post-buckling mode shape variations, affecting the skin-stringer interface's critical region. The authors concluded that minor manufacturing and residual thermal strain imperfections affect post-buckling response. These also induce changes in internal load distribution, which affects skin-stringer delamination initiation and propagation. Pre-test measurements should, therefore, be carried out to measure stringer misalignment and panel curvature. These measured imperfections should then be added as perturbations in finite element simulations.

Action et al. studied a four-stringer hat-stiffened panel with two Teflon inserts and compared a finite element model with test panel results [52]. A coarse global mesh captured panel deformations except near the Teflon inserts. A local model (refer to Figure 3.20 and Figure 3.21) was created with CompDam VUMAT material properties and cohesive elements (between sub-components) to capture delamination growth, ply cracks and migrations. Two fracture toughness values were considered: Critical fracture toughness (G_C) and fracture toughness when resistance to crack growth is fully developed (G_R) such that $G_R > G_C$. The stiffness captured across the model was mostly within 10% of the average test value. The models predicted the onset of buckling within 3% and 9% of the average test value for the centre and outer skin bays, respectively. Using G_C as fracture toughness value resulted in a larger damage morphology than observed from tests, and the damage also assumed a more rounded shape (see Figure 3.22). The damage onset was predicted at a load within 5% of the experimentally observed load. The model accurately predicted the single matrix split that led to delamination migration from the skin-stringer interface to the skin's ply1-ply2 interface. The distribution of damage was not the same as test results, and peak load was over-predicted by 5%. Using G_R as fracture toughness, damage onset occurred at a higher load (15% higher than the average test result). The model still predicted delamination migration due to matrix splits, but peak load was over-predicted by 12%. The predicted damage assumed a more rounded shape (refer to Figure 3.23).

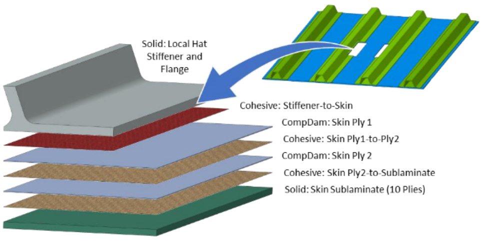

Figure 3.20: Description of the local model defined by Action et al.[52].

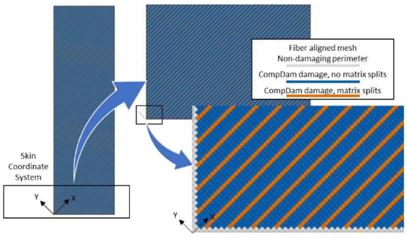

Figure 3.21: Mesh definition to evaluate intra-laminar local failure [52].

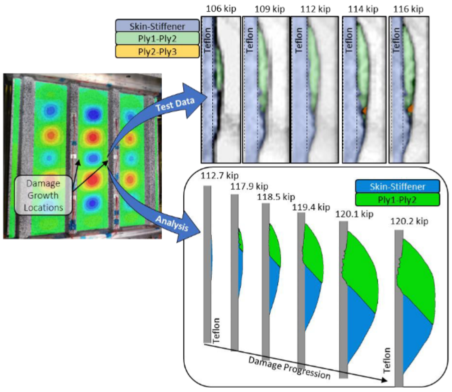

Figure 3.22: Predicted damage evolution with fracture toughness G_C [52].

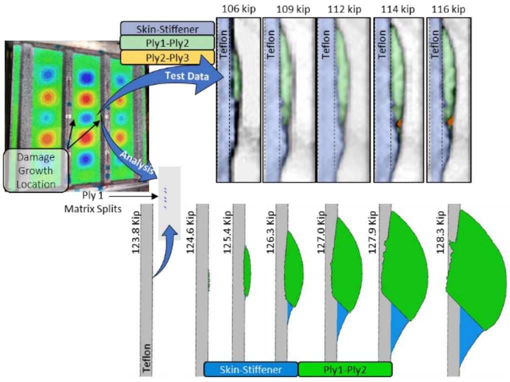

Figure 3.23: Predicted damage evolution with fracture toughness G_R [52].

3.2.2. T-Shaped Stiffened Panels

Masood et al. used cohesive elements to model the post-buckling behaviour of thermoset multi-stiffened panels with four co-cured T-stiffeners [36]. They also used intra-laminar Hashin failure criteria to predict ply failure. When the numerical model's results were compared to the test results, it was found that the model accurately captured the buckling and post-buckling modes. Additionally, the load vs end shortening curve correlated well up until the collapse load. The authors stated that the model predicted debond to occur at the skin-stringer interface near the clamp ends at all four stringers. However, no such debond was observed in the test panel when an ultrasonic A-scan was performed.

Using cohesive elements, Ye et al. studied the behaviour of composite T-stiffened panels with different bond methods [37]. They found that bonding had little effect on the panel's uniaxial compression stiffness but significantly affected the final failure load and the skin-stringer interface's failure mode.

3.2.3. J-Shaped Stiffened Panels

Šedek et al. studied the effect of skin-stringer debond on multi-stringer stiffened panels made using PEKK [53]. The panel consisted of 5 stringers, and the butt-joint technique was used to connect the joints in the panel. Pristine and damaged panels were modelled using cohesive elements, and the results were compared with tests. The damaged panels contained a 70 mm initial delamination between the centre stringer and the skin. The model under-predicted the collapse of the pristine and damaged panels by 3% and 9%, respectively. In the case of the panel with an initial debond, debond extension happened along one of the crack fronts in the longitudinal direction, followed by extension along the other crack front. Upon failure of the centre stringer, the other stringer webs began to debond from the skin. The final failure was characterised by the separation of the webs from the skin and caps. The pristine panel also exhibited similar behaviour. A summary of the results obtained from the finite element model for the pristine and damaged panels is given in Figure 3.24.

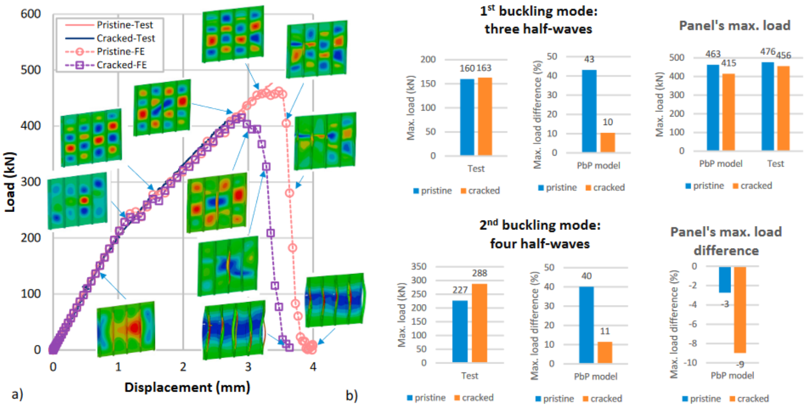

Figure 3.24: Summary of the finite element model results for the pristine and damaged panels [53].

3.2.4. I-Shaped Stiffened Panels

Wang et al. studied the effect of mode III fracture toughness on the post-buckling failure behaviour of multi-stringer stiffened panels with I-shaped stiffeners [54]. Two models were made, one considering mode III fracture toughness and one without ($G_{IIIC} = G_{IIC}$ if mode III is ignored), using the damage criterion defined by Reeder [30]. Cohesive elements were used to model damage at the skin-stringer interface. Compared to experimental test results, it was found that considering mode III fracture toughness had little influence on predicting the buckling load (with a 4.85% over-prediction in both cases). Although both models over-predicted the final failure load, the error was 2.6% when mode III was considered and 6.6% when it was not. The model using mode III also accurately predicted post-buckling behaviour. The failure process occurred in two stages: 1) Interface peeling and shear stresses at the node line along the panel's middle initiated damage on the two free edges of the stiffener's lower flange due to the buckling mode shape. 2) As the load increased, damage on both sides of the flange propagated inwards until they intersected each other, creating a tunnel under the stringer. The damage evolution in the I-shaped stiffener is shown in Figure 3.25.

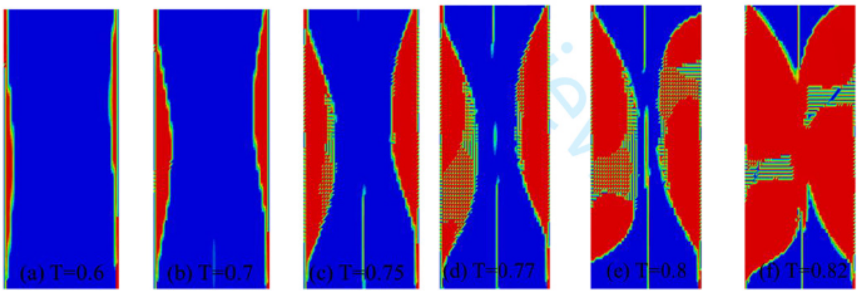

Figure 3.25: Extension of damage in the mode III fracture zone at the interface [54].

3.3. Conclusion

In conclusion, both the Virtual Crack Closure Technique (VCCT) and Cohesive Zone Modelling Technique (CZM) offer valuable tools for studying the skin-stringer separation behaviour in composite stiffened panels. However, there is room for improvement in the accuracy of these models, particularly in predicting post-buckling behaviour and final failure load. The study by Bisagni et al. highlighted the importance of considering the geometric and thermal strain imperfections introduced to the stiffened panels during manufacturing [51]. These imperfections can significantly impact the post-buckling behaviour of the panels, underscoring the need for accurate modelling of these imperfections.

Furthermore, it was observed that both VCCT and CZM techniques are popularly used to model skin-stringer debond in the post-buckling field. They can predict the post-buckling behaviour of the panel close to what has been observed through quasi-static tests. However, these models have a tendency to either overestimate or underestimate the buckling and final failure loads and the stiffness in the post-buckling range [42] [50]. This discrepancy suggests that the boundary conditions, imperfections, damage modelling techniques, and any assumptions made during modelling must be carefully considered to improve the accuracy of these models.

The presence of delaminations in the skin-stringer interface significantly impacts the post-buckling behaviour of the stiffened panels [53] [51]. The study by Davila et al. further highlighted that the length of the initial debonds also determines the onset of delamination in the post-buckling behaviour [15]. In their case, a longer initial debond caused an earlier onset of delamination propagation and determined the structural integrity of the panels and the failure mechanism. The study conducted by Action et al. emphasized the significance of fracture toughness value in determining the predicted damage morphology, damage onset load, and the final failure load [52]. A higher fracture toughness value leads to a higher damage onset load, higher peak load and an increased predicted damage area. Thus, it is a crucial factor in predicting the behaviour of composite stiffened panels. The study by Riccio et al. also highlights the need to consider the increase in mode I fracture toughness due to fiber-bridging, especially in cases where the damage evolution is mode I dominated [48].

The study by Ye et al. highlighted the influence of bonding on the post-buckling behaviour of the panel [37]. It showed that the bonding has little effect on the panels' uniaxial compression stiffness but significantly affects the final failure load and the failure mode at the skin-stringer interface. This finding underscores the importance of accounting for the effect of the bonding method in designing and analysing composite stiffened panels.

Lastly, it is important to note that while the studies in the literature use VCCT and CZM damage modelling techniques to model the skin-stringer separation behaviour in stiffened panels, these techniques limit the predicted crack extension along a predetermined path. Using the extended finite element method could allow the prediction of crack extension along an arbitrary solution-dependent path along the skin-stringer interface. However, to the best of the author's knowledge, no studies about using the extended finite element technique to predict the damage evolution in composite stiffened panels were found in the literature. This presents a research gap and the benefits and shortcomings of using XFEM could be potentially investigated through this thesis project. Overall, this chapter has comprehensively reviewed computational studies on composite stiffened panels. The insights gained from these studies will undoubtedly contribute to the modelling efforts that are planned to be carried out in this project.

4

Project Planning

4.1. Key Takeaways from Literature Study

The previous chapters have provided an extensive review of the literature study conducted. The aim of this section is to summarise the key findings from the literature study. To start with, chapter 1 highlighted the potential of thermoplastic composites to provide manufacturing solutions that could lead to faster and cost-effective manufacturing of aircraft structures through automated manufacturing techniques. Stiffened panels are commonly used as primary aircraft structures and are mainly manufactured using fibre-reinforced composites. Currently, thermosets are the primary material of choice for these structures. Although thermoplastics have higher impact toughness and low moisture absorption capabilities, their high material and tool costs have limited their use. However, with a focus on sustainability and automation, thermoplastics have become more attractive in recent years. Their use allows for rivet-free joints and simplified manufacturing, potentially compensating for their high cost. Despite the many advantages, the accuracy of current post-buckling analysis tools limits the design of weight-efficient post-buckling structures made of composites. Although composite stiffened panels can handle loads beyond the initial buckling load, there is a lack of understanding of the damage mechanisms associated with composites, which limits the ability to predict their post-buckling response accurately. This makes it challenging to certify these structures to operate in the post-buckling field.

The post-buckling behaviour of composite stiffened panels can be predicted through non-linear finite element analysis by gradually increasing the load in small increments. The change in geometry due to large displacements and rotations is considered by updating the stiffness matrix at the end of each load step. During the non-linear analysis, the presence of damage and its evolution can be accounted for using numerical models like VCCT, CZM, and XFEM. Chapter 2 provided a summary of these damage modelling techniques. VCCT is based on linear elastic fracture mechanics and considers the SERR along the crack front to predict crack propagation. Although fairly accurate results can be obtained using a relatively coarse mesh, VCCT can only be applied to study damage evolution in the presence of a pre-existing crack. In contrast, CZM uses a traction-separation law in conjunction with a fracture criterion to predict the initiation and propagation of arbitrary cracks. The drawback, however, is that cohesive models are slower when compared to VCCT-based models since they require the use of fine meshes to provide acceptable results. Lastly, X-FEM is an extension of the traditional finite element method where the discontinuity's presence is considered by locally enriching regions with additional degrees of freedom. Unlike VCCT and CZM-based techniques, the XFEM offers the possibility of modelling the initiation and propagation of cracks along an arbitrary, solution-dependent path within bulk materials without tying it to the element boundaries.

After studying numerical damage modelling techniques, the literature review focused on their use in modelling skin-stringer separation behaviour during post-buckling. Chapter 3 provides insights from various computational studies on composite stiffened panels using the aforementioned techniques. The studies found that VCCT and CZM were primarily used to predict post-buckling behaviour. While finite element models could predict post-buckling deformations accurately, they often over-predicted or under-predicted loads leading up to the final collapse. This was because of how the models were defined. To more accurately predict skin/stringer debond influence on post-buckling behaviour, proper calibration of damage evolution parameters is necessary. Intra-laminar damages within composite laminates should also be considered, as matrix cracks can enable the migration of skin/stringer interface delamination to ply delaminations within the skin. Most studies neglected the influence of mode III fracture toughness, which can be a good approximation when mode III-dominated fracture does not occur. However, the predicted damage evolution will be inaccurate when the skin/stringer debond becomes mode III dominated. Similarly, the influence of fibre-bridging on mode I fracture toughness also becomes important when damage evolution is mode I dominated and has to be considered. Finally, the initial imperfections introduced to the finite element model influence the post-buckling mode shapes. The internal load distribution due to different mode shapes, in turn, affects the skin-stringer delamination initiation and propagation. Therefore, geometric imperfections in the test panels should be measured using 3D-DIC and introduced as perturbations to the models.

Upon concluding Chapter 3, it was identified that a significant research gap exists in the literature concerning computational studies on composite stiffened panels. The current body of work is primarily based on VCCT and CZM damage modelling techniques, leaving a void in applying XFEM for modelling skin-stringer separation behaviour in composite stiffened panels. This thesis project presents an opportunity to delve into this under-explored area.

Given the potential of thermoplastic composites to realise highly optimised and recyclable structures, it would be intriguing to consider a thermoplastic stiffened panel for this study. The butt-joined PEKK-FC thermoplastic stiffened panels, as tested by Dooren et al., serve as a suitable candidate for this investigation. The authors provide detailed information regarding the elastic and fracture properties of the materials used in the structure, along with a comprehensive description of the panel geometry.

While the geometric imperfections obtained from the panel using 3D DIC were not reported, a fraction of the mode-1 out-of-plane deformation could be utilised to achieve a closer correlation. Notably, the authors employed VCCT to model the skin-stringer separation behaviour in their study. This implies that the application of XFEM to model the skin-stringer separation in this thesis project could facilitate a comparison between the results obtained using XFEM and the widely used technique of VCCT. Given that moving cracks can be modelled using XFEM in conjunction with linear elastic fracture mechanics principles or with cohesive segments, it is important to narrow the project's scope. As XFEM is being compared to VCCT (based on Linear Elastic Fracture Mechanics) in this study, using the cohesive segments approach of XFEM could provide a unique comparison. Henceforth, the XFEM approach in conjunction with cohesive segments will be referred to as XFEM in this report. Having identified the research goal of the project, to deal with it effectively, it is crucial to formulate precise research questions, which will be the focus of the subsequent section.

4.2. Research Questions

In line with the project goal, the following primary research question has been formulated:

Main Research Question

Can the XFEM damage modelling technique accurately and efficiently model the skin-stringer separation behaviour in a Butt-Joined PEKK-FC thermoplastic stiffened panel?

To answer the primary research question, the following sub-questions have been devised:

Sub Question 1

Does using XFEM to model skin-stringer separation behaviour influence the prediction of post-buckling deformations and the final failure load?

Sub Question 2

Considering the focus on the thermoplastic stiffened panel examined by Dooren et al. and noting the authors used VCCT to model skin-stringer separation behaviour in their study, how does the predicted skin-stringer separation behaviour using XFEM compare with that obtained through the VCCT model?

Sub Question 3

How does the computational efficiency of XFEM compare to that of VCCT?

Sub Question 4

How do the XFEM and VCCT damage modelling tools, as implemented in Abaqus, compare in terms of ease of use for the user?

These research questions will guide the investigation in this thesis project and will be considered while devising the research plan in the next section.

4.3. Methodological Framework for the Project

A three-stage research plan was devised to answer the research questions and achieve the research objective.

The first stage involved conducting an extensive literature study to identify research gaps, develop a research goal, frame the research questions, and gather the necessary knowledge to answer these questions. This has been documented in the report so far.

The second stage will involve familiarising oneself with the commercial implementation of the damage modelling techniques of VCCT and XFEM. This will be done by modelling simple DCB specimens. An experimental exercise is beyond the scope of this thesis project. Therefore, the material, fracture, and geometric properties for the DCB models will be obtained from the characterisation study carried out by Tijs et al. on AS4D/PEKK-FC DCB specimens [55]. To validate the results predicted using the finite element models, an analytical formulation based on Linear Elastic Fracture Mechanics will be used to obtain a load-displacement curve for the DCB specimen under consideration, which will serve as a benchmark. This project stage will conclude by comparing the results obtained using the two damage modelling techniques. Part II of this thesis report will provide a description of the DCB models and the results obtained using these models.

Guided by the modelling experience gained by creating coupon-level models, the project's third stage, which pertains to modelling multi-stringer stiffened panels, will be carried out. As mentioned in section 4.1, the post-buckling behaviour of the PEKK-FC thermoplastic stiffened panel, as studied by Dooren et al., will be replicated during this thesis study using the damage modelling techniques of VCCT and XFEM. Firstly, the VCCT-based finite element model created by Dooren et al. will be replicated based on the model description reported by the authors. Then, a parametric study will be carried out on the finite element model by varying the fraction of mode 1 out-of-plane deformations introduced to the panel as imperfections. The suitability of the imperfections will be evaluated based on the predicted load-displacement curves. This exercise is essential given the lack of actual geometric imperfections in the test panels used by Dooren et al. in their study. Upon finding the suitable level of imperfection, the evolution of post-buckling deformations and the predicted skin-stringer separation behaviour will then be compared to the test results reported by Dooren et al. Then, an XFEM-based model will be created using the same level of mode-1 imperfection. Upon creating the models, the results obtained using the XFEM-based model will then be compared with the test results as reported by Dooren et al. and the VCCT-based model created during this thesis project to answer the research questions.

Part II

Double Cantilever Beam (DCB) Specimen Analysis

5

Model Descriptions: DCB Specimens

The Double Cantilever Beam (DCB) specimen is widely used for evaluating pure mode I fracture toughness of unidirectional carbon fibre-reinforced composite materials [26]. This project's second stage involves applying the damage modelling techniques of the Virtual Crack Closure Technique (VCCT) and Extended Finite Element Method - Cohesive Segments Approach (XFEM) to model DCB specimens. The DCB specimen's simplicity allows a better understanding of these modelling techniques and their limitations. Once a robust modelling strategy is established with DCB specimens, the study will progress to a more complex multi-stringer stiffened panel analysis.

DCB specimens made using AS4D/PEKK-FC were selected due to the availability of material, fracture and geometric properties from the characterisation study conducted by Tijs et al. [55]. The resultant load-displacement curve will be derived using an analytical formulation to serve as a benchmark for comparison. The models made using VCCT and XFEM damage modelling methodologies will then be validated by comparing the resultant load-displacement curves with the ones obtained using the analytical formulation. The following sections will provide a detailed description of the DCB specimen used for quasi-static delamination analysis (section 5.1) and an explanation of the modelling approaches adopted for quasi-static delamination analysis using VCCT (section 5.2) and XFEM (section 5.3). The results derived from these analyses will be presented in the subsequent chapter.

5.1. DCB Specimen Description

As previously stated, the DCB specimen, described in the characterisation study conducted by Tijs et al., is used for the analysis. The specimen geometry adopted by the authors is presented in Figure 5.1. These DCB specimens measured 100 mm in length and 25 mm in width, with an initial crack length of 48 mm (refer to Table 5.1). The DCB specimens were fabricated using an AS4D/PEKK-FC laminate, comprising 30 unidirectional 0-degree plies (for fracture and material properties, refer to Table 5.2 and Table 5.3, respectively).

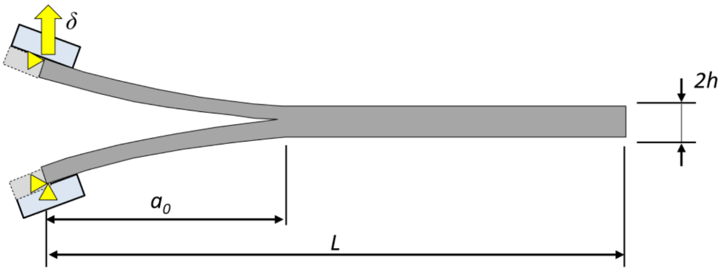

Figure 5.1: Geometric representation of the DCB specimen [55]

Parameter	Value
width [mm]	25
a_0 [mm]	48
L [mm]	100
2h [mm]	4.2

Table 5.1: Geometric parameters of the DCB specimen [55]

G_{IC} (kJ/m^2)	G_{IIC} (kJ/m^2)	G_{IIIC} (kJ/m^2)	η (-)
1.12	2.35	2.35	2.9

Table 5.2: Fracture properties of AS4D/PEKK-FC UD carbon ply composite [55]

E_{1t} (MPa)	E_{1c} (MPa)	$E_{2t} = E_{3t}$ (MPa)	$E_{2c} = E_{3c}$ (MPa)	$\nu_{12} = \nu_{12}$ (-)	ν_{23} (-)
138300	128000	10400	11500	0.316	0.487

Table 5.3: AS4D/PEKK-FC UD carbon ply properties [55]

When the properties of a material are known, an analytical solution derived from Linear Elastic Fracture Mechanics (LEFM) can be used to calculate the load (P) and displacement (δ) for a specific DCB specimen [56]. The calculation requires the use of Equations 5.1 and 5.2, where E_{11} and G_{IC} represent the longitudinal Young's Modulus and Mode 1 fracture toughness of the DCB material, respectively. In addition, the variables "b", "h", and "a" correspond to the width, thickness of a single beam section and the crack length, respectively.

$$P = \sqrt{\frac{G_{IC} b^2 h^3 E_{11}}{12(a + \chi h)^2}} \tag{5.1}$$

$$\delta = \frac{8P(a + \chi h)^3}{b h^3 E_{11}} \tag{5.2}$$

Finally, the terms χ (crack tip correction due to rotation and deflection) and Γ (transverse modulus correction parameter) can be calculated using Equations 5.3 and 5.4. Here, E_{22} and G_{13} in the equations correspond to the Transverse Young's modulus and Shear modulus of the DCB material.

$$\chi = \sqrt{\frac{E_{11}}{11 G_{13}} \left\{ 3 - 2 \left(\frac{\Gamma}{1 + \Gamma} \right)^2 \right\}} \tag{5.3}$$

$$\Gamma = 1.18 \frac{\sqrt{E_{11} E_{22}}}{G_{13}} \tag{5.4}$$

Using the above equations, the force-displacement curve is obtained in the elastic and inelastic regions separately. Within the elastic region, the displacement is obtained as a function of force using Equation 5.2. While in the inelastic region, the crack length (a) is increased from the initial crack length to obtain the force and displacement using Equation 5.1 and Equation 5.2. Having established the analytical solution, the model setup for the VCCT and XFEM based finite element models will be described in the following sections.

5.2. Modelling Approach: VCCT

For the VCCT model, DCB specimens were created using S4R conventional shell elements. Initially, two beams were created as 3D Shell Planar parts, representing the top and bottom beams of the DCB. These were then partitioned to represent the initially cracked and bonded regions. An AS4D/PEKK-FC lamina material was then defined based on Table 5.3. A Shell-type composite section comprising 15 AS4D/PEKK-FC laminae oriented along the 0° direction was defined and assigned to the top and bottom beams. A local orientation was defined, such that the local one direction is along the length of the specimen, and the local two direction is along the width of the specimen.

For the model mesh, three different mesh configurations were considered and are listed below:

1. **Case I:** A coarse mesh configuration with a uniform element size of 1 mm.
2. **Case II:** The element length along the width of the specimen was 1 mm, while the element length along the length of the specimen was varied. The element length was gradually reduced from 1 mm to 0.5 mm in the initially debonded region. The element length was kept uniform at 0.5 mm in the bonded region.
3. **Case III:** A fine uniform mesh of 0.5 mm element length was defined.

To ensure better convergence with VCCT, the top and bottom beam meshes were matched, with the nodes coinciding.

Next, the VCCT fracture criterion was defined as an interaction property. The definition of the VCCT fracture is based on the Benzeggagh Kenane (BK) criterion for mixed-mode behaviour [25]. The fracture criterion is given in Equation 5.5. The criterion states that the interaction between two nodes in contact will fail at the crack tip if it is greater than or equal to 1. The fracture criterion is a ratio between the critical equivalent strain energy release rate G_{equivC}, which is defined in Equation 5.6 and the equivalent strain energy release rate G_{equiv} in Equation 5.7. The equivalent strain energy release rate is computed at each node based on the strain energy release rates for each failure mode (GI, GII, and GIII), which are determined by nodal displacements and forces. The critical equivalent strain energy release rate G_{equivC} is calculated using the fracture properties reported in Table 5.2. A small viscosity factor of 1E-06 was defined to aid in model convergence.

$$f = \frac{G_{equiv}}{G_{equivC}} \geq 1.0 \tag{5.5}$$

$$G_{equivC} = G_{IC} + (G_{IIC} - G_{IIIC}) \left(\frac{G_{II} + G_{III}}{G_I + G_{II} + G_{III}} \right)^{\eta} \tag{5.6}$$

$$G_{equiv} = G_I + G_{II} + G_{III} \tag{5.7}$$

The specimen's behaviour can be affected by the fracture tolerance used to evaluate the fracture criterion. By default, Abaqus uses a fracture tolerance of 0.2 for VCCT. If the fracture criterion (f) at a particular interaction is higher than 1, Abaqus performs a cut-back in the increment size. Sometimes, it may not be computationally efficient to perform a cut-back until the fracture criterion is lowered to 1. Therefore, a tolerance is defined to satisfy the fracture criterion within a set tolerance. To assess the impact of fracture tolerance, the coarse mesh model was tested using three different values: 0.05, 0.1, and 0.2. This is later followed by a mesh convergence study.

To define the interaction between the two beams, a surface-to-surface contact was created, with the lower surface of the top beam as the main surface and the upper surface of the bottom beam as the secondary surface. An automatic contact stabilisation factor of 1E-06 was assigned to the interface, and a small sliding formulation was adopted since VCCT does not support the finite sliding contact formulation. An initial clearance of 1E-06 mm was assigned across the secondary surface to avoid numerical round-off issues. Lastly, the bonding on the secondary surface was limited to the bonded section of the bottom beam. For the interface between the two beams, a "Debond using VCCT" crack was defined with a Ramp debonding force. From the literature study, it was observed that the DCB specimens modelled using the Ramp option showed a more rounded delamination front, similar to the experimentally observed behaviour. This is shown in Figure 3.7. Additionally, the Ramp option is known to improve solution convergence.

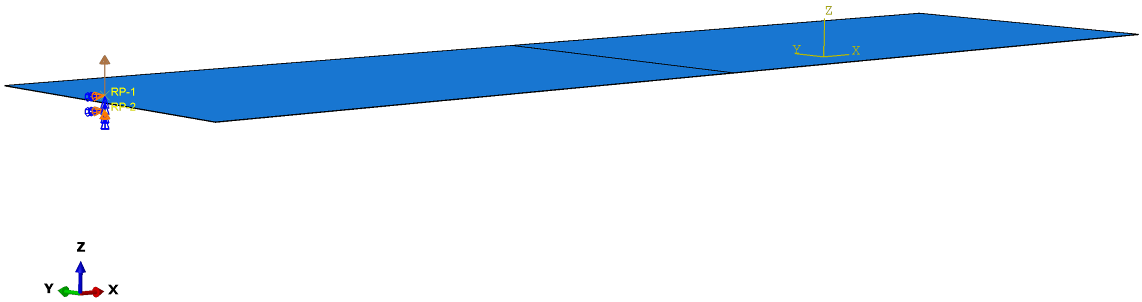

Figure 5.2: Illustration of the boundary conditions and load applied to the DCB model

Two reference points were defined near the front edges of the beam, as shown in Figure 5.2. The front edges of the top and bottom beams were then tied to their respective reference points using rigid body constraints. A Static, General loading step was defined with a time period of 20 seconds. The initial increment size was set to 0.1s, with a minimum increment size of 1E-25s and a maximum increment size of 0.5s. The full

Newton solution technique was adopted for the loading step. Boundary conditions were then set, such that U1=U3=UR1=UR3=0 for RP-2 and U1=UR1=UR3=0 for RP-1 (refer to Figure 5.2). To load the DCB specimen, RP-1 was assigned a velocity of 1mm/s.

5.3. Modelling Approach: XFEM

In the VCCT model, the crack was defined along the contact surface between the top and bottom beam sections. However, this approach is not suitable for the XFEM model for two reasons. Firstly, fracture properties listed in Table 5.2 represent the inter-phase between the top and bottom beam sections. Secondly, when used with 3D models, the implementation of XFEM in Abaqus only considers crack propagation through first-order solid brick elements. As a result, the Abaqus algorithm cannot determine the location of the inter-phase between the two beam sections. Therefore, to model the separation of the two beam sections, the original specimen geometry has to be modified by introducing a section representing the interface between the two beam sections. To achieve this, a 0.3 mm thick solid interface section was introduced in the initially bonded region of the DCB specimen as shown in Figure 5.3. By enriching this section, crack growth will be modelled through the interphase.

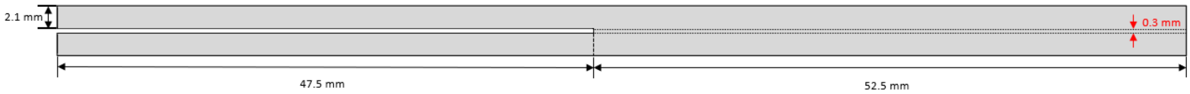

Figure 5.3: Side view of the modified DCB specimen for XFEM

The thickness of the interface was chosen based on several considerations. Firstly, using cohesive law to model damage evolution requires a reasonable number of elements in the fracture process zone (cohesive zone length). A general rule of thumb is to have at least three elements in the cohesive zone. To obtain the approximate cohesive zone length (l_{fpz}) ahead of the crack tip, Equation 5.8 can be used, where E is the material's stiffness, G_c is the fracture toughness corresponding to a particular mode of fracture, and σ_c is the strength of the material.

$$l_{fpz} = \frac{EG_c}{\sigma_c^2} \tag{5.8}$$

It was assumed that the inter-phase between the two beam sections only contained the matrix material, not the fibres. Under this assumption, the interface section was defined as a homogeneous region with a Young's Modulus equivalent to the transverse stiffness of the AS4D/PEKK-FC UD carbon ply material, i.e. set to 10,950 MPa. The Poisson's ratio was assumed to be 0.316. Based on the matrix tensile strength reported by Tijs et al., the material strength of the interface section was defined as 87 MPa [55]. The DCB specimen is used to model pure mode I fracture, and accordingly, the fracture toughness G_{IC} was set to 1.12 kJ/m^2.

Based on the given values, the length of the cohesive zone ahead of the crack tip in the interface area is approximately 1.548 mm. To ensure that there are at least three elements in the cohesive zone, the maximum element length should be 0.516 mm. The aspect ratio of the elements must be considered to achieve better convergence for the enriched elements. This is important because a higher aspect ratio can cause stress calculation issues and element distortion. Considering these factors, the thickness of the interface section was chosen as 0.3 mm.

Regarding the modelling approach, the first step was to create a 3D Solid DCB part using the cross-section shown in Figure 5.3. The depth of the extrude was 25 mm. Then, the DCB part was partitioned to create separate sections representing the interface region, the initially cracked regions, and the bonded regions.

Using the elastic properties from Table 5.3, an AS4D/PEKK-FC UD composite material was created. The interface was defined with an isotropic material with a Young's Modulus of 10950 MPa and a Poisson's Ratio of 0.316. The MAXPS damage criterion was defined to model delamination, with 87 MPa as the critical principal stress. The stress/strain extrapolated to the crack tip was used to determine if the damage initiation criterion was satisfied by setting the position to NONLOCAL [40]. This also means that the stress/strain averaged over a group of elements around the crack tip in the enriched region will be used to determine the crack propagation direction. An Energy type damage evolution criterion was defined with a linear softening behaviour. The linear softening behaviour was chosen, assuming the interface material is linear-elastic, and the material stiffness would degrade linearly as the damage progresses. Knowing that a DCB specimen would exhibit pure mode I fracture, a mode-independent fracture energy of 1.12 kJ/m^2 (G_{IC}) was defined for damage evolution.

Two Solid, Homogeneous sections were defined for the AS4D/PEKK-FC UD composite and the interface, respectively. These were assigned to the corresponding sections in the DCB. A local material orientation was defined such that the local one direction is along the length of the specimen, and the local two direction is along the width of the specimen. To improve the computational efficiency, the composite laminate of the beam sections was idealised as a solid, homogeneous section. If they were defined as composite sections, it would have required each beam to be further partitioned into 15 sections through the thickness, ultimately introducing 15 element layers in each section. By using a solid-homogeneous section, fewer elements are needed through the thickness of the beam. To represent the initial crack tip, a Planar-type 3D shell part was created. The dimensions of the shell part were as shown in Figure 5.4. The initial crack was introduced at the centre of the interface section (refer to Figure 5.5). As a result, the initial crack length becomes 48 mm (47.5 mm + 0.5 mm).

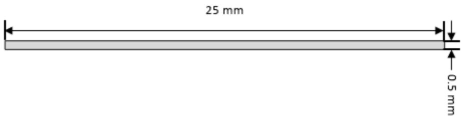

Figure 5.4: 2D Sketch of the crack

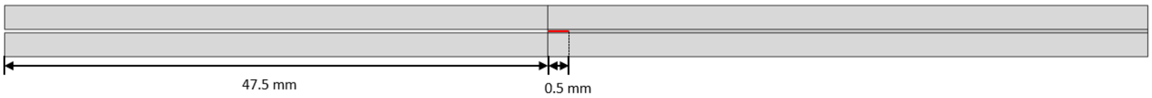

Figure 5.5: Side view of the DCB specimen model assembly (XFEM Model)

In the interaction module, an XFEM type crack was defined using the interface section as the domain and the 3D Shell crack part as the crack location. The crack growth option was also enabled. A Static, General loading step was created with a time period of 20 seconds. The initial increment size was set to 0.01 seconds, while the minimum and maximum increment sizes were 1E-25 and 0.2 seconds, respectively. The full Newton solution technique was selected for the loading step. Two reference points were defined at the centre of the inner edges of the beams as shown in Figure 5.6. Rigid body-tie constraints were assigned to the respective edges of the reference points. The boundary conditions were then defined such that U1=UR1=UR2=0 for RP-1 and U1=U2=UR1=UR2=0 for RP-2. These boundary conditions were defined about the global coordinate system shown on the bottom left in the Figure 5.6. A velocity of V2 = 1 mm/s was introduced to RP-1 to introduce loads to the beam.

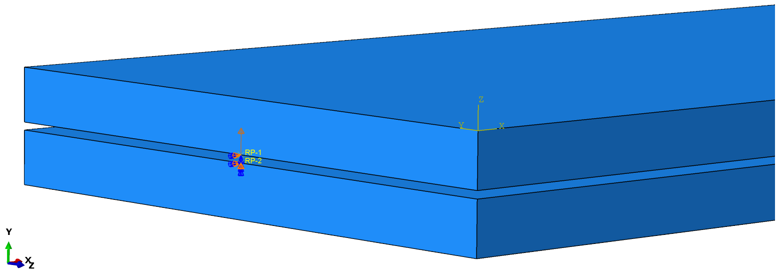

Figure 5.6: Illustration of the boundary conditions and load applied to the DCB-XFEM model

The DCB specimen was modelled using 8-node linear brick - 3D stress elements (C3D8). In the interface region, one element layer was introduced with three different mesh configurations for the specimen. These configurations are listed below:

1. **Case I:** A coarse mesh was created with an element length of 0.4 mm along the width of the specimen. The element size decreased along the length of the specimen, from 1 mm to 0.4 mm in the debonded region. In the bonded region, a uniform size of 0.4 mm was used. Three-element layers were defined through the thickness of each beam.
2. **Case II:** Keeping the same mesh configuration as case I, the element layers in each beam were increased from 3 to 4.
3. **Case III:** For the fine mesh configuration, the case II configuration was modified by reducing the minimum element size along the length of the specimen to 0.3 mm.

Before performing a mesh configuration study, it is important to identify two damage parameters namely, the viscous stabilisation factor and damage initiation tolerance. The viscous stabilisation factor is used to aid in solution convergence in case of any instability arising due to crack initiation and propagation. Damage initiation tolerance is used for a similar purpose as in case of VCCT although here, it is to evaluate whether the critical strength of the material has been reached for damage initiation. Firstly, the damage initiation tolerance is investigated using a low viscous stabilisation factor of 1E-06. Tolerances of 0.05 and 0.1 were evaluated. Abaqus by default uses a 0.05 tolerance. A higher tolerance was not tested because using a tolerance like 0.2 would mean that damage is initiated when the principal stress is 106.8 MPa, which is significantly higher than 87 MPa. A study was performed to find an appropriate stabilisation factor after finding the suitable tolerance. Three viscous stabilisation factors (1E-04, 1E-05 and 1E-06) were tested using the coarse mesh setup. Afterwards, the remaining mesh configurations were tested using the selected parameters of viscous stabilisation factor and damage initiation tolerance.

6

Chapter 6: Delamination Propagation Results

This chapter discusses the results obtained using VCCT and XFEM modelling techniques in section 6.1 and section 6.2 respectively. This is followed by comparing the two modelling techniques in section 6.3.

6.1. DCB Results (VCCT)

Several DCB specimens were created to simulate the growth of delamination. The specifics of these models were explained in detail in section 5.2. As previously mentioned, the effect of fracture tolerance was investigated by testing three different values: 0.05, 0.1, and 0.2. This was done using the coarse mesh configuration. A mesh convergence study was conducted once a suitable tolerance factor was determined. To keep track of the models, a naming convention was introduced: CS{X}_TL{Y} (where X = I, II, III indicates the mesh configuration and Y = 0.05, 0.1, 0.2 indicates the tolerance factor).

The predicted load-displacement curves were evaluated to assess the effect of tolerance. The load-displacement curves obtained from the finite element models showed minor deviation from the analytical solution, as seen in Figure 6.1. The slopes listed in Table 6.1 were compared to the analytical solution, and it was noted that the curves corresponding to 0.05, 0.1, and 0.2 tolerances had higher slopes by 4.14%, 3.02%, and 3.39%, respectively. It was also observed that the models over-predicted the peak load compared to the analytical solution. The table shows that the peak load predicted by The highest error was approximately 2.37% (tolerance of 0.2). The load-displacement curve was analysed closely for further comparison (refer to Figure 6.2). The curve predicted using a tolerance of 0.2 appears to be more erratic than the other two. On the other hand, the curves produced using a tolerance of 0.05 and 0.1 behave similarly.

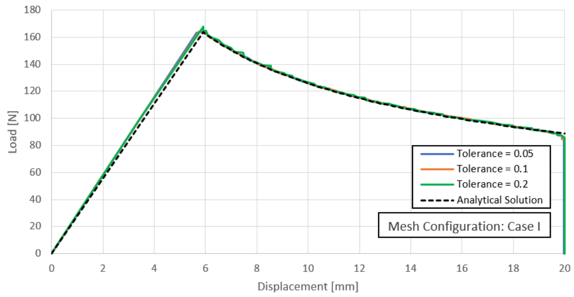

Figure 6.1: Load-Displacement curves obtained from the tolerance study

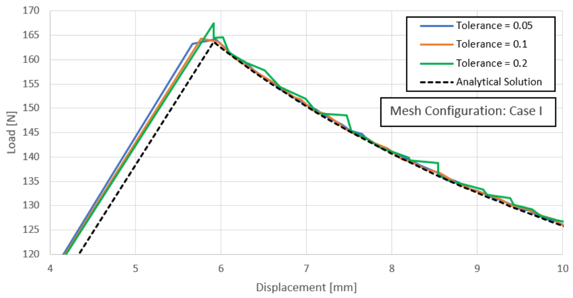

Figure 6.2: Load-Displacement curves obtained from the tolerance study (zoomed)

Curve	Slope [N/mm]	Max Load [N]	Total CPU Time [s]
Analytical Solution	27.670	163.620	-
CSI_TL0.05	28.82	164.242	24136
CSI_TL0.1	28.50	164.364	16444
CSI_TL0.2	28.33	167.5	13602

Table 6.1: Tolerance Study: Comparison of Stiffness, Maximum Load, Displacement and Total CPU Time for Different Cases

Lastly, the total CPU time for each iteration was compared. Based on Table 6.1, it can be seen that the CPU time utilised by models with a tolerance of 0.1 and 0.2 are significantly lower when compared to the model with a tolerance of 0.05. Based on the other comparisons, the tolerance of 0.1 seems more suitable. Firstly, the peak loads and the load-displacement curves obtained with the tolerances 0.05 and 0.1 are closer, while the CPU time is reduced by 31.87%. Secondly, while the CPU time for 0.2 as tolerance is the lowest, the peak load is higher, and the curve is erratic. Considering the trade-offs, it seems reasonable to choose 0.1 as tolerance.

When modelling fracture, a viscous damping parameter is used to help with solution convergence. The value of the viscous damping parameter used for a specific model is typically determined through previous experience or an iterative process. It needs to be high enough to ensure stable incrementation but not so high that it fails to represent the physical behaviour in the fracture region. To determine if the selected viscous damping is appropriate, one can compare the plots of total strain energy in the model (ALLSE) with the damping energy plot (ALLVD). To do so, the curves were plotted for the CSI_TL0.05 model, as the choice of tolerance should not impact the damping energy. The resulting curves are shown in Figure 6.3. It is evident that the damping energy is a small fraction of the total strain energy in the model. Therefore, the choice of 1E-06 as the viscous damping is acceptable.

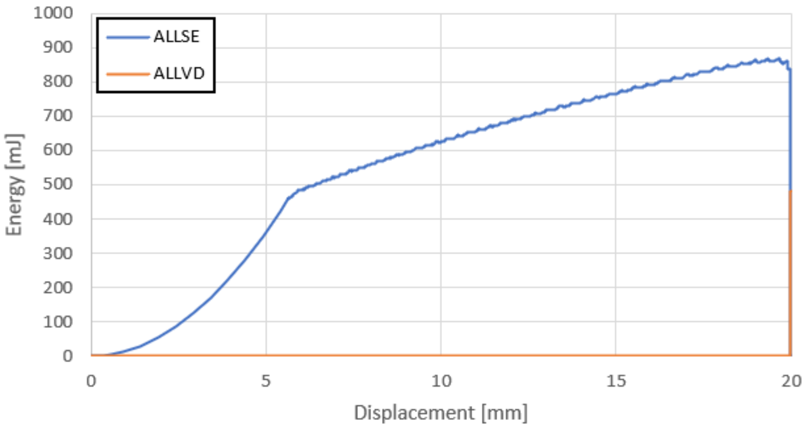

Figure 6.3: ALLSE and ALLVD curves for CSI_TL0.05 model

After determining the appropriate tolerance, the mesh configuration of the model was changed to look for mesh convergence. The load-displacement curves and peak loads obtained for each case were evaluated and compared to verify the solution convergence. The load-displacement curves are displayed in Figure 6.4 and Figure 6.5. The observed variation in the load-displacement curves was minimal. The curve slope continued to be over-predicted, and from Table 6.2, it can be inferred that there was a very slight change in the slope of the curves. The same is true concerning the peak load predicted by the models, which is also over-predicted. The maximum error in the predicted slope and the peak load is 3.02% and 0.45%, respectively (both in the case of the coarse mesh configuration). Given that there was no significant change in the predicted load-displacement behaviour, it was interpreted that the solution has converged.

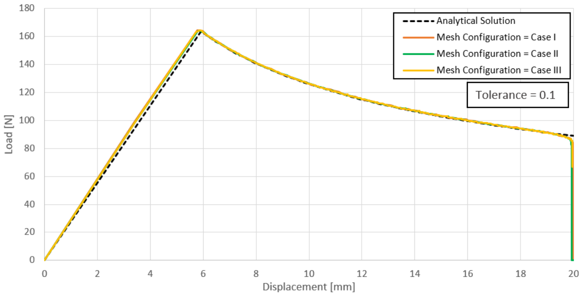

Figure 6.4: Load-Displacement curves obtained from the mesh convergence study

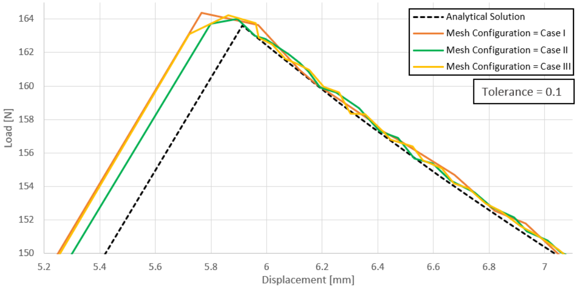

Figure 6.5: Load-Displacement curves obtained from the mesh convergence study (zoomed)

Curve	**Slope [N/mm]**	**Max Load [N]**	**CPU Time [s]**
Analytical Solution	27.67	163.620	-
CSI_TL0.1	28.504	164.364	16444
CSII_TL0.1	28.229	164.002	69440
CSIII_TL0.1	28.502	164.246	332088

Table 6.2: Mesh Convergence Study: Comparison of Stiffness, Maximum Load, Displacement and Total CPU Time for Different Cases

As discussed in section 5.2, the ramp release option for the VCCT crack was chosen to model a rounded delamination front consistent with the physical tests. To evaluate this, bond-state contours for the bottom beam were obtained at approximately 6 mm displacement, where the delamination front begins to propagate. These contours are shown in Figure 6.6, Figure 6.7, and Figure 6.8. It is evident that the delamination front is rounded for all cases, irrespective of the mesh size.

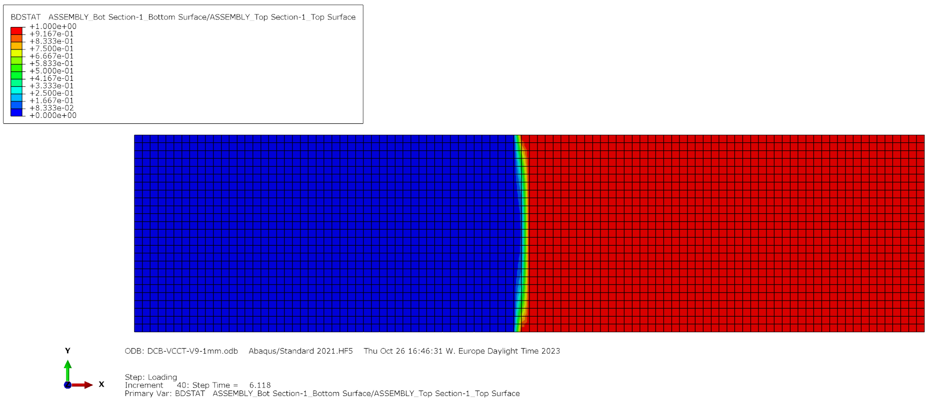

Figure 6.6: Delamination front corresponding to the displacement of 6.118 mm for the model CSI_TL0.1

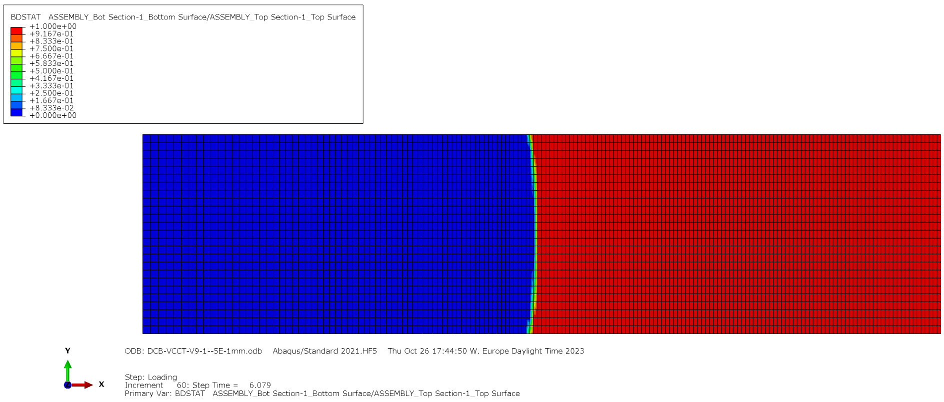

Figure 6.7: Delamination front corresponding to the displacement of 6.079 mm for the model CSII_TL0.1

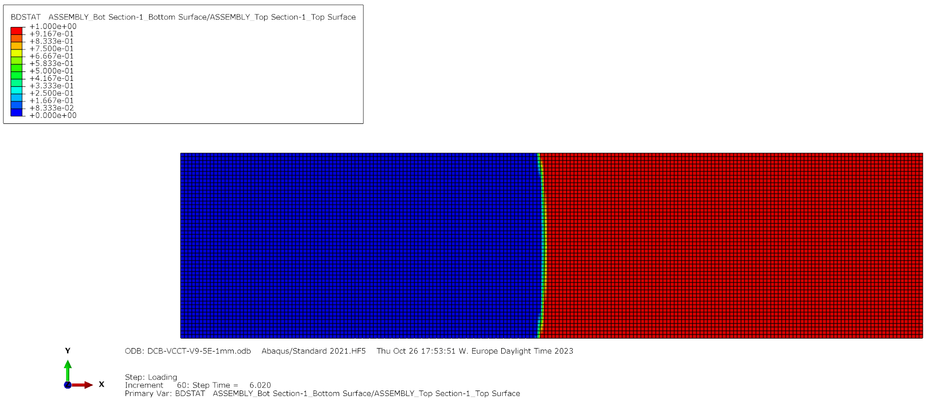

Figure 6.8: Delamination front corresponding to the displacement of 6.020 mm for the model CSIII_TL0.1

Upon closer examination of the load-displacement curve (refer to Figure 6.5), it is observed that there is a fluctuating trend in the non-linear region, although it is not as erratic as in the case of CSI_TL0.2. This trend persists even when using the fine mesh configuration (CSIII_TL0.1). The ramp option selected for the VCCT crack definition gradually releases the bond instead of immediately releasing it when the criterion is met. As a result, the crack front progresses from one boundary of an element to the other, causing a stiffness mismatch. This also explains the increase in the frequency of the fluctuations as the mesh becomes finer. Despite these fluctuations, the load-displacement curve remains very similar to the one predicted by the analytical model on a macro scale.

Lastly, a drop in the load-displacement curves is observed at the end for all cases. This is simply because the crack has propagated through the length of the beam (shown in Figure 6.9).

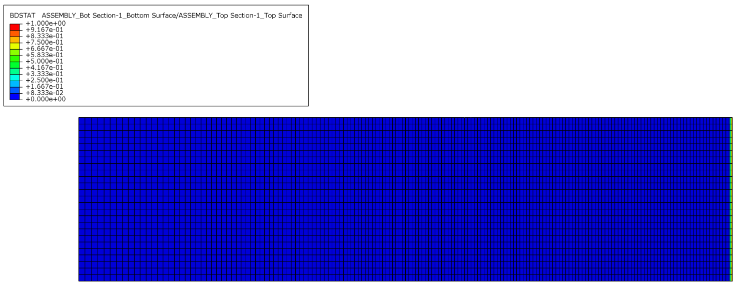

Figure 6.9: The bond state corresponding to 20 mm displacement

6.2. DCB Results (XFEM)

The XFEM models are computationally more intensive compared to the VCCT models. Therefore, for the initial iterations to identify the suitable parameters, i.e. the viscous stabilisation factor and damage initiation tolerance, the loading step's time period was reduced to 10 seconds (i.e., displacement of 10 mm). Only for the mesh convergence study was the time period of 20 seconds used. To keep track of the models, a naming convention was adopted for this study: CS{X}_VS{Y}_TL{Z} (where X = I, II, III, ... indicates the mesh configuration; Y = 1E-04, 1E-05, 1E-06 indicates the viscous stabilisation factor and Z = 0.05, 0.1 indicates the damage initiation tolerance).

Initially, a study was conducted to determine the damage initiation tolerance factor using the lowest viscous stabilisation factor, 1E-06, along with the coarse mesh configuration. The suitability of the damage tolerance factor was assessed based on the load-displacement curves and the total CPU time. The load-displacement curves for models CSI_VS1E-06_TL0.05 and CSI_VS1E-06_TL0.1 are illustrated in Figure 6.10 and Figure 6.11.

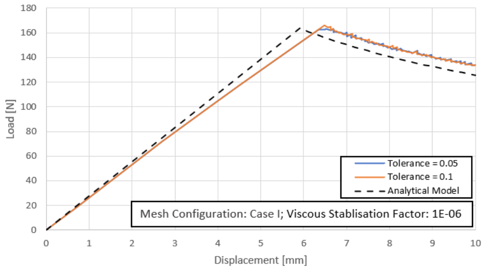

Figure 6.10: Load-Displacement curves obtained from the mesh convergence study

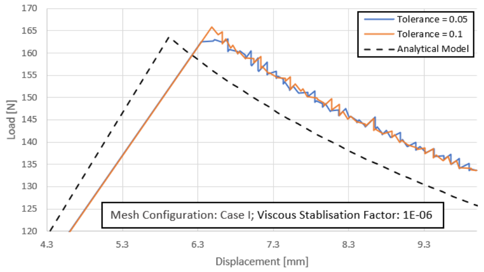

Figure 6.11: Load-Displacement curves obtained from the mesh convergence study (zoomed)

There are three key observations to be made. Firstly, the models under-predicted the stiffness of the specimen. The predicted slopes for the 0.05 and 0.1 damage initiation tolerances had errors of 5.74% and 5.72%, respectively. Secondly, in the non-linear region, the predicted load-displacement curve deviated from the analytical solution. Loads corresponding to any given displacement were over-predicted with a consistent approximate error of 6.14%. Lastly, the predicted maximum load was closer to the analytical model when a tolerance of 0.05 was used, while there was an overshoot of 1.37% when a tolerance of 0.1 was used. Based on the predicted load-displacement curves for the two tolerances, it was determined that there was no significant deviation between them. Hence, the CPU time was used as a metric to choose the appropriate tolerance. Based on this, a damage initiation tolerance of 0.1 was selected for the remaining models.

Model	**Slope [N/mm]**	**Max. Load [N]**	**CPU Time [s]**
Analytical Solution	27.66843174	163.6200095	-
CSI_VS1E-6_TL0.05	26.07975547	163.16	65725
CSI_VS1E-6_TL0.1	26.08564858	165.867	55078

Table 6.3: Summary of results from the damage initiation tolerance factor study

After setting the damage initiation tolerance to 0.1, the coarse mesh configuration was studied with a viscous stabilisation factor of 1E-04, 1E-05, and 1E-06. The load-displacement curves (Figure 6.12 and Figure 6.13) and the total CPU times were compared for all three cases.

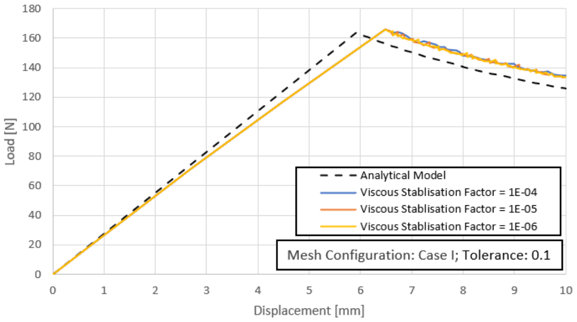

Figure 6.12: Load-Displacement curves corresponding to different viscous stabilisation factors

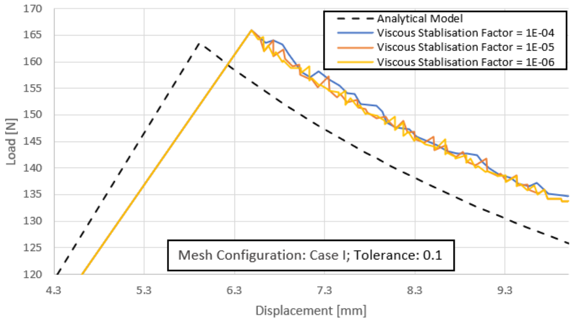

Figure 6.13: Load-Displacement curves corresponding to different viscous stabilisation factors (zoomed)

For all three cases, the predicted slope in the linear region was lower than that of the analytical solution. Additionally, the loads corresponding to any given displacement were over-predicted by approximately 6% in the non-linear region. Although the peak load predicted by all three models was similar, it was still higher than that obtained using the analytical solution. Based on the observations made through the tolerance study, this can be linked to the tolerance used for modelling damage.

In both the tolerance study and the viscous stabilisation study, it was found that the peak load was achieved at a higher displacement as compared to the analytical model. Additionally, it was discovered that the CPU time was the lowest for a viscous stabilisation factor of 1E-04, which was approximately 42.6% lower

Model	Slope [N/mm]	Max. Load [N]	CPU Time [s]
Analytical Solution	27.66843174	163.6200095	-
CSI_VS1E-4_TL0.1	26.08574554	165.875	31618
CSI_VS1E-5_TL0.1	26.0854742	165.868	43348
CSI_VS1E-6_TL0.1	26.08564858	165.867	55078

Table 6.4: Summary of results from the viscous stabilisation factor study

than the 1E-06 case. Therefore, a viscous stabilisation factor of 1E-04 seems like a reasonable choice. But before making the decision, it is important to ensure that the chosen factor isn't too high (similar to the viscous damping parameter used for VCCT). To verify this, the total strain energy (ALLSE) and the damping energy (ALLVD) curves were compared for the CSI_VS1E-4_TL0.1 model (refer to figure Figure 6.14). These plots show that the damping energy used to stabilise the model is a very small fraction of the total strain energy in the model. Hence, 1E-04 was chosen as the viscous stabilisation factor.

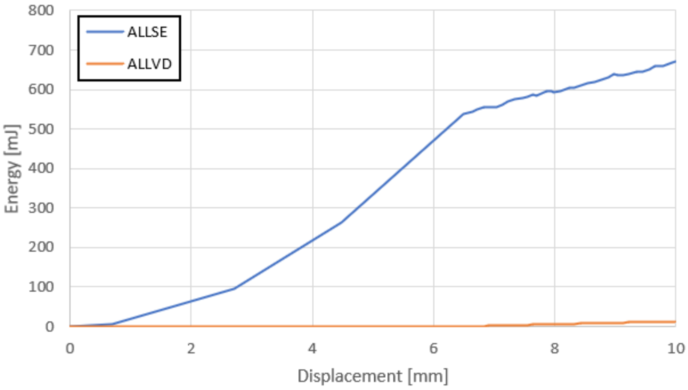

Figure 6.14: ALLSE and ALLVD curves for CSI_VS1E-4_TL0.1 model

A mesh convergence study was carried out after finding the suitable damage parameters. For this, three different mesh configurations were used. These were discussed in section 5.3. The load-displacement curves obtained from the study are shown in Figure 6.15 and Figure 6.16.

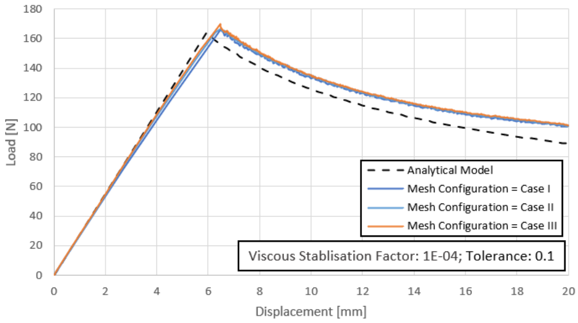

Figure 6.15: Load-Displacement curves obtained from the mesh convergence study

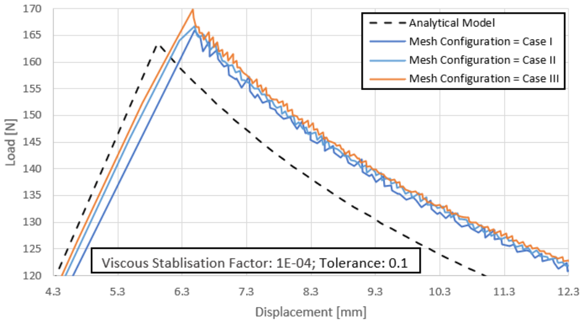

Figure 6.16: Load-Displacement curves obtained from the mesh convergence study (zoomed)

Model	Slope [N/mm]	Max. Load [N]	CPU Time [s]
Analytical Solution	27.66843174	163.6200095	-
CSI_VS1E-4_TL0.1	26.0854742	165.868	156876
CSII_VS1E-4_TL0.1	26.69677307	166.632	202344
CSIII_VS1E-4_TL0.1	27.02669234	169.87	304882

Table 6.5: Summary of results from the mesh convergence study

The load-displacement curves for CSI_VS1E-04_TL0.1 and CSII_VS1E-04_TL0.1 show that adding an element layer to the two beams increases the specimen's stiffness. This is because having more elements through the thickness allows the finite element model to capture the bending and deformation behaviour more accurately. By adding a single element layer to each beam, the error was reduced from 5.74% to 3.51%, but the total CPU time increased by 29%. The predicted slope error was further reduced to 2.32% when the minimum element size along the length of the specimen was reduced to 0.3 mm for CSIII_VS1E-04_TL0.1.

For all the cases studied, there is very little change in the load-displacement curve predicted in the non-linear region. This could be an indication of the solution's convergence. However, there is a consistent issue with the load-displacement curve deviating from the analytical solution in the non-linear region. This could be due to the thickness chosen to model the interface of the DCB specimen. A new model was created to test this theory with a thinner interface of 0.1 mm. However, this resulted in convergence issues. After several attempts, a mesh configuration showed promising results, but the model failed to converge beyond a displacement of 7.228 mm. Nevertheless, this was sufficient to evaluate the theory.

In the model, the element size was 0.2 mm along the width of the specimen. The element size in the initially cracked region along the length of the specimen was reduced from 1 mm to 0.2 mm using a bias, while a uniform element size of 0.2 mm was defined in the bonded region. Three element layers were assigned through the thickness of each beam, while the interface region had only one element layer. For simplicity, the model is referred to as CSIV_VS1E-04_TL0.1. The resulting load-displacement curve is presented in Figure 6.17. The load-displacement curve in the non-linear region is closer to the one predicted by the analytical solution.

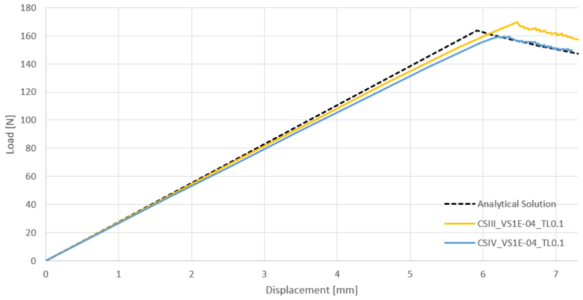

Figure 6.17: Load-Displacement curves for the specimen with reduced interface thickness

Model	Slope [N/mm]	Max. Load [N]	CPU Time [s]
Analytical Solution	27.67	163.6200095	-
CSIII_VS1E-4_TL0.1	27.02669234	169.87	304882
CIV_VS1E-4_TL0.1	26.34	159.53	102054
CV_VS1E-5_TL0.1	27.55	164.66	904194

Table 6.6: Summary of results from study to understand the effect of interface thickness

Further refining the mesh in the interface section could solve convergence issues. However, this would increase the CPU time. An alternate approach would be to model each beam using a single layer of Continuum Shell elements through a composite layup. This should improve the computational efficiency of the model. The element length along the width of the specimen was defined to be 0.2 mm, while the minimum element length along the length of the specimen was defined as 0.1 mm. Continuum Shell elements (SC8R) were used to model the beams, while 3D Stress elements (C3D8) were defined in the interface region. Although the resultant model required approximately 2.96 times higher CPU time than the CSIII_VS1E-4_TL0.1 model, it did not present any convergence issues and could better predict the load-displacement curve. One thing to note is that the viscous stabilisation factor had to be reduced to 1E-05 to achieve a stable model without any convergence issues. This model will henceforth be referred to as CSV_VS1E-05_TL0.1. The obtained load-displacement curve is presented in Figure 6.18, where it is compared to the CSIII_VS1E-4_TL0.1 model.

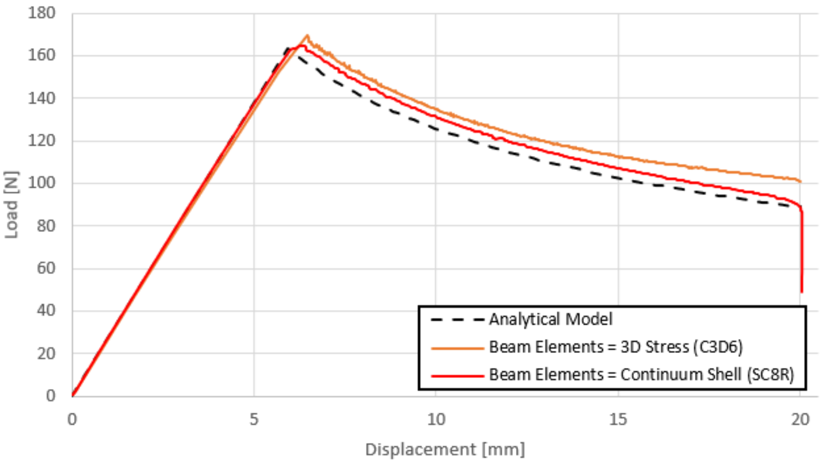

Figure 6.18: Load-Displacement curves for the specimen with reduced interface thickness

It is clear from Figure 6.18 that the stiffness predicted by the continuum shell model is close to the analytical model (with 0.4% error). Furthermore, the specimen's behaviour in the non-linear region differs from the model with 3D Stress elements. The load-displacement curve predicted by the CSIII_VS1E-4_TL0.1 model shows increasing deviation from the analytical solution. On the other hand, although the curve predicted by the model with continuum shell elements is still over-predicted, the error is relatively lower. Near the final failure, the predicted curve is close to the analytical solution. Additionally, there is a load drop at the end of the curve, indicating that the crack has propagated through the length of the specimen. Reducing the thickness of the interface section further would reduce the over-prediction error. However, it would also require further refinement of the mesh in the interface section. This would increase the computation cost. Considering that the maximum error in the load-displacement curve predicted by CSV_VS1E-05_TL0.1 model at approximately 4.23%, the results were considered to be acceptable.

In the non-linear region, the load-displacement curves display small oscillations that are more evident in Figure 6.16. This behaviour can be explained by how the crack initiates and evolves in the enriched region. Initially, when the principal stress in the enriched element reaches a critical level, a crack is initiated, but the element does not immediately lose its stiffness. As the specimen is further loaded, the cracked element is slowly degraded until it completely loses its stiffness. This process is based on a traction-separation law. The evolution process is evident from figures 6.19 through 6.22, where the STATUSXFEM field output contour in the interface section is presented over a series of frames. The undamaged elements (STATUSXFEM=0) are in blue, while the completely damaged elements (STATUSXFEM=1) are in red. As the damage evolves, a stiffness mismatch is created, which in turn causes the oscillations.

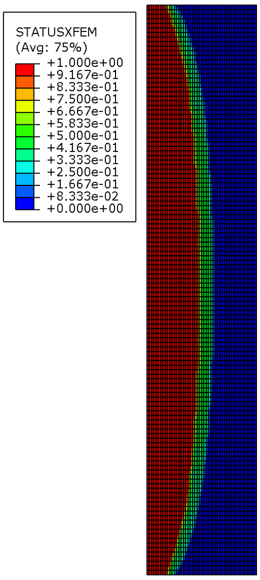

Figure 6.19: STATUSXFEM contour at displacement 6.477 mm (CSV_VS1E-5_TL0.1)

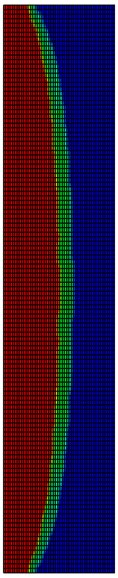

Figure 6.20: STATUSXFEM contour at displacement 6.524 mm (CSV_VS1E-5_TL0.1)

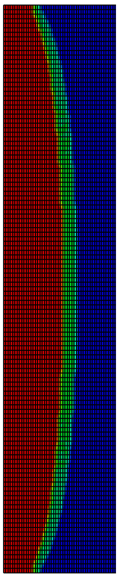

Figure 6.21: SSTATUSXFEM contour at displacement 6.565 mm (CSV_VS1E-5_TL0.1)

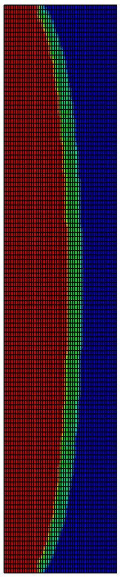

Figure 6.22: STATUSXFEM contour at displacement 6.610 mm (CSV_VS1E-5_TL0.1)

The delamination occurring at 20 mm displacement was analysed for the CSV_VS1E-5_TL0.1 and CSIII_VS1E-4_TL0.1 models. To do so, the STATUSXFEM contour was taken into consideration for the interface sections, as shown in figures Figure 6.23 and Figure 6.24. The XFEM-based model predicts a delamination front that is similar to the experimentally observed rounded delamination fronts. However, there is a difference in the delamination evolution obtained by the model with 3D stress elements and the continuum shell elements. At 20 mm displacement, the CSIII_VS1E-4_TL0.1 model predicts that the delamination has propagated by 42.6 mm, leaving the rest of the interface section undamaged. An attempt was made to run the model for a larger displacement, but the model encountered convergence issues shortly after 20 mm. On the other hand, the model with continuum shell elements in the beam sections and a 0.1 mm interface predicted that the delamination would propagate until the end of the specimen. However, this model also faced convergence issues beyond this point, leaving a small portion of the interface undamaged.

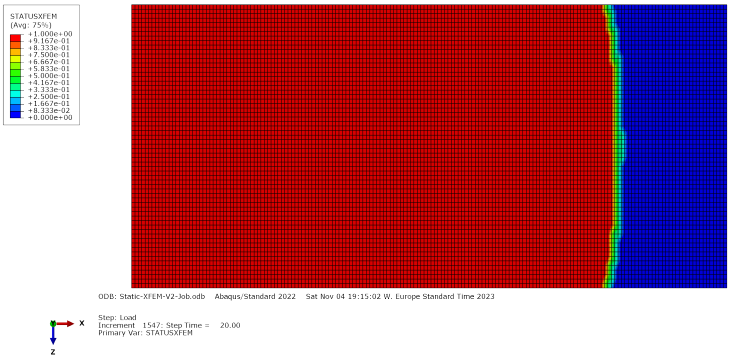

Figure 6.23: STATUSXFEM contour at displacement 20 mm (CSIII_VS1E-4_TL0.1)

Figure 6.24: STATUSXFEM contour at displacement 20.04 mm (CSV_VS1E-5_TL0.1)

In summary, although the CSIII_VS1E-04_TL0.1 model with 3D stress elements in the entire specimen showed mesh convergence, it underestimated the specimen stiffness, overestimated loads in the non-linear region, and had solution convergence problems beyond 20 mm displacement. The CSIV_VS1E-04_TL_0.1 model showed that reducing the specimen's thickness to 0.1 mm could improve the results. However, it was unstable and required further mesh refinement. A mesh refinement would increase the computation cost. To improve computational efficiency, the 3D Stress elements in the beams were replaced with a single element layer of continuum shell elements. The resulting CSV_VS1E-05_TL0.1 model, with a 0.1 mm interface, showed a significant improvement in terms of solution convergence. It predicted that the delamination would propagate close to the specimen's end and closely predicted the analytical model's stiffness, with an error of 0.4%. In the load-displacement curve, a maximum error of approximately 4.23% was observed in the non-linear region. Although the CSV_VS1E-05_TL0.1 model required approximately 2.96 times higher computational requirements than the CSIII_VS1E-04_TL0.1 model, it provided a more accurate prediction of the load-displacement curve without any convergence issues. Therefore, the study concludes that the CSV_VS1E-05_TL0.1 model is the best choice for further comparison with the VCCT-based DCB model, which will be made in the next section.

6.3. Comparison of VCCT and XFEM Based Models

This section compares the results obtained from two different damage modelling techniques of VCCT and XFEM. The total delamination of both models was studied, as shown in Figure 6.9 and Figure 6.23. To begin with, both models can replicate the experimentally observed rounding of the delamination front. In terms of the extent of delamination, in the VCCT model, the delamination between the two beams propagated to the end of the specimen. However, in the XFEM-based model, delamination had only extended by 51.9 mm, leaving the last 0.6 mm of the specimen undamaged. This difference was considered minor and can be attributed to the introduction of the solid interface section in the model. This theory is supported by comparing the XFEM-based models CSV_VS1E-05_TL0.1 and CSIII_VS1E-04_TL0.1, which have different interface thicknesses. It was observed that reducing the thickness of the interface section to 0.1 mm resulted in a closer prediction of the specimen behaviour and a further extension of the delamination front when compared to the specimen with a 0.3 mm thick interface, as shown in Figure 6.23 and Figure 6.24.

The load-displacement curves generated using the VCCT and XFEM-based models were compared to an analytical model used as a benchmark solution. The comparison is shown in Figure 6.25. The VCCT-based model over-predicted the stiffness in the linear region by 3.77% but closely predicted the non-linear load-displacement behaviour. On the other hand, the XFEM-based model very closely predicted the stiffness in the linear region with a 0.414% under-prediction. However, it over-predicted the curve in the non-linear region. It is worth noting that the magnitude of load over-prediction reduces at higher displacements, with a maximum error close to 4.23%. The XFEM and VCCT-based models predicted peak loads of 164.66 N and 164.246 N, respectively. These values were close to the analytical peak load of 163.63 N, with errors of 0.63% and 0.38%, respectively. One key observation is that both models present the peak loads at a higher displacement (6.31 mm for the XFEM model and 5.86 mm for the VCCT model) when compared to the analytical model (4.82 mm).

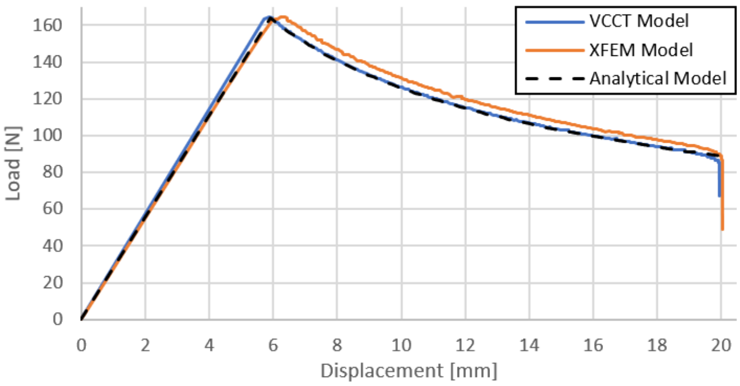

Figure 6.25: Load-Displacement curves obtained using VCCT and XFEM models

Lastly, the CPU times of the two models were compared. The VCCT-based model had a total CPU time of 332088 seconds, while the XFEM-based model had a total CPU time of 904194 seconds. This indicates that the XFEM model is considerably more computationally expensive, taking approximately 2.723 times more CPU time than the VCCT model. This could be attributed to the way damage is modelled using enriched elements. The XFEM model assigns additional degrees of freedom in the enriched regions to model crack initiation and evolution in the region, thereby increasing the number of unknowns in the system of equations. Furthermore, in addition to initiating damage and tracking its evolution, the model must predict the crack deflection angle whenever the damage initiation criterion is met, making the XFEM model more expensive. Lastly, as evident from section 6.2, the XFEM-based models present challenges with solution convergence. These challenges could be overcome by using a fine mesh in the enriched region. This is because a sufficient number of elements have to be defined in the cohesive zone, and the aspect ratio of the elements must also be considered. In summary, these factors add up to increase the computational cost of the XFEM model, making it more expensive than the VCCT model.

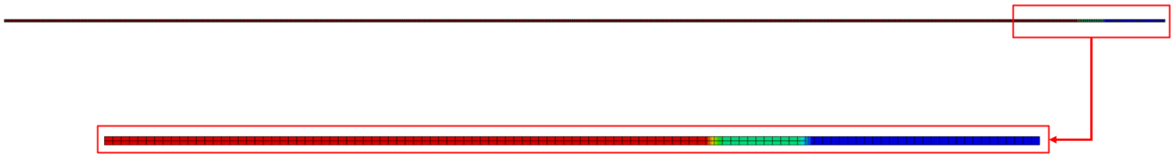

Figure 6.26: Side view of the crack path predicted by the XFEM model in the solid interface

In principle, the XFEM-based model has certain advantages over the VCCT model. The VCCT model is limited to predicting damage evolution at the interface between two parts since it is a contact-based fracture definition. XFEM, on the other hand, uses phantom nodes with additional degrees of freedom in solid brick elements to capture the complex crack path through a 3D interface. However, in the case of the DCB specimen, the crack path predicted by the XFEM-based model was straight (refer to Figure 6.26), as pure mode I fracture occurs in DCB specimens. As a result, the additional computational resources required for modelling the XFEM-based DCB model can be viewed as overkill, and a VCCT-based model would suffice for predicting specimen behaviour. However, this may not be the case with the stiffened panel, where complex mix-mode damage can be expected to occur along the skin-stringer interface. In such scenarios, the added computational expense of using XFEM could be justified by the ability to model the complex crack path through the skin-stringer interface. Nevertheless, it is important to note that problems related to solution convergence and stability, which were observed while modelling the XFEM-based DCB model, could also arise when modelling the stiffened panel using XFEM.

Part III

Multi-Stringer Panel Analysis

7

Chapter 7: Model Descriptions: Stiffened Panel

Having understood and developed the modelling strategies for implementing VCCT and XFEM, these techniques were used to model a multi-stringer stiffened panel. The stiffened panel under consideration is the one tested and modelled by Dooren et al. [50]. A detailed panel description is given in section 7.1. The model descriptions for the VCCT and XFEM models follow this in section 7.3 and section 7.4.

7.1. Panel Description

The panel considered by Dooren et al. was a three-stringer thermoplastic composite stiffened panel. It comprised three stringers that were connected to the skin using a butt joint. Each stringer consisted of a vertical web and an angled side cap (105° with respect to the web). To introduce load, the panel had two epoxy potting tabs at both ends. The panel is shown in Figure 7.1, and a 2D sketch of the panel is presented in Figure 7.2. The panel was 495.3 mm long (including potting) and 445.3 mm between potting, with a width of 344.8 mm and a stringer spacing of 152.4 mm. The web height was 28 mm, and the cap width was 15 mm. The butt joint was created with an injection-moulded short-fibre reinforced polymer (SFRP) filler material. An artificial damage of 70 mm was created between the bottom of the filler and the top of the skin at the middle stringer to represent Barely Visible Impact Damage (BVID). The red area in Figure 7.1 highlights the damage.

Figure 7.1: Thermoplastic Composite Stiffened Panel used by Dooren et al. for their study [50]

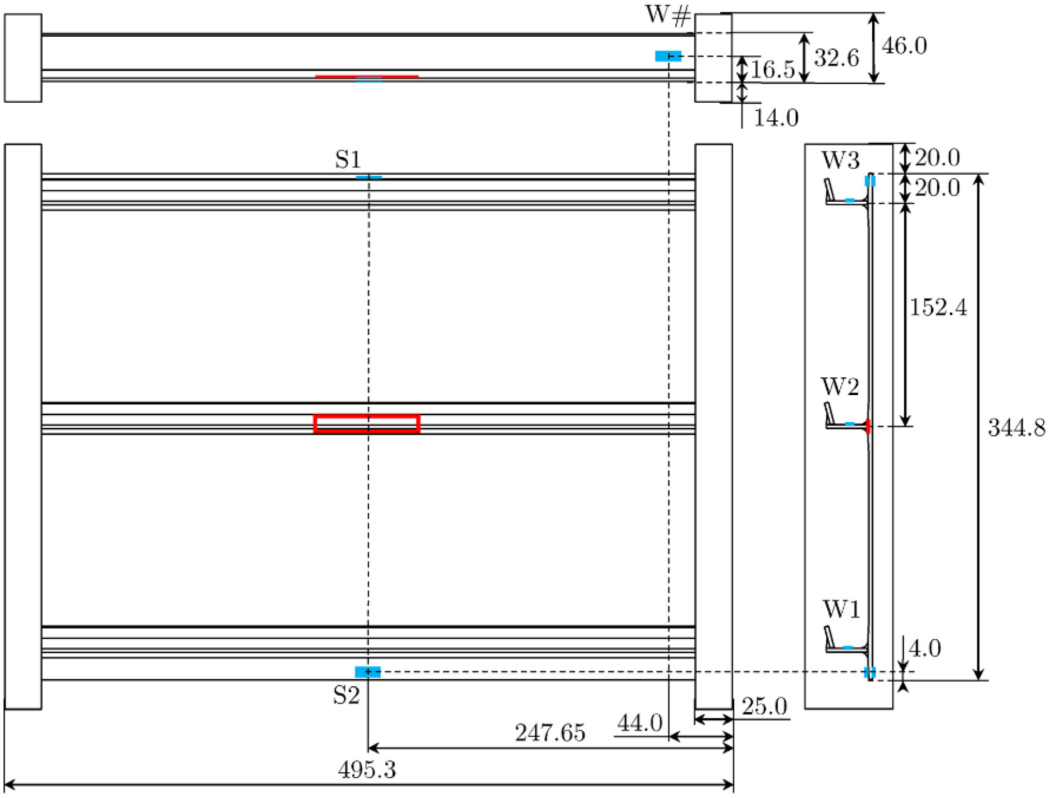

Figure 7.2: 2D Sketch of the Thermoplastic Composite Stiffened Panel [50]

Material	**E_{11} [MPa]**	**E_{22} [MPa]**	**ν_{12} [-]**	**G_{12} [MPa]**	**ρ [kg/m^3]**	**t_{ply} [mm]**
AS4D/PEKK-FC carbon UD ply	126100	11200	0.3	5460	1560	0.138
PEKK glass fabric	25000	25000	0.3	3000	2200	0.1
PEKK carbon SFRP filler	13252	6570	0.42	2389	1560	0.138

Table 7.1: Material Properties as reported by Dooren et al. [50]

G_{IC} $[kJ/m^2]$	**G_{IIC}**$[kJ/m^2]$	**G_{IIIC}**$[kJ/m^2]$	η
1.41	1.9	1.9	2.3

Table 7.2: B-K fracture properties of the skin-stringer interface [50]

XT [MPa]	**XC [MPa]**	**YT [MPa]**	**YC [MPa]**	**SC [MPa]**
2559	1575	83.1	284	99

Table 7.3: Strength properties of AS4D/PEKK-FC carbon UD ply [50]

XT [MPa]	**XC [MPa]**	**YT [MPa]**	**YC [MPa]**	**SC [MPa]**
304	200	304	200	50.4

Table 7.4: Strength properties of PEKK glass fabric [57]

All laminated sections were manufactured using AS4D carbon fibre-reinforced Fast Crystallising PolyEtherKetoneKetone (PEKK-FC). The butt joint filler was made from short carbon fibre-reinforced PEKK material. The material properties of the AS4D/ PEKK-FC UD, PEKK glass fabric, and the filler, as reported by Dooren et al., are shown in Table 7.1. The fracture properties of the skin stringer interface are given in

Table 7.2. The laminated sections consist of quasi-isotropic layups as described in Table 7.5. The skin has three distinct layups, L1, L2, and L3, named due to the extra glass fabric plies in the stringer area. Refer to Figure 7.3 for a visual representation of layup in each skin-section.

Section	Thickness [mm]	Layup
Skin L1	2.484	$[45/-45/0/45/90/-45/45/0/-45]_s^C$
Skin L2	2.684	$[0_2]^G[45/-45/0/45/90/-45/45/0/-45]_s^C$
Skin L3	2.884	$[0_4]^G[45/-45/0/45/90/-45/45/0/-45]_s^C$
Web	2.484	$[45/90/-45/0/45/0/-45/0/45/-45]_s^C$
Cap	2.76	$[45/90/-45/0/45/0/-45/0/0/90]_s^C$

Table 7.5: The thicknesses and layups of panel sections (superscripts C and G, stand for carbon and glass plies respectively) [50]

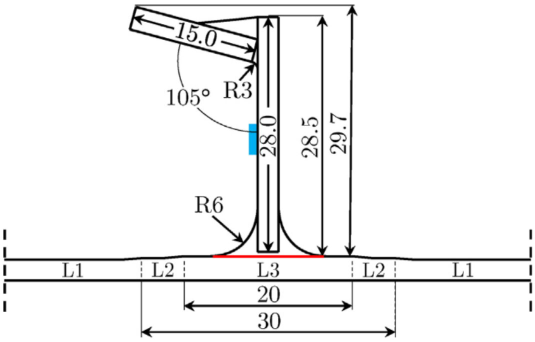

Figure 7.3: Visual representation of the layup in each skin-section [50]

7.2. Geometrical Imperfections

Since the geometric imperfections present in the test panels were not available for use in this thesis study, a fraction of mode 1 deformations were considered imperfections. Therefore, a linear buckling eigenvalue analysis was performed using a reference load of 1N to determine the buckling shape for the first mode. The resulting out-of-plane displacement field was stored in a node file and later used to define the imperfections for the non-linear analysis. The mode shape obtained from the linear buckling analysis is presented in Figure 7.4. The buckling load corresponding to mode one bucking was predicted to be 97.747 kN. For mode 1, Dooren et al. reported a buckling mode shape corresponding to Figure 7.5 for a numerically obtained buckling load of 100 kN. It can be observed that the eigenvalue analysis does reproduce the mode 1 buckling shape with three half waves per bay, with the out-of-plane direction of the half waves being anti-symmetric with respect to the middle stringer. The buckling load corresponding to mode 1 obtained from the eigenvalue analysis was 2.253% less than the 100 kN reported by the authors. This difference was not considered significant, and no further investigation was carried out.

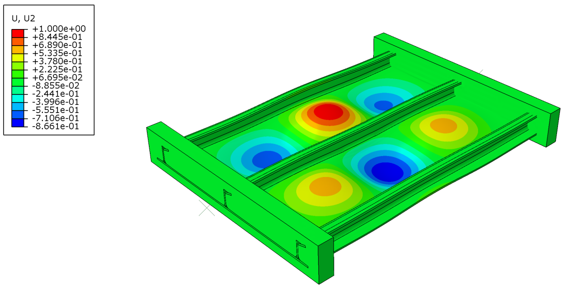

Figure 7.4: Mode 1 buckling shape obtained from the eigenvalue analysis

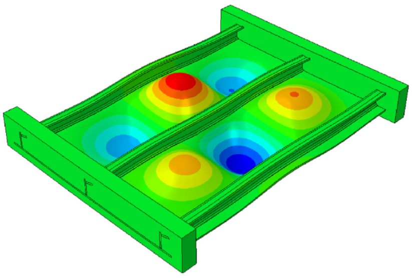

Figure 7.5: Mode 1 buckling shape reported by Dooren et al. [50]

As evident from the literature study, introducing imperfections in the form of linear perturbations of the deformation field obtained from the eigenvalue analysis effectively influences the post-buckling behaviour [51]. Therefore, a percentage of out-of-plane displacements corresponding to mode 1 were considered as imperfections for this study. The percentage of displacements introduced as perturbations varied between 0% and 10% with 2.5% increments. The resultant load-displacement curves and out-of-plane deformations were compared with those reported by Dooren et al. [50].

7.3. Finite Element Model Description: VCCT

The stiffened panel described in section 7.1 was simplified for the finite element model. The skin and the stringers were modelled individually and connected using a contact definition. This is also required for the VCCT fracture definition since it is defined as an interaction property at the interface. Lastly, butt-joint filler geometry at the skin-stringer interface was simplified, as seen when comparing Figure 7.3 and Figure 7.6. The filler region at the interface was meshed with hexahedral elements due to their superior contact interface representation, smoother stress profile, and avoidance of shear locking. However, due to the curved surface of fillets, accurately meshing these regions with hexahedral elements is challenging. Therefore, the fillet geometry near the interface was simplified, assuming it would not significantly impact the panel's structural behaviour.

The skin, stringer and tab geometries were defined as 3D solid parts. The cross-section of the stringer was partitioned into smaller sections to define the individual members, i.e. cap, web, and filler regions. Further partitions were created in the filler regions to have control over the element shape. Partitions were created to define the regions with layups of Skin L1, Skin L2, and Skin L3 in the skin. Lastly, partitions were created in the regions with Skin L3 layup to improve the mesh convergence by ensuring that the nodes of the elements at the skin-stringer interface coincide. The resulting cross-sections of the skin and the stringer after partitioning are illustrated in Figure 7.6 and Figure 7.7.

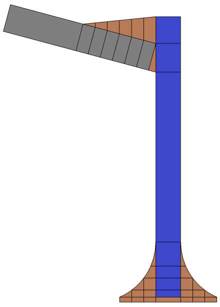

Figure 7.6: Cross-sectional view of the Stringer after partitioning

Figure 7.7: Cross-sectional view of the Skin after partitioning

Next, the material definitions for AS4D/PEKK-FC UD, PEKK glass fabric and PEKK carbon SFRP filler were created using Table 7.1. Based on Table 7.5, composite layups were defined for the web, cap, Skin L1, Skin L2 and Skin L3. These layups were defined for continuum shell-type elements. The layup orientation was defined such that the 0-degree fibres align along the length of the individual member while the 90-degree plies align along the member's width. Lastly, a Solid, Homogeneous section was defined using the PEKK Filler Material for the filler sections.

In their study, Dooren et al. investigated mesh convergence by testing different sizes from 1.25 mm to 2.5 mm [50]. They discovered that a mesh size of 2.5 mm was sufficient for obtaining a converged solution while still being computationally efficient. Thus, for this study, a 2.5 mm mesh size was utilised to model the panel. For the potting tabs, a uniform mesh of 5 mm was used. The panel's laminated sections were modelled using continuum shell elements (SC8R), while the filler sections at the skin-stringer interface were modelled using solid brick elements (C3D8I) with wedge elements (C3D6) for better bending behaviour. For better computational efficiency, solid brick elements with reduced integration (C3D8R) were used for the remaining filler sections and the potting tabs.

Shared nodes were used at the interface between the skin and the stringers to ensure better mesh convergence and computational efficiency. The outer stringers were joined to the skin using a contact property definition with a rough friction formulation for tangential behaviour control and a "Hard" contact pressure-overclosure definition for normal behaviour management. To partially bond the interface between the middle stringer and the skin, a contact pair definition with VCCT was used. The interface has an initial damage of 70 mm in length in the middle, assumed to be present only between the filler and the skin. The growth of the damage will be restricted to the interface. The model does not consider any possible crack growth into the filler due to the limitations of VCCT. This assumption is based on the failure behaviour observed by GKN Fokker through their internal tests and three-point bending tests by Baran et al. [23].

Like the DCB specimen, the VCCT definition for the panel utilised the Benzeggagh Kenane (BK) criterion [25]. The fracture toughness for modes I, II, and III are reported in Table 7.2. Dooren et al. report that these properties were obtained using the tests performed by GKN Fokker for modes I and II. The mode III fracture toughness is assumed to be equal to the mode II fracture toughness, and the BK parameter, η was obtained by the authors based on the data available in the literature for a similar material.

The VCCT fracture was defined using a default fracture tolerance of 0.2 and an unstable crack growth tolerance of 10. The unstable crack growth tolerance was defined to improve convergence and computational efficiency when an unstable crack growth occurs by limiting the number of nodes released simultaneously when the fracture criterion is met. Furthermore, a low viscosity factor of 1E-06 was used to achieve better convergence. To stabilise both loss of contact and separation, a stabilisation factor of 1E-06 was defined.

The contact definitions were based on node-to-surface discretisation, with the skin surface acting as the primary surface and the stringer surface as the secondary surface. For the contact definitions of the outer stringers, a finite sliding formulation was used, while for the middle stringer, a small sliding formulation was used to be compatible with VCCT. Moreover, for the VCCT definition, an initial clearance uniform across the secondary surface of 1E-08 was defined, and the bonding to the secondary nodes was limited to the initially bonded area of the middle stringer surface. Lastly, a "Debond using VCCT" type crack was defined using the RAMP option. The RAMP option was chosen for the same reasons as in the case of the DCB model, i.e. to have a rounded crack front. Additionally, the Hashin fibre and matrix failure criterion was defined using the strength properties from Table 7.3 and Table 7.4 to account for damage in the composite laminate.

A Dynamic, Implicit-Quasi-static loading step was initiated with a 1-second time period. The initial and maximum increment sizes were set to 0.01 seconds, while the minimum increment size was set to 1E-08 seconds. To aid in convergence, the general solver controls for the loading step were modified by increasing the maximum number of cut-backs allowed for an increment (represented by the parameter I_A) from the default value of 5 to 15.

The two potting tabs were introduced to the panel assembly using an embedded region type constraint. Two reference points were then defined 30 mm away from the front and rear end of the panel and were tied to the respective tab surfaces using rigid body constraints. Boundary conditions were defined for the two reference points. At the rear end (RP-2), all degrees of freedom were restricted to prevent movement, while at the front end (RP-1), all degrees of freedom except the one along the longitudinal direction were restricted. A displacement-controlled load of 3 mm was introduced to the panel (RP-1) along the longitudinal direction. Refer to Figure 7.8 to better understand the boundary conditions.

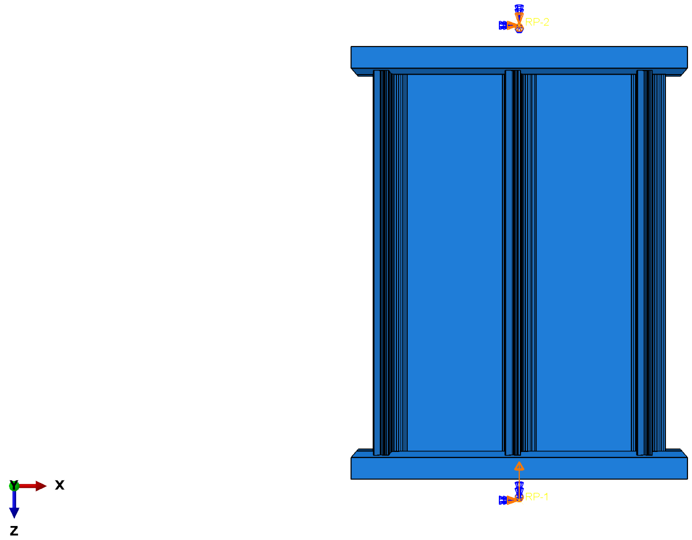

Figure 7.8: Visual representation of the boundary conditions defined for the VCCT Panel

7.4. Finite Element Model Description: XFEM

For modelling the panel using XFEM, the modelling approach used for the VCCT-based panel was utilised with some modifications to make it suitable for the damage modelling technique. This section details the modifications made to the model. To begin with, VCCT allowed the delamination to be modelled along the interface, i.e. the contact surfaces between the skin and the filler section of the stringer. In contrast, the XFEM approach can only be used to model the initiation and growth of cracks through first-order solid elements. Fortunately, unlike the DCB specimens, there is a 0.5 mm interface between the skin and the stringer. This interface region is part of the butt-joint filler. Therefore, a 70 mm long crack was introduced within this interface section as illustrated in Figure 7.9.

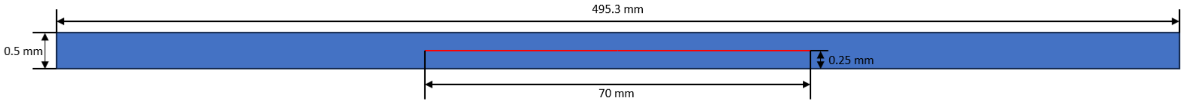

Figure 7.9: Side view of the interface section with the initial crack

The enriched regions where the crack is modelled using XFEM must contain a fine mesh. To estimate the element size, the cohesive zone length ahead of the crack tip was first estimated using Equation 5.8 as shown in Equation 7.1. In Equation 7.1, mode 1 fracture toughness was used for a conservative estimate. To introduce at least three elements in the cohesive zone ahead of the crack tip, the maximum element length has to be limited to approximately 0.787 mm. To achieve this element length, the interface section of the middle stringer was modelled as a separate part and was connected to the stringer and the skin using surface-to-surface tie constraints. The aim was to define an independent mesh in the interface section. In addition to the interface section, the fillet region of the butt-joint filler is defined with fine mesh. For the same reason, no partitions were created in the fillet region of the middle stringer as illustrated in Figure 7.10.

$$l_{fpz} = \frac{E_{11} * G_{IC}}{\sigma_c} = \frac{13252 \times 1.14}{89} \approx 2.36 \text{ mm} \tag{7.1}$$

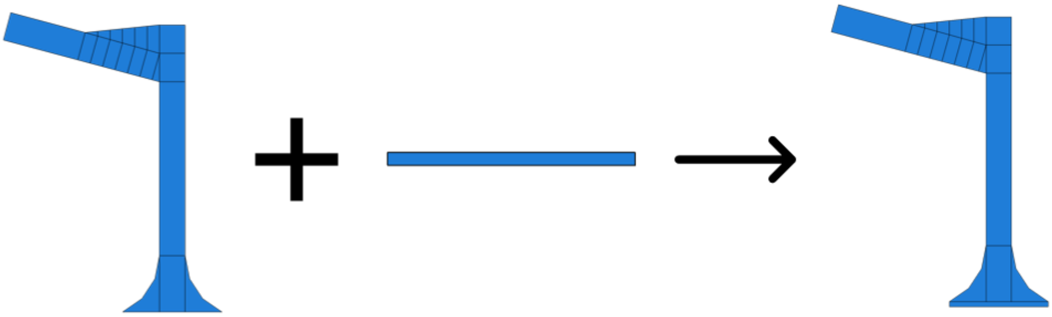

Figure 7.10: Division of the middle stringer into two parts

Given the need for a very fine mesh in the enriched region, having a uniform mesh across the panel is no longer computationally efficient. Hence, a fine mesh was defined close to the butt-joint filler of the middle stringer (the region of interest), while a coarse mesh was defined away from the filler. To transition from the coarse mesh to the fine mesh, the skin section was partitioned midway through the bay sections as shown in Figure 7.11. The region with Hex-dominated elements uses a sweep-type mesh technique and acts as a transition region between the fine and coarse mesh regions.

In contrast to the VCCT-based model, the skin and the outer stringers were defined as a single part for the XFEM-based model, as seen in Figure 7.11. This was done to maximise the computational efficiency of the model. If the stringers were modelled as individual parts and connected to the skin using a contact definition like it was done for the VCCT-based model, the contact detection and enforcement would add a penalty to the computational efficiency of the model. Continuum shell elements (SC8R) were assigned in the laminated sections, while 3D Stress Elements with reduced integration (C3D6R) were assigned in the filler sections.

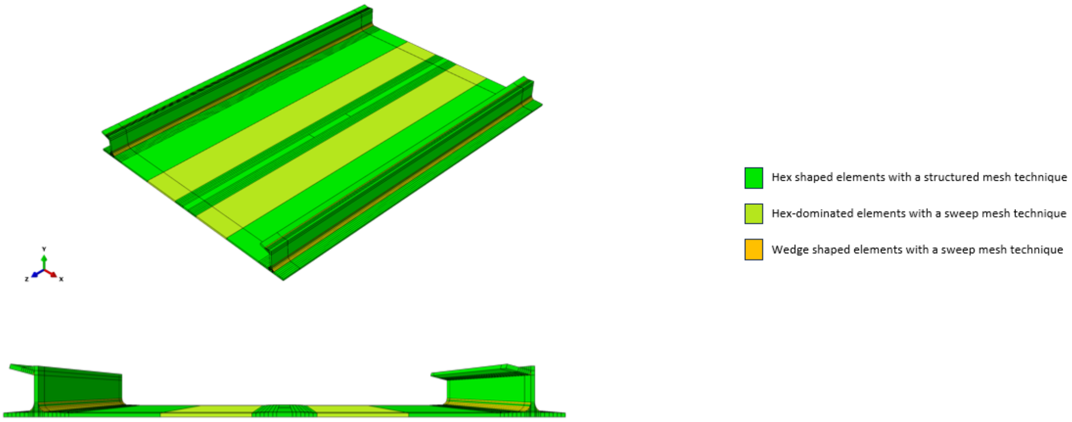

Figure 7.11: Mesh controls assigned to the skin and the outer stringers

The mesh controls for the middle stringer were defined similarly to the VCCT-based model, except in the fillet region. In this region, Hex-shaped elements were assigned using a sweep-type mesh technique. The purpose was to assign a fine mesh in the region. Like the outer stringers, Continuum shell elements (SC8R) were assigned in the laminated sections, while 3D Stress Elements with reduced integration (C3D6R) were assigned in the filler sections. Lastly, 3D Stress Elements (C3D6) were assigned for the interface section.

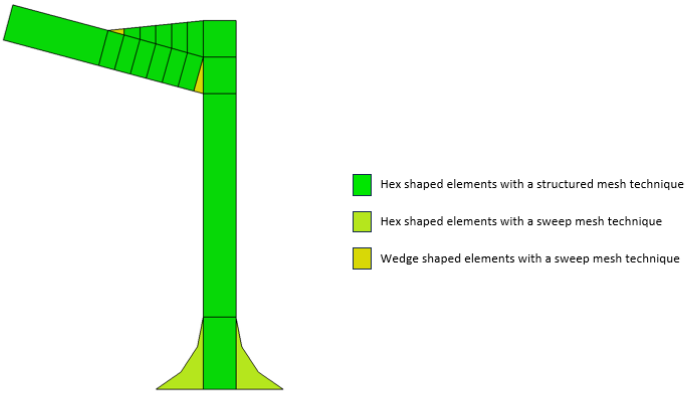

Figure 7.12: Mesh controls assigned to the middle stringer

To model the damage using XFEM, a damage initiation criterion and a damage evolution law must be defined. The damage initiation criterion is used to evaluate the initiation of degradation of the enriched element. The process is initiated when the stresses in the enriched element satisfy the damage initiation criterion specified for the model. For this study, the damage predicted using two different damage initiation criteria was evaluated: the Quadratic nominal stress criterion (QUADS) and the Maximum Principal Stress Criterion (MAXPS). The two criteria offer unique ways to evaluate damage initiation. The QUADS stress criterion assumes the initiation of a crack in the enriched element when the quadratic interaction function involving the nominal stress ratios (Equation 2.8) reaches one. Here, t_n^0, t_s^0, and t_t^0 represent the critical values of the nominal traction stress components whereas, t_n, t_s, and t_t represent the normal (along the local 3-direction) and the two shear tractions. The QUADS criterion is defined in conjunction with the NORMAL DIRECTION parameter. The NORMAL DIRECTION parameter has to be set to 1 or 2 to specify whether the new crack is defined orthogonal to the element local 1-direction or local 2-direction, respectively.

$$\left\{\frac{t_n{}^2}{t_n^0}\right\}+\left\{\frac{t_s{}^2}{t_s^0}\right\}+\left\{\frac{t_t{}^2}{t_t^0}\right\}=1 \tag{7.2}$$

The initiation of damage is evaluated differently in the case of the MAXPS criterion. Unlike the QUADS criterion, the MAXPS criterion evaluates the normal stresses acting onto three mutually perpendicular principal planes with zero shear stresses. If the normal stress acting on either of the three principal planes reaches a critical value, a crack is initiated normal to the corresponding principal stress component. Unlike the QUADS criterion, where the normal direction parameter defines the direction of crack propagation, the MAXPS criterion provides the freedom to determine the crack direction based on the local stresses in the enriched region. The drawback, however, is that the MAXPS criterion is suited for homogeneous, isotropic linear elastic materials. Therefore, the enriched region must be approximated as an isotropic linear elastic, homogeneous material. For this study, the position parameter corresponding to the MAXPS damage initiation criterion was set to NONLOCAL. This means that the stress/strain extrapolated to the crack tip is used to evaluate the damage initiation criterion and to determine the crack propagation direction.

QUADS				**MAXPS**
Nominal Stress Normal-only Mode	**Nominal Shear Stress First Direction**	**Nominal Shear Stress Second Direction**	**NORMAL DIRECTION**	**Critical Stress**
87 MPa	60 MPa	60 MPa	2	87 MPa

Table 7.6: Critical Stress Values for QUADS and MAXPS Criteria

The critical stress values for QUADS and MAXPS criteria are shown in Table 7.6. In their research, Dooren et al. used VCCT to model delamination and did not provide these values. Therefore, the stress values in Table 7.6 were obtained from Tijs et al.'s characterisation study [55]. It should be noted that while the material used in their study (PEKK-FC) is not identical, it is similar to the short fibre-reinforced PEKK filler used in the interface region. Finally, a damage initiation tolerance of 0.1 was chosen based on the experience from the DCB study.

After defining the damage initiation criterion, the damage evolution law is then defined to describe the degradation of material stiffness once the damage is initiated. Considering the complexity of damage in the skin-stringer interface region, an energy-based mixed-mode damage evolution law was defined using the BK criterion. The BK parameter (η) and fracture energies corresponding to modes 1, 2 and 3 used to define the BK criterion are given in Table 7.2. Further, a linear softening behaviour was selected, assuming that the PEKK SFRP material exhibits linear-elastic behaviour. Lastly, based on observations made during the DCB study, a viscous stabilisation factor of 1E-05 was chosen.

A Dynamic, Implicit-Quasi-static loading step was initiated, similar to the VCCT-based model. The initial and maximum increment sizes were set to 0.01 seconds, with a minimum increment size of 1E-15. To facilitate convergence, the general solver controls for the loading step were adjusted by increasing the maximum number of cut-backs allowed for an increment (represented by the parameter I_A) from 5, the default value, to 15. The field output request was modified to include additional output identifiers related to the XFEM crack. These identifiers are: PHILSM, which is a signed distance function used to describe the crack surface; STATUSXFEM, which indicates the status of the enriched element (1.0 if the element is completely cracked, 0.0 if the element contains no crack, and a value between 1.0 and 0.0 if the element is partially cracked); and LOADSXFEM, which represents the distributed pressure loads applied to the crack surface.

In this section, the modifications made to the original VCCT-based model to model the damage at the skin stringer interface using XFEM were discussed in detail. Like the VCCT-based model, the fibre and matrix failure in the composite sections was evaluated during the loading process using the Hashin criterion. The boundary conditions and displacement-controlled load definition were the same as the VCCT-based panel model. To introduce imperfections in the form of liner perturbations, different percentages of mode 1 out-of-plane deformations were considered for the VCCT-based model. Based on the predicted post-buckling behaviour, the appropriate imperfection was selected, and the same level of imperfection was introduced to the XFEM-based model of the stiffened panel. The predicted skin-stringer separation and post-buckling behaviour using the XFEM-based model are reported in chapter 8.

8

Chapter 8: Quasi-Static Analysis Results

The results obtained from the stiffened panel models as detailed in chapter 7 are reported in this chapter. To begin with, the VCCT-based model was used to pick a suitable magnitude of mode 1 out-of-plane deformations to be introduced to the panel as imperfections. This was done by introducing 0 to 10% of mode 1 buckling deformations to the model as linear perturbations and then evaluating the post-buckling behaviour of the panel. For evaluation, the results reported by Dooren et al. were considered a benchmark because they were experimentally obtained [50]. After choosing a suitable magnitude of mode 1 imperfection, the panel was modelled using XFEM.

8.1. Post-Buckling Behaviour Exhibited by Test Panels

Dooren et al. tested two panels until the final failure. The examination of test panel 1 revealed an initial buckling mode of three half waves, which was anti-symmetric relative to the central stringer. As the load increased, the buckling pattern underwent a mode change, with a fourth-half wave forming at the upper part of the right bay. The inward out-of-plane displacement towards the stringers was observed to be greater than the outward displacement. Following the initial buckling, the out-of-plane displacement magnitude was found to be nearly identical in both bays. However, as the load increased, the fourth half-wave became more prominent, and the displacement magnitude in the left bay increased in both directions compared to the right bay. The half-waves in the left bay were also found to be longer than those in the right bay. This discrepancy became more evident with the appearance of the fourth half-wave in the right bay and continued to grow until the final failure. The test panel 2 exhibited the same three-half wave buckling pattern as test panel 1. Compared to test panel 1, the buckling pattern of panel 2 changed with a fourth half-wave appearing at the top of the right bay at a higher load, and this fourth half-wave was smaller in size. The out-of-plane displacement of test panel 2 at 116 kN was greater in the inward direction and lesser in the outward direction than test panel 1. This variation could be attributed to differences in geometric or loading imperfections, and it diminished at higher loads when the out-of-plane displacements of panels 1 and 2 started to converge. Figure 8.1 displays the out-of-plane displacement contours for test panels 1 and 2 at different loads. It is important to note that the displacement contours presented here were obtained from the rear side of the panel using a 3D DIC setup.

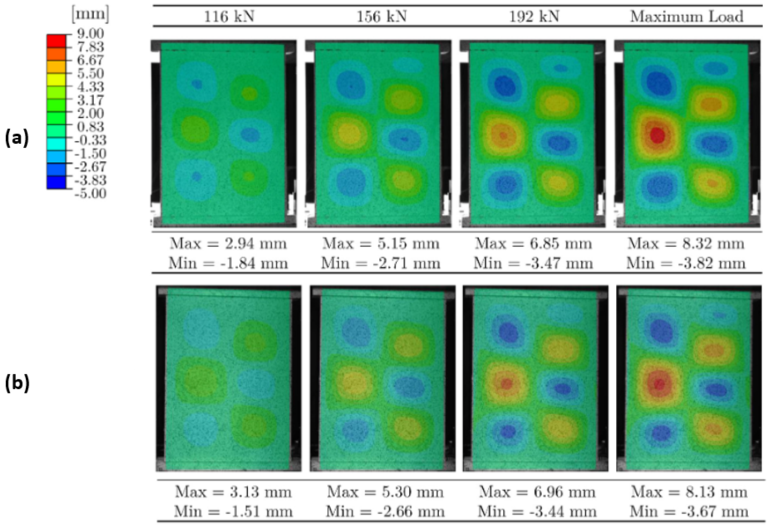

Figure 8.1: Out-of-plane displacements corresponding to (a) Test Panel 1; (b) Test Panel 2, at different loading intervals [50]

Regarding the skin-stringer separation behaviour, crack growth was initiated at 120 kN and 119 kN for test panels 1 and 2, respectively. Unstable growth followed the crack growth initiation, which was later followed by stable crack growth. At 156 kN, both panels exhibited significant crack opening, with more growth in the downward direction than the upward direction. Furthermore, the crack opening was found to be one-sided due to the buckling shape. The outward half-wave on the cap side opens the crack, while the inward half-wave on the opposite side of the cap tends to close the crack. Upon analysing the fracture surface, the authors found that around 196.5 mm of the stringer surface was separated before failure. Delamination of the plies from the skin was observed on the left side, with only a small amount of filler material still attached to the skin. No delamination of plies was observed on the right side. However, more filler material remained attached to the skin. The authors hypothesise that this difference in the fracture surface could be due to the one-sided crack growth behaviour.

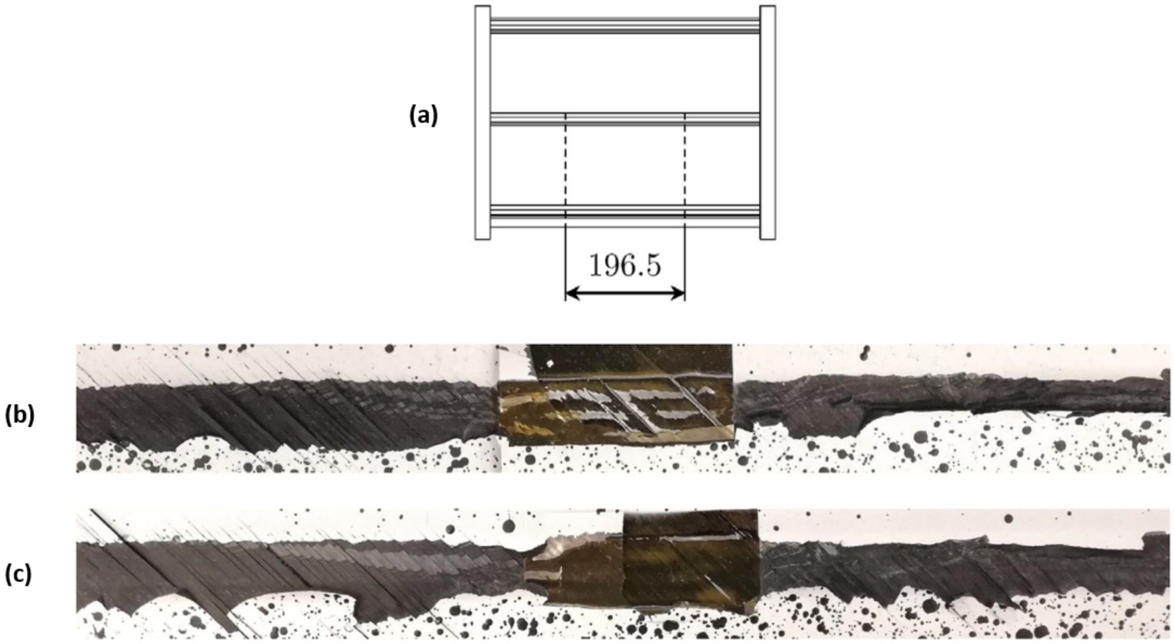

Figure 8.2: Top view of skin-stringer interface: (a) Area of Interest; (b) Test Panel 1 - fracture surface; (c) Test Panel 2 - fracture surface

8.2. Quasi-Static Analysis Results: VCCT Criterion

The results of the quasi-static analysis using the VCCT Criterion are reported in the following sub-sections. Subsection 8.2.1 details the effect of imperfections on the post-buckling behaviour. Using the load-displacement curves, a model with a suitable imperfection magnitude is chosen for further evaluation. Subsection 8.2.2 then details the out-of-plane displacements predicted by the chosen model. This is followed by an assessment of the skin-stringer separation behaviour predicted by the VCCT criterion in subsection 8.2.3. Lastly, the composite sections were evaluated for Hashin failure criterion in subsection 8.2.4.

8.2.1. Imperfection Study

Dooren et al. report that test panels 1 and 2 were found to buckle at 94 KN load. A linear stiffness of 132 kN/mm was reported for both panels. The final failure loads of 223 kN and 215.9 kN were reported for test panels 1 and 2, respectively. Taking these reported values as a benchmark, the buckling load, final failure load and linear stiffness predicted by the finite element models were assessed. The predicted values are presented in Table 8.1. Further, the load-displacement curves obtained for test panels 1 and 2 and the predictions made using finite element models with different imperfections are shown in Figure 8.3.

Model Description	Buckling Load [kN]	Final Failure Load [kN]	Linear Stiffness [kN/mm]	CPU Time [s]
Test Panel 1	94.00	223.00	132.00	-
Test Panel 2	94.00	215.90	132.00	-
FE (Pristine Panel)	96.21	225.98	133.63	152313
FE (2.5% Imperfection)	94.66	226.57	133.21	172553
FE (5% Imperfection)	92.82	230.49	132.92	185177
FE (7.5% Imperfection)	90.99	230.20	132.50	167846
FE (10% Imperfection)	90.96	238.12	131.83	61186

Table 8.1: The buckling load, final failure load, linear stiffness and CPU Times corresponding to the finite element models

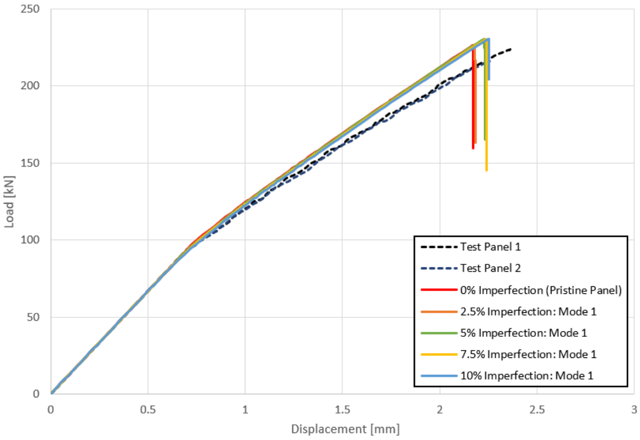

Figure 8.3: Load-Displacement curves from tests and finite element models

According to the data presented in Table 8.1, the buckling load decreases as the magnitude of imperfection increases. The models with 0% and 2.5% imperfections overestimate the buckling load, whereas the models with 5% to 10% imperfections underestimate it. Among all the models, the one with 10% imperfection has the highest error at -3.23%, whereas the model with 2.5% imperfection shows the closest prediction with only 0.7% error.

Similarly, the linear stiffness predicted by the finite element models decreases with an increasing imperfection magnitude. Except for the model with 10% imperfection, which underestimates the stiffness by 0.13% (closest prediction), all the other models overestimate the linear stiffness. The model with no imperfections has a maximum error of 1.23%.

The final failure load for test panels 1 and 2 differed slightly from each other, but not significantly. This difference could be attributed to imperfections in the panel's geometry and inconsistencies during loading. The finite element models overestimated the final failure load. The models with 0% and 2.5% imperfections provided the closest predictions.

Lastly, all the finite element models overestimate the stiffness of the panel in the post-buckling field. A loss of stiffness of the panel is expected as the crack grows in the skin-stringer interface. The loss in stiffness exhibited by the finite element models is lower than the test specimens. This discrepancy could be because the skin-stringer separation was not considered for the outer stingers. The separation of the webs and the caps was also not modelled. Additionally, the finite element models did not consider delamination in the composite laminate sections, which could add to the loss in stiffness in the post-buckling field.

An analysis of the buckling load, linear stiffness, and final failure load of various finite element models determined that the model with a 2.5% imperfection provides the closest prediction of the post-buckling behaviour. The buckling load and linear stiffness of this model are overestimated by 0.7% and 0.91%, respectively, while the final failure load is overestimated by 1.6% and 4.94% when compared to test panels 1 and 2, respectively. Compared to the remaining models, the model with 2.5% mode 1 imperfection was chosen as the most suitable candidate for further comparison.

8.2.2. Out-of-plane Displacement

The out-of-plane displacement contours were captured at four different load levels: 116 kN, 156 kN, 192 kN, and the maximum load of 226.57 kN for the model with a 2.5% mode 1 imperfection. These contours were then compared with the ones obtained from test panels 1 and 2 as shown in Figure 8.4. The out-of-plane displacement contours illustrate the evolution of the deformations in the post-buckling field, with the maximum and minimum displacements reported for each load level. A positive sign indicates displacement in the inward direction, towards the stringer, while a negative sign indicates displacement in the outward direction, away from the stringer.

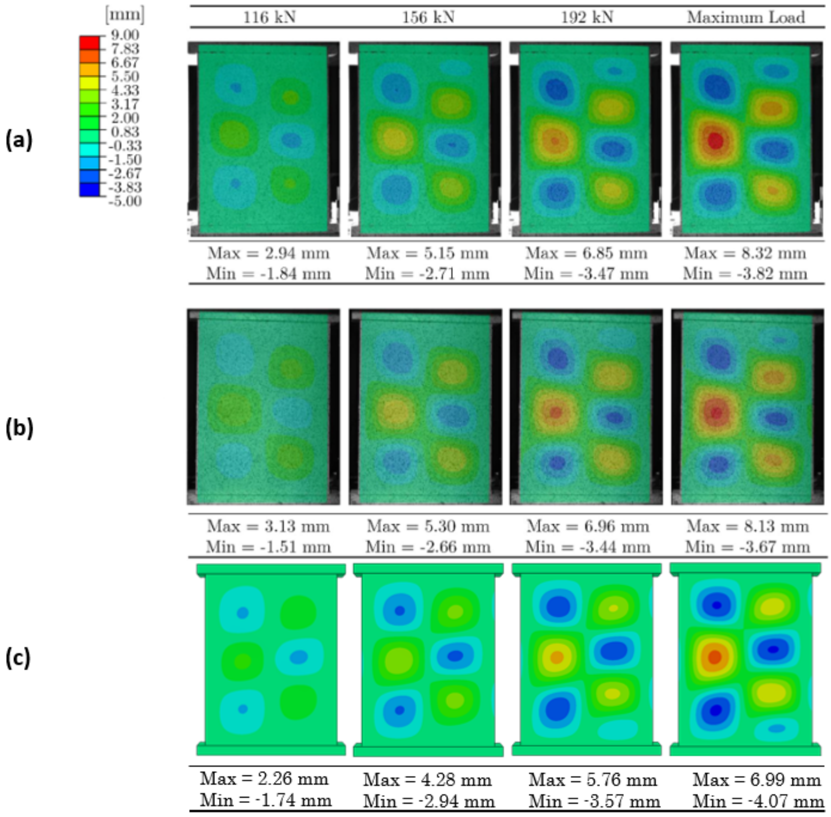

Figure 8.4: Out-of-plane displacement: (a) Test Panel 1; (b) Test Panel 2 and (c) FE Model (2.5% Imperfection)

The finite element model accurately predicted the panel's initial buckling shape with three half-waves. The model also predicted the position and length of the half-waves well. The model's prediction of the magnitude of out-of-plane displacement at 116 kN and 156 kN load levels was closer to test panel 1. At 192 kN load level, the model successfully captured the formation of the fourth smaller half-wave in the outward direction. However, the position of the fourth half-wave is different compared to the test panels. While the shape of the half-wave is predicted well, the model predicts the wave to form at the bottom of the right bay rather than on the top. This could be due to the geometric imperfections present in the model. The predicted out-of-plane displacements are generally smaller in the inward direction than the test panels, while the predicted outwards out-of-plane displacements are larger. This difference in the magnitude of out-of-plane deformations could affect the amount of crack opening in the panel and thus influence the final failure load. Lastly, like the test panels, the length of the half-waves in the left bay is longer compared to the right bay.

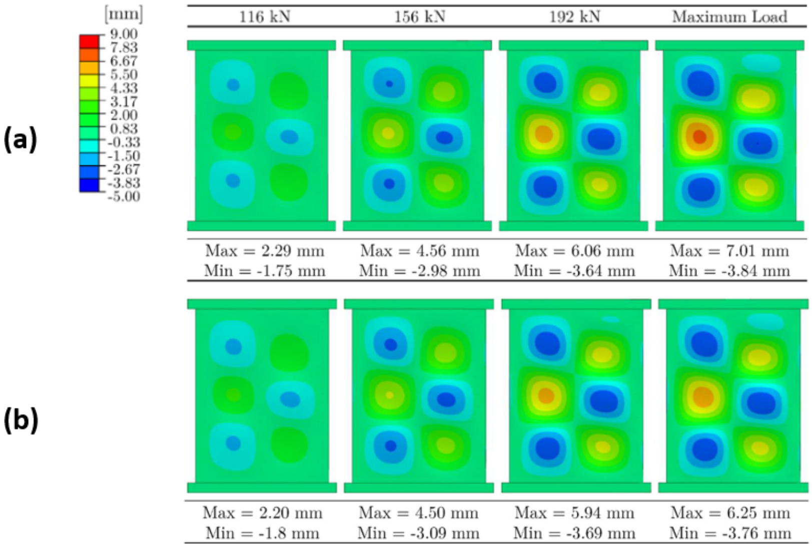

Figure 8.5: Out-of-plane displacement: (a) FE Panel 1; (b) FE Panel 2; obtained by Dooren e al. with actual geometric imperfections [50]

The prediction error in the magnitude of displacements could be minimised by considering the actual geometric imperfections in the test panels, and this hypothesis is supported by the finite element simulations reported by Dooren et al. [50]. The out-of-plane displacement contours obtained by the authors using the finite element models are shown in Figure 8.5. These models used the data captured using 3D DIC to introduce imperfections. From Figure 8.5, it can be observed that although the finite element models provided closer prediction, they could not capture the exact magnitude of out-of-plane deformations. Given the lack of availability of the geometric imperfections from the test panels, the out-of-plane deformations predicted by the finite element model with 2.5% mode 1 imperfections can be considered acceptable.

8.2.3. Skin-Stringer Separation

According to Dooren et al., the crack length before the final failure was 196.5 mm. The finite element model with a 2.5% imperfection was used to predict the evolution of the crack length, which was then plotted along with the load-displacement curve as shown in Figure 8.7. The numerical model predicted that the crack length at the final failure load would be around 178 mm, which is less than what was observed in the test panels. The under-prediction of crack growth could be the reason why the finite element model overestimates the final failure load. This is because, with less skin-stringer separation, the panel has more load-bearing capacity. Moreover, the crack length evolution curve obtained from the numerical model showed a stable crack growth behaviour after initiation, which is different from the unstable crack growth behaviour reported by Dooren et al. in their study [50].

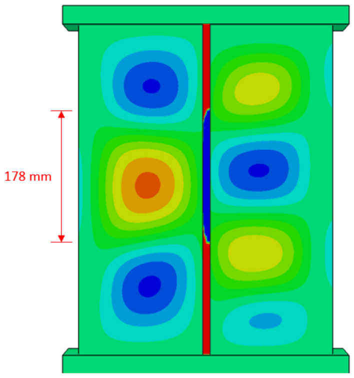

Figure 8.6: The predicted skin-stringer separation and the out-of-plane deformations in the stiffened panel at the maximum load

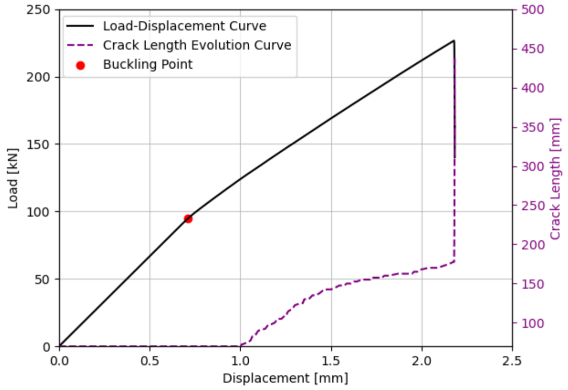

Figure 8.7: Crack length curve with respect to displacement for the finite element model

The evolution of delamination along the skin-stringer interface was assessed by capturing the bond state contours at four different load levels: 116 kN, 156 kN, 192 kN, and Maximum Load (226.57 kN), as shown in Figure 8.8. The intact interface is indicated by red, while the separated interface is indicated by blue in the contours. The numerical model predicts that the crack growth initiation will occur at 116 kN, which is close to the crack growth initiation load observed for test panels 1 and 2, although it is slightly underestimated. Beyond this point, the numerical model predicts stable crack growth. At 156 kN load, significant crack growth is observed. The crack growth is one-sided due to the presence of an outwards half-wave, which promotes crack opening on the cap-side of the panel, similar to the test panels. Furthermore, the crack front shape is quasi-elliptical, with a narrow horizontal line of the intact interface. At 192 kN, the quasi-elliptical shape of the crack front remains dominant, and the crack front has elongated predominantly along the left side, upwards of the panel. This could be driven by the formation of an outward half-wave on the lower part of the right bay, which pushes the predominant outward half-wave upwards. As the magnitude of the fourth half-wave increases upon further loading, the crack front extends along the left side, as evident from Figure 8.8 (d). Upon further compression past the final failure load, the model predicts the occurrence of unstable crack growth. This happens due to the formation of a tunnel beneath the middle stringer, caused by the connection of the outwards half waves at the top of the left and right bay.

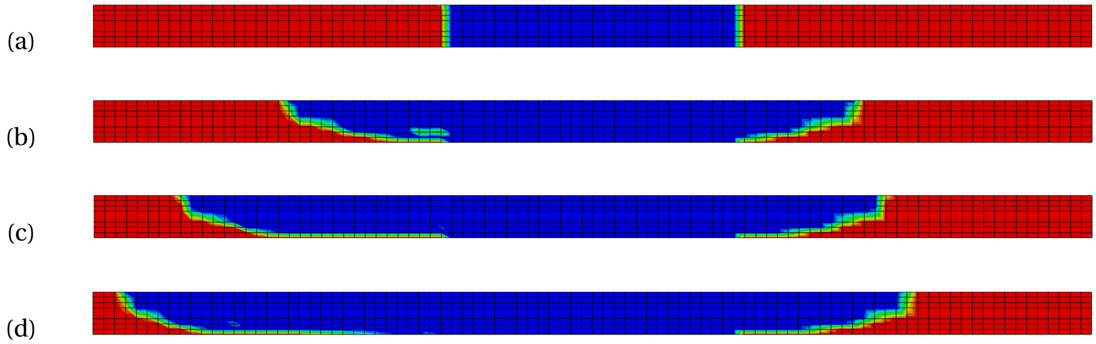

Figure 8.8: Evolution of delamination along the skin-stringer interface : (a) 116 kN; (b) 156 kN; (c) 192 kN and (d) Maximum Load

8.2.4. Hashin Failure Criterion

The panel's composite sections were evaluated for Hashin failure criterion at the final failure load. The numerical model primarily predicts failure in the panel's skin sections. Therefore, the contours of Hashin fibre and matrix failure were captured at the final failure load and presented in Figure 8.9, Figure 8.10, Figure 8.11 and Figure 8.12. It must be noted that these contours were captured from the front side of the panel. It is evident that only fibre compression failure is present in the panel at the final failure load. Further, the fibre compression failure is confined to the skin section in contact with the middle stringer, where the skin-stringer separation is modelled.

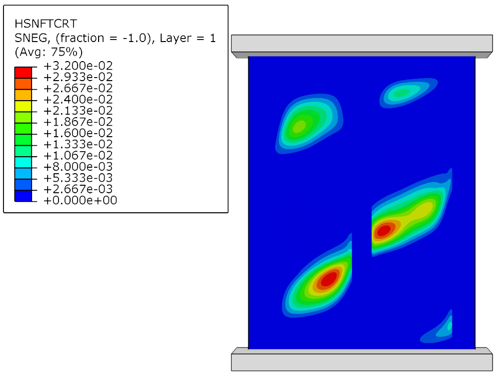

Figure 8.9: Hashin fibre tension criterion contour at the final failure load

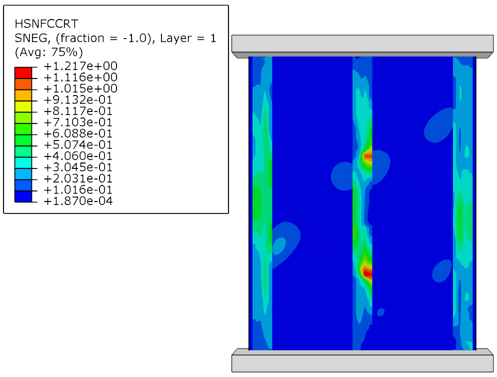

Figure 8.10: Hashin fibre compression criterion contour at the final failure load

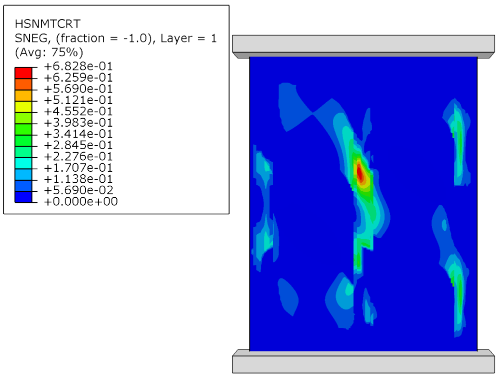

Figure 8.11: Hashin matrix tension criterion contour at the final failure load

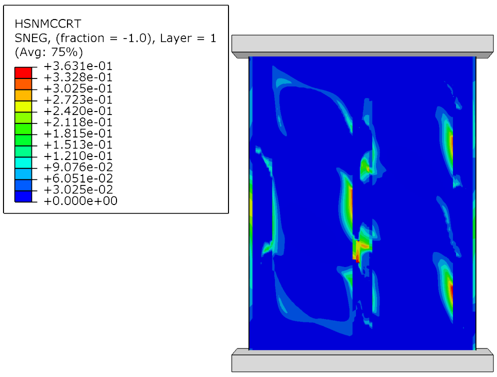

Figure 8.12: Hashin matrix compression criterion contour at the final failure load

8.2.5. Conclusion

It can be concluded from the analysis of several subsections, namely subsection 8.2.1, subsection 8.2.2, subsection 8.2.3 and subsection 8.2.4, that a finite element model with 2.5% of out-of-plane mode 1 displacement can provide a fairly accurate prediction of the post-buckling behaviour of test panels. The model can precisely capture the initial buckling shape with three half waves in each bay. Although the model could predict the formation of the fourth half-wave, the position of the half-wave was not the same as the test panels. The model underestimates the crack extension at the skin-stringer interface, which leads to over-prediction of the final failure load. Despite this, the finite element model can replicate the elliptical shape of the crack front, although it does not capture the delamination of the plies in the skin under the middle stringer. Despite the lack of geometric imperfections for this study, the model offers a fairly accurate prediction for the buckling load and final failure load. These load levels are crucial while designing skin-stringer structures. Therefore, using 2.5% mode 1 imperfections is justified and will be used for evaluating the crack growth at the skin-stringer interface through the extended finite element method.

8.3. Quasi-Static Analysis Results: XFEM (QUADS Criterion)

8.3.1. Mesh Convergence Study

A mesh convergence study was conducted to evaluate the predicted post-buckling behaviour of the stiffened panel. Four different mesh configurations were assessed based on the resultant load-displacement curves. The skin section's element size was varied, with a fine mesh close to the middle stringer where skin-stringer separation is expected and a coarse mesh away from it. The skin section was partitioned, and hex-dominated elements were used to define the transition region using the sweep mesh technique (as illustrated in Figure 7.11). The seeds assigned to the skin sections are shown in Table 8.2 using the terminology defined through Figure 8.13. It should be noted that only half of the panel is shown in Figure 8.13, through the line of symmetry passing through the middle stringer. The outer stringers were assigned a mesh size corresponding to the value x in Table 8.2, while a uniform mesh size of 2.5 mm was assigned to the middle stringer.

In the table Table 8.2, mesh assigned to the butt-joint fillet and the interface section connecting the middle stringer to the skin are given. In this case, the element size was determined based on the cohesive zone length ahead of the crack tip, which was discussed in section 7.4. It was found that the maximum element length in the enriched region should be limited to 0.787 mm to ensure at least three elements in the cohesive zone. For this reason, element lengths of 0.7 mm, 0.6 mm, and 0.5 mm were selected for study. A choice was made to use a fine mesh for the butt-joint fillet and interface, while a relatively coarser mesh of 2.5 mm was used for the middle stringer and nearby skin sections. This was done to ensure the model's computational efficiency and maintain a suitable aspect ratio for the continuum shell element. In this case, the nodes on the connecting surfaces do not match. This is addressed in Abaqus by connecting the nodes on the fine mesh surface (secondary surface) to the nearest node on the coarse mesh surface (primary surface). The displacement and other parameters are then estimated by interpolating the values from the primary surface to the secondary surface [40].

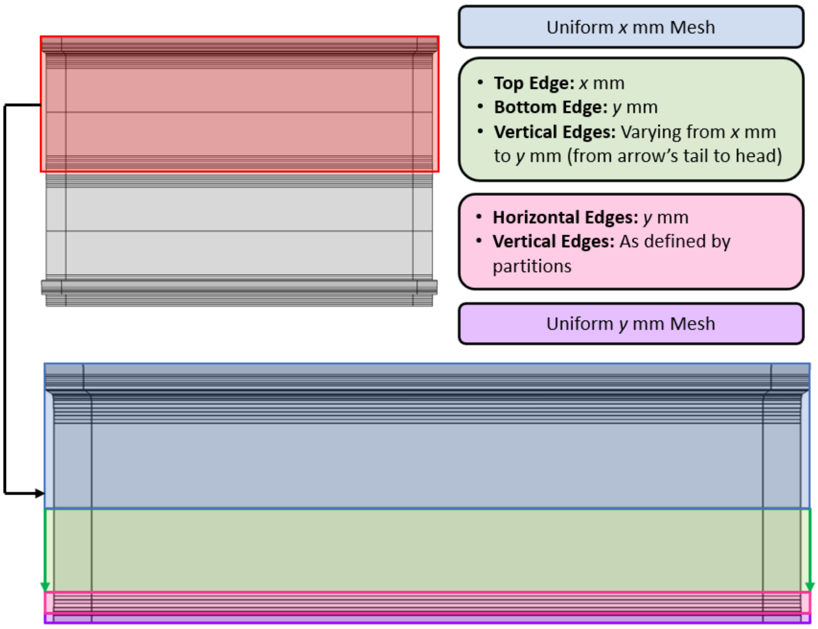

Figure 8.13: Illustration of the terminology used for mesh assignment

Mesh Configuration	x [mm]	y [mm]	Butt-Joint Fillet & Interface Section [mm]
1	5	2.5	0.7
2	5	2.5	0.6
3	5	2.5	0.5
4	2.5	2.5	0.5

Table 8.2: Mesh size definitions

Load-displacement curves were obtained for different mesh configurations and compared to the test panels and the converged solution obtained using the VCCT-based model. The curves are shown in the Figure 8.14. Based on these curves, the linear stiffness, buckling load, and peak load were predicted for each model and presented in the Table 8.3. Lastly, the total CPU time utilised to run these models was also obtained and presented in Table 8.3.

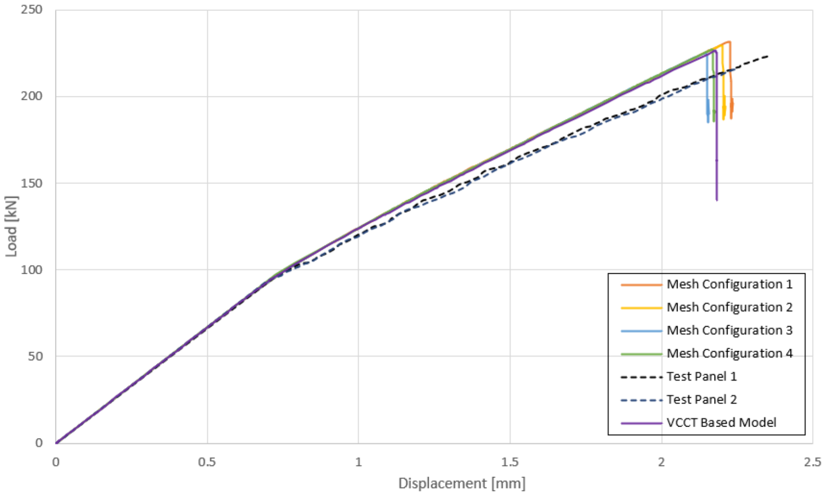

Figure 8.14: Load-Displacement curves from tests and finite element models

Model Description	Buckling Load [kN]	Final Failure Load [kN]	Linear Stiffness [kN/mm]	CPU Time [s]
Test Panel 1	94.00	223.00	132.00	-
Test Panel 2	94.00	215.90	132.00	-
FE (VCCT Based Model)	94.66	226.57	133.21	172553
FE (Mesh Configuration 1)	95.86	231.64	133.13	174872
FE (Mesh Configuration 2)	95.86	229.5	133.13	188218
FE (Mesh Configuration 3)	95.86	225.239	133.13	174785
FE (Mesh Configuration 4)	97.19	226.89	133.60	222358

Table 8.3: The buckling load, final failure load, linear stiffness and CPU Times corresponding to the finite element models

As per the data presented in Table 8.3, it can be observed that the XFEM-based models predict higher buckling loads compared to both the test panels and the VCCT-based model. The buckling loads predicted by mesh configurations 1, 2, and 3 are the same, with only a 1.98% error compared to the test panels. This can be explained as the mesh configuration of the skin and the stringer sections remains the same for these models. However, the buckling load predicted for the model with mesh configuration 4 is higher than the others, with a 3.39% error compared to the test panels.

The XFEM-based models predict a stiffness very similar to the VCCT-based models. However, in general, the XFEM-based models tend to overestimate the linear stiffness of the panel. The models with mesh configurations 1, 2 and 3 predict a linear stiffness of 133.13 kN/mm, which has only 0.86% error compared to the test panels. The linear stiffness of the models remains unchanged due to the same reason mentioned for the buckling load prediction. On the other hand, the model with mesh configuration 4 predicts a linear stiffness of 133.60 kN/mm, which has 1.21% error as compared to the test panels.

Unlike the buckling load and linear stiffness predictions, the final failure loads predicted by the XFEM-based models differ from each other. This can be linked to the change in the mesh assigned to the skin-stringer interface, where the separation behaviour is modelled during the post-buckling field. In general, as the mesh is refined, the predicted linear buckling load becomes lower, although the variation between the models is not too significant. The predicted peak load by the coarse mesh model (mesh configuration 1) and the fine mesh model (mesh configuration 4) only changes by 2.05%. Generally, the fine mesh model with mesh configuration 4 predicts the final failure load very close to the VCCT-based model. The VCCT-based and XFEM-based models over-predict the final failure load by a similar error margin. Furthermore, as evident from Figure 8.14, both the XFEM-based models and the VCCT-based model under-estimate the loss in stiffness in the post-buckling field, thereby predicting a higher stiffness in the nonlinear region when compared to the test panels. This could be attributed to the idealisation of the test panel for the purposes of modelling.

Lastly, the total CPU times required for the XFEM-based models are higher as compared to the VCCT-based model. This suggests that XFEM has higher computational requirements. When comparing the XFEM-based model with mesh configuration 4 and the VCCT-based model, there is a 28.86% increase in CPU time. Comparing these two models offers a fair comparison of the increase in the required CPU time by XFEM because the mesh assigned to the skin, stringer, and potting sections for these two models is the same. The only difference is the use of a finer mesh in the interface between the middle stringer and the skin.

Judging by the predicted buckling loads, final failure load and linear stiffness, the models with mesh configurations 3 and 4 come very close to the VCCT based model and the obtained test results. But before choosing the converged solution, the skin-stringer separation predicted by these models was evaluated. This is because the mesh convergence study primarily focused on varying the mesh in the interface section. The next section compares the skin-stringer separation behaviour predicted by these models with the results obtained from the VCCT-based model.

8.3.2. Skin-Stringer Separation

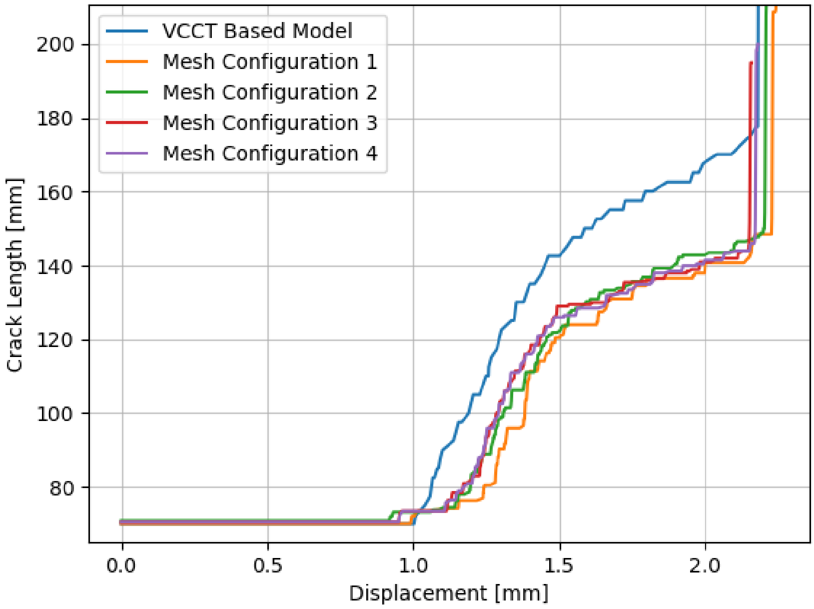

Figure 8.15: Crack length evolution curves from the XFEM (QUADS Criterion) and VCCT based finite element models

A comparison of the crack length evolution predicted by the XFEM (QUADS Criterion) based models and the VCCT-based model is shown in Figure 8.15. Figure 8.15 indicates that the predicted crack length evolution curves by the XFEM (QUADS Criterion) based models are quite similar to each other, with minor deviations. These deviations could be due to changes in the skin and stringer's mesh configuration or numerical instabilities during the analysis. However, compared to the VCCT-based model, it is apparent that the XFEM (QUADS Criterion) based model under-predicts the extent of skin-stringer separation in the post-buckling field. Furthermore, the crack length at the final failure load is lower than that observed in the test panels. Based on the models with a 0.5 mm element size in the interface section, it was predicted that the crack length would be 144.5mm (with mesh configuration 3) and 146.5 mm (with mesh configuration 4) at the final failure loads. These predicted crack lengths are 26.4% and 25.6% lower than the actual crack length of 196.5 mm that was observed in the test panels. This discrepancy could be attributed to one of the following hypotheses:

Hypothesis 1

Both the VCCT and XFEM (QUADS Criterion) approaches model the skin-stringer separation behaviour differently. VCCT approach models the separation of the skin and the stringer along the 2D interface between the skin and the butt-joint filler. On the other hand, the XFEM (QUADS Criterion) approach models the separation of the skin and the stringer as a 3D crack within the solid interface section. While these models yield different crack lengths (distance between the farthest nodes in the damaged elements), the net fracture area of the resultant fracture surfaces may be the same. However, due to the lack of information required to calculate the fracture surface area predicted by the XFEM (QUADS criterion) model, this theory cannot be verified for this thesis study.

Hypothesis 2

It is possible that the difference in the predicted crack length may be due to the nominal stress values used to model crack initiation not accurately representing the strength of the SFRP butt joint filler. There is a lack of experimental data for the SFRP PEKK filler material, which led to the nominal stress values being assumed based on a study by Tijs et al. [55]. This study pertained to material without short fibre reinforcements. However, the PEKK filler reinforced with short fibres should be stronger than the PEKK-FC material Tijs et al. considered. Using experimentally obtained values could provide a better correlation, but an experimental investigation is not within the scope of this study.

Although all models have certain limitations, in this case, crack growth prediction, it is essential to review these models comprehensively before disregarding them. It is also important to highlight the constraints present in modelling the crack growth through the skin-stringer interface for the reasons mentioned earlier. Despite these limitations, the models have provided a good estimate of the final failure load of the test panels, which is a critical factor in structural analysis. Additionally, these models were as effective as the VCCT-based model in predicting the loss in stiffness during the post-buckling phase, as shown by the load-displacement curves. Therefore, these models were considered to be acceptable, and no further investigation was carried out to fix the discrepancy in the predicted crack length evolution.

The crack growth behaviour of mesh configurations 1 through 4 were found to be comparable, suggesting that the models have converged. Therefore, mesh configuration 3 will be utilised for further evaluation as it provides outcomes similar to mesh configuration 4 while requiring less computational cost. The next stage involved evaluating the crack shape by capturing the STATUSXFEM contour at four load levels: 116 kN, 156 kN, 192 kN, and Maximum Load (225.239 kN). These contours were captured from the viewpoint of the bottom of the middle stringer, as depicted in Figure Figure 8.16. This evaluation aims to study the shape of delamination and later compare it to the bond state contours obtained using VCCT. It should be noted that the red colour on the STATUSXFEM contour represents a region with a completely developed crack, while the blue regions indicate undamaged areas.

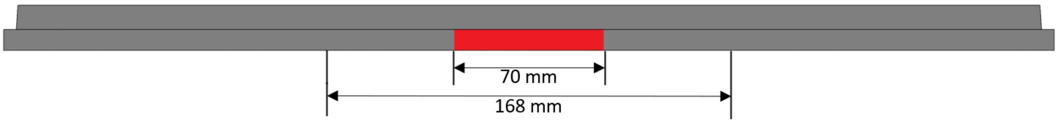

Figure 8.16: Reference for the view-point used to capture STATUSXFEM contours

Figure 8.17: Evolution of delamination along the skin-stringer interface : (a) 116 kN; (b) 156 kN; (c) 192 kN and (d) Maximum Load

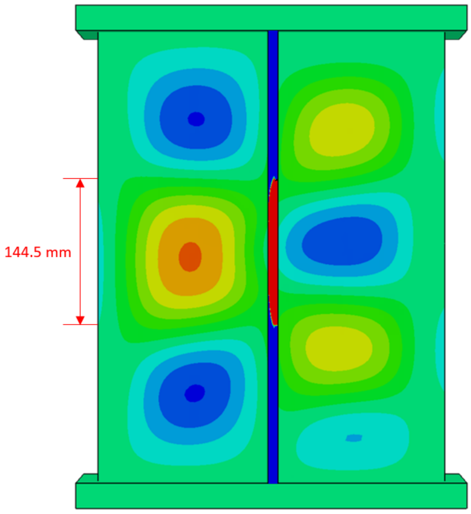

Figure 8.18: The predicted skin-stringer separation and the out-of-plane deformations in the stiffened panel at the maximum load

The STATUSXFEM contours were analysed in reference to the out-of-plane displacement contours shown in Figure 8.19. While a discussion on the predicted deformations is provided in the next section, they are referred to provide more context for the observed crack growth behaviour. To begin with, at 116 KN (Figure 8.17 (a)), once the panel has buckled, it appears that the damage initiation criterion has been met and the crack growth has been initiated. However, it can be seen that the stiffness of the crack elements is being degraded, and the elements are not fully damaged. At 156 kN (Figure 8.17 (b)), one-sided crack growth is predicted along the cap side of the interface. As observed with the VCCT-based model and the test panels, a semi-elliptical delamination front is observed with a portion of the interface still attached to the skin. As the panel is further loaded, the crack front extends further (Figure 8.17 (b)). Here, it can be seen that with the formation of the fourth half-wave, the crack front extended more in the left direction (upwards of the panel) than the right (downwards the panel). The delamination shape is still semi-elliptical. At the maximum load, it is seen that the crack front does not extend much further on the right side, but the crack front does extend further on the left side. Furthermore, the presence of black lines near the crack front on the left indicates the crack tip reaching the bottom surface of the interface section. Given that the implementation of XFEM (QUADS Criterion) in Abaqus does not allow for the branching of cracks or the initiation of new cracks close to an exiting the, the original crack front moves around the attached portion of the filler. This could be one of the reasons for the slowing down of the crack growth.

8.3.3. Out-of-plane Displacement

Like the VCCT-based model, the out-of-plane displacement contours obtained using the selected XFEM (QUADS Criterion) model were captured at four levels: 116 kN, 156 kN, 192 kN and the maximum load of

225.239 kN. The predicted contours were compared to those reported by Dooren et al. for test panels 1 and 2 in Figure 8.19. The maximum and minimum displacements corresponding to each load level are also indicated.

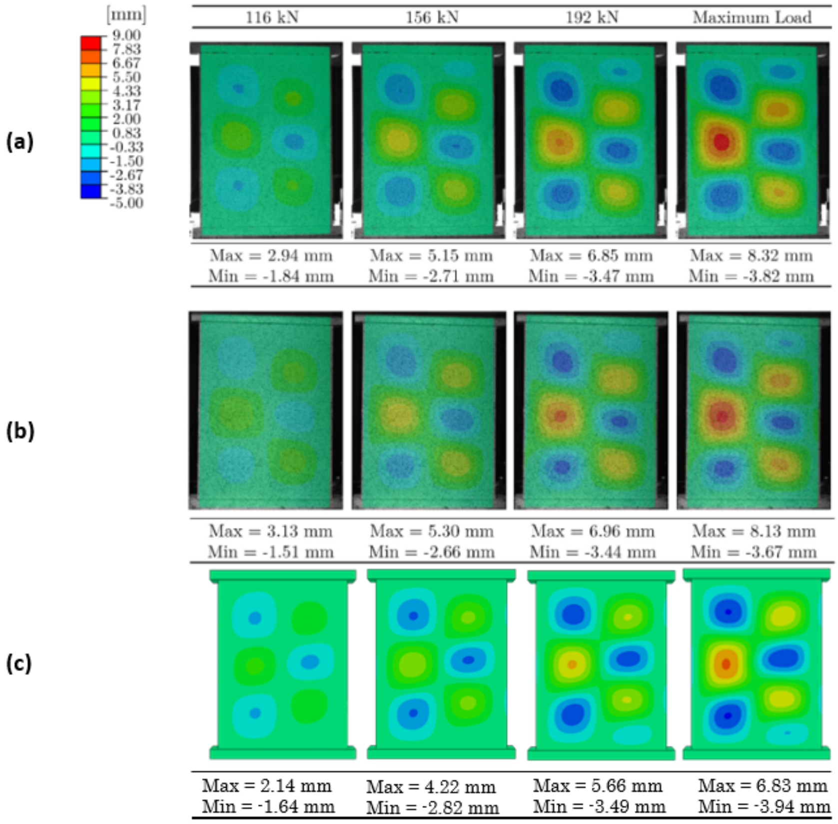

Figure 8.19: Out-of-plane displacement: (a) Test Panel 1; (b) Test Panel 2 and (c) FE Model (Mesh Configuration 3)

The finite element model accurately predicts the formation of three half-waves in each bay after buckling at 116 kN. However, it underestimates the inward (positive) deformations towards the stringer and overestimates the outward (negative) deformations away from the stringer. This is also true at 156 kN, but in both cases, the model can precisely predict the shape and position of the half-waves. As the panel is further loaded, the model can also predict the formation of the fourth outward half-wave in the right bay. However, like the VCCT model, the position of the fourth half-wave in this case differs from the test panels. This could be due to the same reasons as in the case of the VCCT-based model, which is the geometric imperfections introduced to the model. The model can replicate the longer length of the half-waves in the left bay compared to the ones in the right bay. At the maximum load, the inward deformations are underestimated, while the outward deformations are slightly overestimated. As discussed in subsection 8.2.2, it is possible to minimise the error in predicted deformations by incorporating the geometric imperfections from the test panels rather than assuming a fraction of mode 1 deformation as an imperfection. However, the predicted results are acceptable due to the unavailability of actual geometric imperfections, as they closely predict the post-buckling behaviour.

8.3.4. Hashin Failure Criterion

The composite sections within the panel were evaluated for the Hashin fibre and matrix failure criterion. The contours were captured at the final failure load (refer to Figure 8.20, Figure 8.21, Figure 8.22 and Figure 8.23). It must be noted that these contours were captured from the front side of the panel. Like the VCCT model, the failure was found to occur in the skin sections of the panel. Moreover, the failure was confined to the regions near the middle stringer within the skin sections. From the contours, it can be seen that only the Fiber Compression failure occurred in the stiffened panel, and the failure was present at the skin-stringer interface. This is expected since the loads on the panel were compressive.

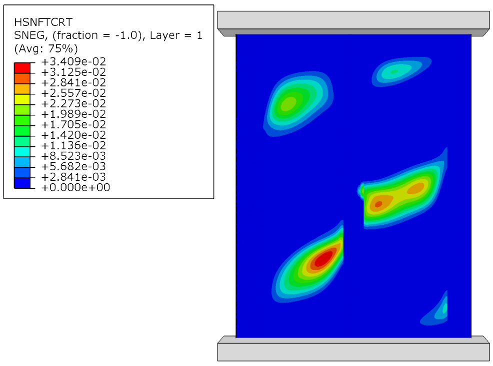

Figure 8.20: Hashin fibre tension criterion contour at the final failure load

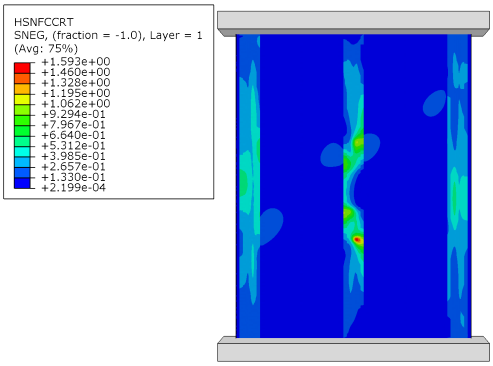

Figure 8.21: Hashin fibre compression criterion contour at the final failure load

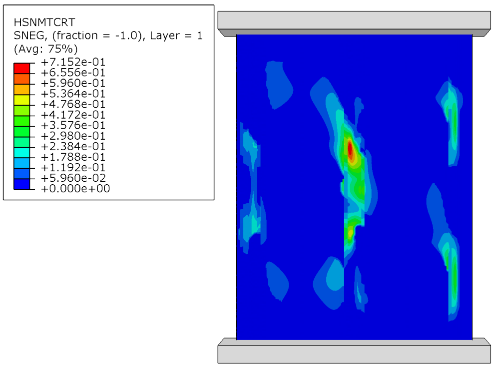

Figure 8.22: Hashin matrix tension criterion contour at the final failure load

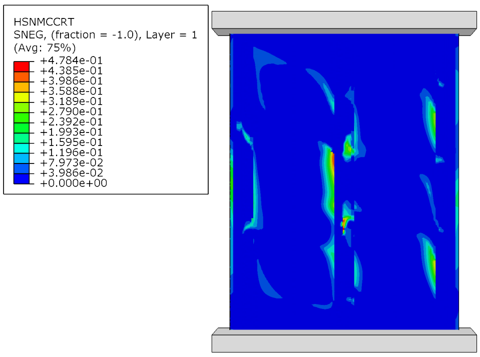

Figure 8.23: Hashin matrix compression criterion contour at the final failure load

8.4. Quasi-Static Analysis Results: XFEM (MAXPS Criterion)

This section of the report discusses the skin-stringer separation behaviour predicted by the Maximum Principal Stress (MAXPS) damage initiation criterion. Unlike the QUADS criterion, the MAXPS criterion allows crack growth in a completely solution-based arbitrary direction. In section 8.3, it was determined that Mesh Configuration 3 yielded a converged solution. Consequently, this model was employed to study crack growth behaviour using the XFEM modelling technique with the MAXPS criterion. As detailed in section 7.4, the MAXPS criterion is suitable for homogeneous, isotropic linear elastic materials. Accordingly, the interface section was idealised as an isotropic material with a Young's Modulus of 13252 MPa and a Poisson's ratio of 0.42 for modelling crack growth. The damage initiation stress was set at 87 MPa. The resulting STATUSXFEM contour, captured at the end of the analysis, is presented in Figure 8.24. The predicted load-displacement and crack-growth curves are also depicted in Figure 8.25.

Figure 8.24: Predicted crack growth behaviour trough the interface section: (a) Cap-side view; (b) Top Surface and (c) Bottom Surface

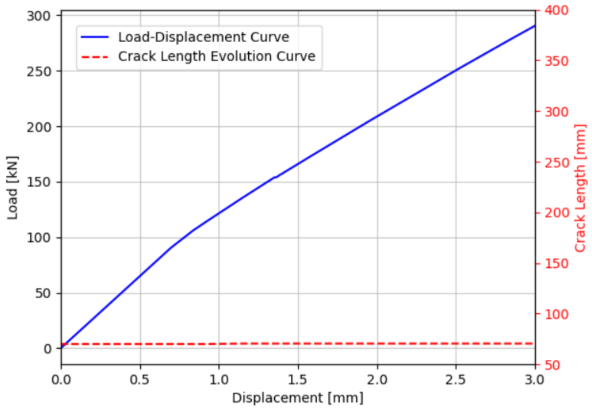

Figure 8.25: Load-displacement and crack length evolution curves: XFEM (MAXPS Criterion) model with mesh configuration 3

The model fails to capture the skin-stringer separation behaviour. After buckling, the model does predict the initiation of crack growth. However, the model predicts the crack to grow towards the bottom surface of the interface section. Crack growth is not observed once the crack tip reaches the bottom surface. Since the model fails to predict the evolution of skin-stringer separation, no load drop is observed in the load-displacement curve predicted by the model. It could be possible that the mesh requires further refinement. Therefore, a mesh in the interface section was further refined.

A mesh refinement would increase the computational cost of the resultant model. To minimise the increase in computation cost, the fine mesh was limited to the regions within the interface section where the crack growth is expected to occur in the post-buckling field. With this in mind, the interface section was partitioned as shown in Figure 8.26. The sections in green were defined with a fine mesh of 0.2 mm length elements. Based on the crack growth behaviour observed through the VCCT-based model and the XFEM (QUADS Criterion) model, this is the region where the crack growth is expected before the final failure load. The orange sections were defined with a mesh of uniform element length of 0.7 mm. The yellow regions act as a transition between the fine mesh regions and the coarse mesh regions. Here, using a bias, the element length is varied between 0.7 mm and 0.2 mm with the 0.2 mm length element being close to the green sections. Lastly, three-element layers were defined in the interface section. This will henceforth be referred to as mesh configuration 5. The crack growth predicted by the refined mesh model at the end of the analysis is presented in Figure 8.27 using STATUSXFEM contours.

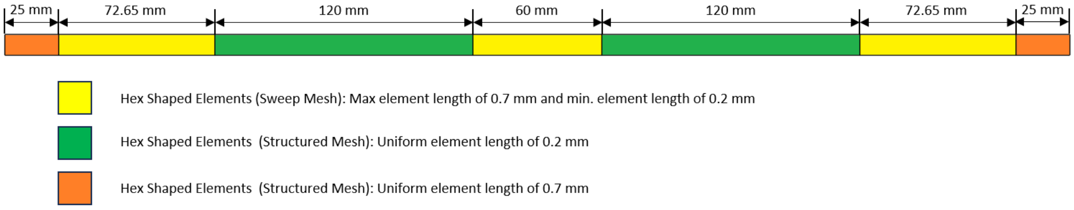

Figure 8.26: Partitioning of the interface section

Figure 8.27: Predicted crack growth behaviour trough the interface section: (a) Side view (Cap-side); (b) Top Surface and (c) Bottom Surface

The mesh refinement did not overcome the challenge faced by the earlier model. Furthermore, it is important to note that with a 0.2 mm element length, approximately 12 elements have been assigned along the cohesive zone length ahead of the crack tip. In the case of DCB specimens, where similar challenges were presented, a mesh refinement did allow the prediction of delamination until a displacement of 20 mm, beyond which numerical convergence issues were faced. In the case of the stiffened panel, a mesh refinement did not solve the same issue. Hence, three hypotheses were formulated to reason for this behaviour.

Hypothesis 1

The implementation of XFEM with the MAXPS damage initiation criterion in Abaqus may have limitations. Although it was possible to refine the mesh for DCB specimens to minimise these limitations, the same approach may not be effective for the stiffened panel due to the mixed mode crack growth behaviour at the skin-stringer interface. This contrasts with the DCB specimens, where pure mode 1 damage occurs. These observations are consistent with those of Camphilo et al., who also found that while the MAXPS damage initiation criterion is effective in modelling a DCB specimen, it fails to model the evolution of damage in the case of single and double lap joint specimens where mixed-mode damage is present [58][59][60]. The authors note that the model leads the crack growth towards and within the adherents in the presence of mixed-mode damage. Likewise, Fernandes et al. note that while the implementation in Abaqus could potentially be used to identify the locus of damage initiation in adhesive bonds and to predict the corresponding load as a rough estimate, it is unsuitable for predicting damage growth under mixed-mode conditions or along multi-material interfaces [61].

Hypothesis 2

Another possible reason could be that the model has accurately predicted that the crack propagates to the interface between the skin and the stringer, and any further delamination occurs along the interface in the form of an interface failure. However, the Abaqus implementation of XFEM only supports crack growth through a solid element, not along an interface. Therefore, the model cannot predict the resultant delamination along the skin-stringer interface. This is a likely cause, given that the test panels present a skin-stringer separation behaviour dominated by interface failure and skin-delaminations.

Hypothesis 3

Alternatively, even if the crack growth is expected to continue within the interface section, the limitations of the Abaqus implementation will not allow it. When the crack front reaches the bottom or top surface of the interface section, a new crack is expected to initiate close to the original crack front due to the stress concentrations in the region. However, the Abaqus implementation has a limitation where a new crack cannot be initiated close to an existing crack, as discussed in chapter 2. Moreover, any expected branching of the existing crack cannot be accounted for using the Abaqus implementation.

Several solutions have been proposed in the literature to address the challenges posed by XFEM in Abaqus. However, these workarounds have yielded varying degrees of success. Among the proposed solutions, two stand out. Stuparu et al. and Mubashar et al. suggested using Cohesive Zone Models (CZMs) at the interface between the adherend and adhesive while also enriching the adhesive with XFEM [62][63][64]. However, this approach presents an additional challenge. If the XFEM crack meets the interface, it cannot leave it again. Additionally, if the XFEM crack meets the centre of a conventional cohesive element, it is unclear how it should be treated.

Stein et al. encountered similar issues when modelling crack growth along multi-material adhesive joints [65]. To address this problem, they suggest using the UDMGINI subroutine. This subroutine uses an user-defined damage initiation criterion to allow the conventional algorithm to determine the crack growth direction when the crack tip is away from the interface. However, when the crack tip approaches the vicinity of the interface and is about to impinge on it, a user-defined crack direction is used to deflect the crack back into the adhesive. The results obtained using this approach showed potential and could be used to overcome the limitations of the Abaqus algorithm in modelling the skin-stringer separation behaviour.

Considering the suitable solutions, it was decided to develop a UDMGINI model to overcome the challenges in modelling the skin-stringer separation behaviour using the MAXPS damage initiation criterion. While the development of a physics-based damage initiation model is out of scope for the purpose of this thesis study, a series of experiments were conducted using finite element models to demonstrate the use of UDMIGINI in overcoming the limitations of the Abaqus model. Before delving into the UDMGINI model, it is important to provide a brief explanation of the UDMGINI subroutine.

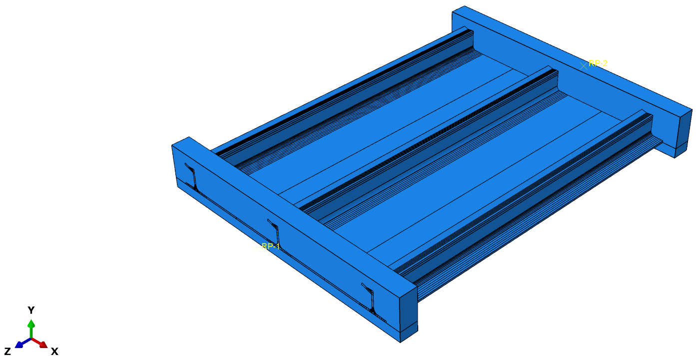

Figure 8.28: Stiffened panel assembly with the global coordinate system

UDMGINI is an Abaqus subroutine that allows users to define custom damage initiation criteria using one or more failure mechanisms. The subroutine code should be written to return FINDEX (NFINDEX) and FNORMAL (NDI, NFINDEX) variables. FINDEX is a vector that defines the indices for all failure mechanisms, and FNORMAL is an array that defines the normal direction to the fracture plane for each failure mechanism. NFINDEX and NDI are the number of indices for all failure mechanisms and the number of direct stress components at a given point, respectively. To better understand, consider the UDMGINI subroutine that employs the maximum principal stress, as shown below. The UDMGINI subroutine is defined in reference to the global coordinate system shown in Figure 8.28. This subroutine uses the built-in function ROTSIG to rotate the stress tensor to the global coordinate system and the SPRIND to calculate the principal stress values and directions. For more information, refer to the Abaqus documentation [40].

```fortran
      SUBROUTINE UDMGINI(FINDEX,NFINDEX,FNORMAL,NDI,NSHR,NTENS,PROPS,
     1 NPROPS,STATEV,NSTATEV,STRESS,STRAIN,STRAINEE,LXFEM,TIME,
     2 DTIME,TEMP,DTEMP,PREDEF,DPRED,NFIELD,COORDS,NOEL,NPT,LAYER,
     3 KSPT,KSTEP,KINC,KDIRCYC,KCYCLELCF,TIMECYC,SSE,SPD,SCD,SVD,
     4 SMD,JMAC,JMATYP,MATLAYO,LACCFLA,CELENT,DROT,ORI)
C
      INCLUDE 'ABA_PARAM.INC'

C
      DIMENSION FINDEX(NFINDEX),FNORMAL(NDI,NFINDEX),COORDS(*),
     1 STRESS(NTENS),STRAIN(NTENS),STRAINEE(NTENS),PROPS(NPROPS),
     2 STATEV(NSTATV),PREDEF(NFIELD),DPRED(NFIELD),TIME(2),JMAC(*),
     3 JMATYP(*),DROT(3,3),ORI(3,3)
C ------------- USER CODE TO DEFINE FINDEX AND FNORMAL -------------
C
C
      DIMENSION PS(3), AN(3,3), WT(6)
      PS(1)=0.0
      PS(2)=0.0
      PS(3)=0.0
C
C ROTATE THE STRESS TO THE GLOBAL SYSTEM IF THERE IS ORIENTATION
C
      CALL ROTSIG(STRESS,ORI,WT,1,NDI,NSHR)
C
C MAXIMUM PRINCIPAL STRESS CRITERION
C
      CALL SPRIND(WT,PS,AN,1,NDI,NSHR)
      SIG1 = PS(1)
      KMAX=1
      DO K1 = 2, NDI
         IF(PS(K1).GT.SIG1) THEN
            SIG1 = PS(K1)
            KMAX = K1
         END IF
      END DO
      FINDEX(1) = SIG1/PROPS(1)
      DO K1=1, NDI
              FNORMAL(K1,1) = AN(KMAX,K1)
      END DO
C

C ----------------------- END OF USERCODE -----------------------
      RETURN
      END
```

Three different approaches were tested to overcome the limitations of the commercial implementation of the MAXPS damage initiation criterion. These approaches were introduced to the finite element model by modifying the UDMGINI subroutine shown above. A description of the approaches considered for this experimental study is detailed below:

1. **Case 1:** The maximum principal stress criterion is solely used to assess damage initiation. When the damage initiation criterion is met, a user-defined fracture plane is defined parallel to the length of the stiffened panel through the FNORMAL variable. This approach is very similar to the Abaqus implementation of QUADS damage initiation, where the crack growth direction is user-defined. The distinction lies in the fact that, in this case, the damage initiation criterion uses the maximum principal stress to assess damage instead of a quadratic stress criterion (Equation 2.8).

```
C MAXIMUM PRINCIPAL STRESS CRITERION
C
  CALL SPRIND(WT,PS,AN,1,NDI,NSHR)
  SIG1 = PS(1)
  KMAX=1
  DO K1 = 2, NDI
     IF(PS(K1).GT.SIG1) THEN
        SIG1 = PS(K1)
        KMAX = K1
     END IF
  END DO
  FINDEX(1) = SIG1/PROPS(1)
  FNORMAL(:,1) = [0,1.0,0]
C
```

2. **Case 2:** The second approach utilises the maximum principal stress to determine damage initiation and fracture plane, as illustrated below. To promote crack growth along the length of the panel, a bias factor (represented by a placeholder variable BIAS_FACTOR) was introduced to the y-axis component of the FNORMAL vector. The bias factor aligns the normal vector towards the y-axis, promoting crack growth along the length of the panel. For this study, BIAS_FACTOR values of 5 and 10 were considered.

```
C MAXIMUM PRINCIPAL STRESS CRITERION
C
      CALL SPRIND(WT,PS,AN,1,NDI,NSHR)
      SIG1 = PS(1)
      KMAX=1
      DO K1 = 2, NDI
         IF(PS(K1).GT.SIG1) THEN
            SIG1 = PS(K1)
            KMAX = K1
         END IF
      END DO
      FINDEX(1) = SIG1/PROPS(1)
      DO K1=1,NDI
              IF(K1.EQ.2) THEN
                 FNORMAL(K1,1)=BIAS_FACTOR*AN(KMAX,K1)
              ELSE
                 FNORMAL(K1,1)=AN(KMAX,K1)
        END IF
      END DO
C
```

3. **Case 3:** The third approach is similar to the solution proposed by Stein et al. [65]. Here, damage initiation in the enriched elements is evaluated using the maximum principal stress criterion. Upon damage initiation, the fracture plane is defined differently for each element layer in the interface section (see Figure 8.29). The normal to the fracture plane in Element Layer - 2 is defined based on

the maximum principal stress direction, while the normal to the fracture plane in Element Layers 1 and 3 is defined to deflect the crack back towards Element Layer - 2. This study considered the crack deflection angles of 2.5° and 5°.

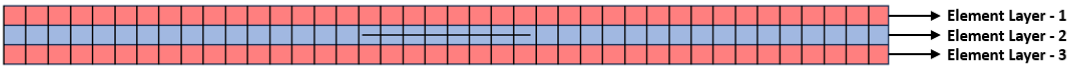

Figure 8.29: Definition of element layers in the interface section

```
C MAXIMUM PRINCIPAL STRESS CRITERION
C
      CALL SPRIND(WT,PS,AN,1,NDI,NSHR)
      SIG1 = PS(1)
      KMAX=1
      DO K1 = 2, NDI
         IF(PS(K1).GT.SIG1) THEN
            SIG1 = PS(K1)
            KMAX = K1
         END IF
      END DO
      FINDEX(1) = SIG1/PROPS(1)
      DO K1=1, NDI
              FNORMAL(K1,1) = AN(KMAX,K1)
      END DO

C
C IF LOOPS TO CONTROL THE CRACK DIRECTION IN THE RESTRICTED REGIONS
C
C IF LOOP FOR THE REAR HALF OF ELEMENT LAYER - 1
      IF(NOEL>=77921 .AND. NOEL<=93504) THEN
          FNORMAL(:,1) = [0.0, 1.0, -tan(θ)]
      END IF
C
C IF LOOP FOR THE REAR HALF OF ELEMENT LAYER - 3
      IF(NOEL>=46753 .AND. NOEL<=62336) THEN
          FNORMAL(:,1) = [0.0, 1.0, tan(θ)]
      END IF
C
C IF LOOP FOR THE FRONT HALF OF ELEMENT LAYER - 1
      IF(NOEL>=31169 .AND. NOEL<=46752) THEN
          FNORMAL(:,1) = [0.0, 1.0, tan(θ)]
      END IF
C
C IF LOOP FOR THE FRONT HALF OF ELEMENT LAYER - 3
      IF(NOEL>=1 .AND. NOEL<=15584) THEN
          FNORMAL(:,1) = [0.0, 1.0, -tan(θ)]
      END IF
C
```

Having discussed the modifications introduced using the UDMGINI subroutine, the results obtained using the resultant finite element models are discussed in the following subsections.

8.4.1. Skin-Stringer Separation Behaviour

Case-1

In the finite element model with mesh configuration 5, the UDMGINI subroutine was introduced, which resulted in the evolution of crack length shown in Figure 8.30. The growth trend of the curve is similar to what was predicted using the QUADS criterion. However, there is a difference in the crack growth behaviour between the two criteria. While the QUADS-based criterion predicts a mix of stable and unstable crack growth, the maximum principal stress criterion predicts stable crack growth in this case. Nevertheless, the model with the maximum principal stress criterion under-predicts the crack length at the final failure load, which is 129.1 mm.

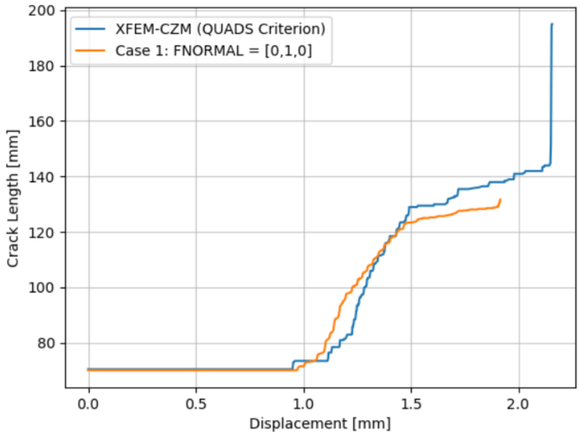

Figure 8.30: Crack length evolution curves obtained using the finite element model for Case 1 (Mesh Configuration 5)

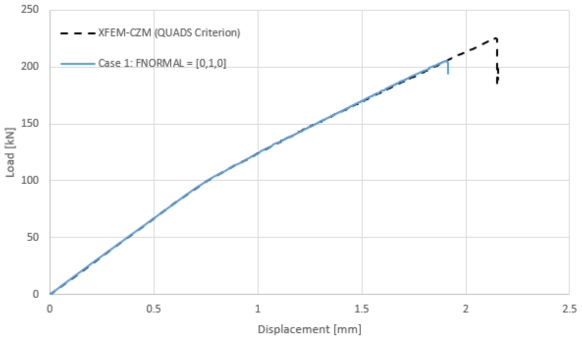

Figure 8.31: Load-Displacement curves obtained using the finite element model for Case 1 (Mesh Configuration 5)

It is worth noting that the reason for the under-prediction of the crack length becomes clear when the STATUSXFEM contour of the non-cap side of the interface section is evaluated at the final failure load (see Figure 8.32). Instead of moving forward, the crack tip started propagating backwards. Furthermore, branching of the original crack was observed to a certain extent. Although this could be modelled due to the use of the user subroutine, the evolution of the resultant cracks was not predicted well. Hence, the model underestimated the crack length evolution.

Figure 8.32: STATUSXFEM contour obtained from the non-cap side view of the interface section for Case 1 (Mesh Configuration 5)

Multiple cracks were initiated in the same region due to the presence of three element layers. However, the Abaqus implementation of damage evolution was unable to model the loss of stiffness of the damaged elements. Therefore, to simplify the model, the same user damage criterion was introduced to a finite element model with mesh configuration 3, which had a single element layer in the interface section. The resulting crack length evolution and load-displacement curves are shown in Figure 8.33 and Figure 8.34, respectively. The crack length evolution curve is significantly different from the previous model. Furthermore, the model shows a closer correlation with the test panels and the VCCT-based model with a 169.8 mm crack length at the final failure load. Beyond the final failure load, the model exhibits unstable crack growth. Analysing the load-displacement curve predicted by the model, it is evident that while the stiffness remains the same as the XFEM (QUADS Criterion) model in the linear and non-linear domain, the maximum load predicted by the model is significantly higher at 245.795 kN.

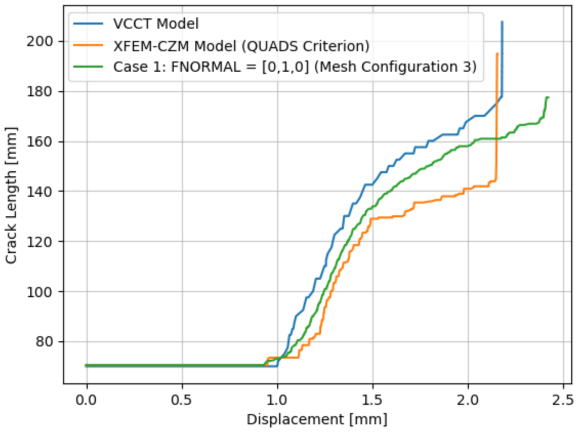

Figure 8.33: Crack length evolution curves obtained using the finite element model for Case 1 (Mesh Configuration 3)

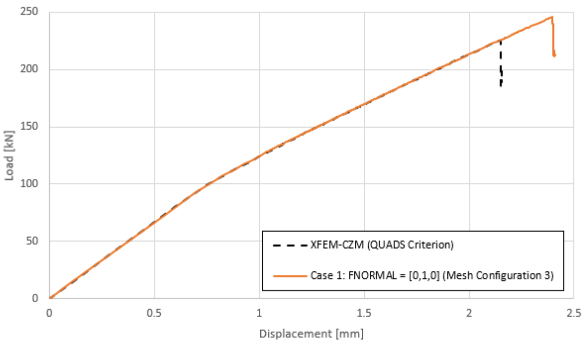

Figure 8.34: Load-Displacement curves obtained using the finite element model for Case 1 (Mesh Configuration 3)

The STATUSXFEM contour was captured from both the cap side and bottom of the interface section at the final failure load and can be seen in Figure 8.38. The model does not exhibit any issues related to crack tip impingement, which is a good sign. Additionally, the model can accurately predict the semi-elliptical shape of the skin-stringer damage that was observed in previous models and test panels. While the model overestimates the final failure load, overall, the model with mesh configuration 3 and case 1 of the user damage initiation criterion seems promising.

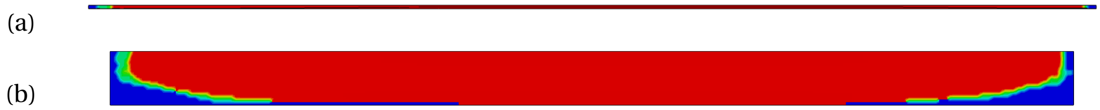

Figure 8.35: Predicted crack growth behaviour trough the interface section (Case 1 - Mesh Configuration 3): (a) Cap-side view; (b) Bottom Surface

Case-2

The crack length evolution curves obtained using the finite element models are depicted in Figure 8.36. The crack length evolution curve obtained using the model based on the QUADS criterion is also presented as a reference. In contrast to case 1, the attempt to modify the fracture plane using a bias factor was unsuccessful. The crack length evolution curve initially shows a stable crack growth behaviour, but it becomes apparent that the crack length starts to plateau after a certain point. At around a load of 173 kN, both finite element models encountered numerical convergence issues, leading to a failure in the analysis beyond this point. The message files identified the STD_FINDCUTSHAPE3D8_XFEM error as the cause of this failure. Although the official Abaqus documentation does not provide details about this error, it is hypothesised that it arises from using a user-defined fracture plane. The initiation of damage and the resultant fracture plane is evaluated at the integration point of the enriched elements using the user subroutine. As a result, the shape of the delamination modelled by the finite element model is complex and not continuous. When the complex crack fronts approach each other, they fail to connect or merge at a specific element. This causes a numerical error. Lastly, judging the load-displacement curves in Figure 8.37, it is evident that the model overestimates the stiffness in the non-linear region. This is expected because the model underestimates the skin-stringer separation in the post-buckling domain.

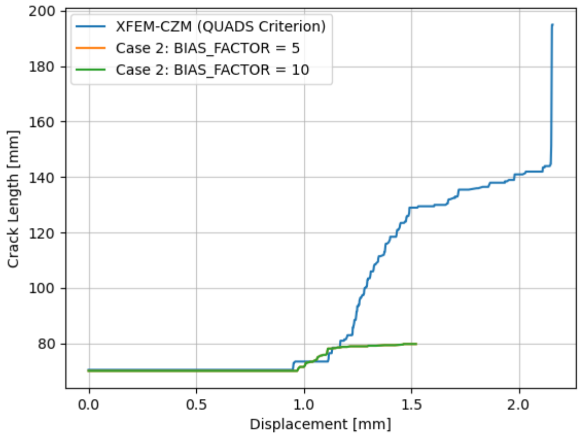

Figure 8.36: Crack length evolution curves obtained using the finite element model for case 2

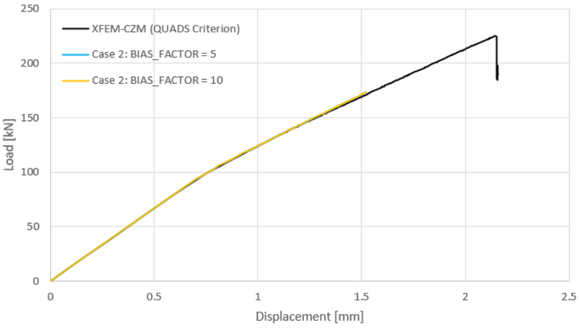

Figure 8.37: Load-Displacement curves obtained using the finite element model for case 2

The shape of the predicted delamination was assessed by analysing the STATUSXFEM contours, which were captured just before the model failed. The contours for the finite element models with BIAS_FACTOR values of 5 and 10 are presented in Figure 8.38 and Figure 8.39. The cap-side view of the STATUSXFEM contours clearly demonstrates the effect of the bias factor. Unlike the original Abaqus algorithm, the crack front can travel further before reaching the bottom surface. Additionally, the contours taken from the bottom surface indicate that only the crack front near the cap side meets the bottom surface. However, due to incomplete analysis, no definitive conclusions could be drawn.

Figure 8.38: Predicted crack growth behaviour trough the interface section (BIAS_FACTOR = 5): (a) Cap-side view; (b)Bottom Surface

Figure 8.39: Predicted crack growth behaviour trough the interface section (BIAS_FACTOR = 10): (a) Cap-side view; (b)Bottom Surface

Case-3

Like the models evaluated for Case 2, the deflection angle models also failed to converge beyond a certain load. Referring to the message files, STD_FINDCUTSHAPE3D8_XFEM error was identified as the cause of failure. The explanation for the cause of error should be the same as for Case 2, wherein the use of the crack deflection approach results in a prediction of a complex shape of the delamination along the interface section. The models in this case, fail to converge beyond a load of around 130 kN, which is earlier than case 2. This is explainable because using a solution-based approach in Element Layer 2 and a user-defined fracture plane for Element Layers 1 and 3 would have caused numerical convergence issues when merging or connecting the crack fronts at a given element. This mixed approach makes it difficult for the Abaqus model to predict the continuity of the crack front along the interface section. Hence the early failure.

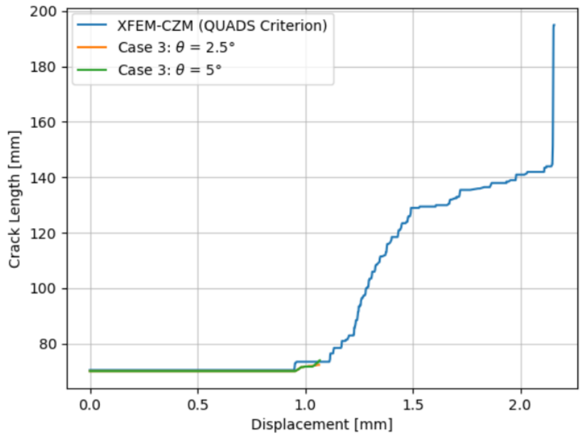

Figure 8.40: Crack length evolution curves obtained using the finite element models for Case 3

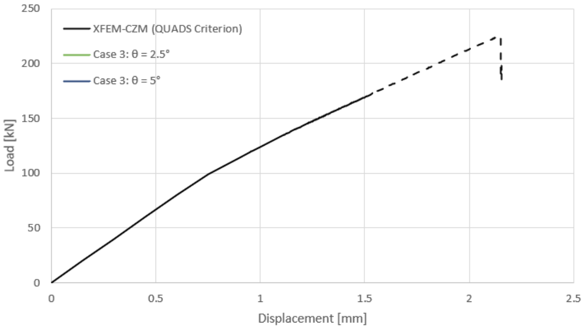

Figure 8.41: Load-Displacement curves obtained using the finite element models for Case 3

The STATUSXFEM contours were captured from the cap-side view and on the bottom surface for the models with cracked deflection angles of 2.5° and 5°. They are shown in Figure 8.42 and Figure 8.43 respectively. These contours were captured just before the models failed. The cap-side views of the models demonstrate the successful implementation of the crack deflection algorithm. In both scenarios, when the crack tip moves from Element Layer 2 to Element Layer 3, the crack is successfully deflected back to Element Layer 2. Furthermore, the bottom surfaces of both models show that only a very small portion of the crack tip reaches the bottom surface. This could be because when the crack tip moves from Element Layer 2 to Element Layer 3, the Abaqus algorithm attempts to maintain the continuity of the crack front. If continuity cannot be maintained using the user-defined fracture plane, Abaqus uses a solution-based fracture plane. Therefore, in such scenarios, it has been observed that the crack tip may still manage to reach the bottom surface.

Figure 8.42: Predicted crack growth behaviour trough the interface section (deflection angle = 2.5°): (a) Cap-side view; (b)Bottom Surface

Figure 8.43: Predicted crack growth behaviour trough the interface section (deflection angle = 5°): (a) Cap-side view; (b)Bottom Surface

8.4.2. Discussion

After analysing three cases, it can be concluded that the model investigated in Case 1 with mesh configuration 3 performs better than those analysed in Cases 2 and 3. The reason is that the model in Case 1 can predict the stable crack length evolution leading up to the final failure load and the unstable crack growth that follows it. On the other hand, the models analysed in Cases 2 and 3 could not predict the crack length evolution in the post-buckling field. This was due to the introduction of a modification to the user subroutine, resulting in an irregular crack shape along the interface section. As a result of this, the models encountered numerical convergence issues when merging the complex crack front. Consequentially, the analysis failed after a certain load point, making using a bias or a crack deflection strategy an unreliable method for modelling the skin-stringer separation.

In Case 1, a uniform user-defined fracture plane was defined, resulting in a relatively less complex delamination shape and no convergence issues. Additionally, the models in Cases 2 and 3 still showed crack impingement on the bottom surface of the interface section to varying extents, while the crack impingement problem was absent in the model evaluated for Case 1.

In summary, Case 1, which utilised the maximum principal stress criterion to determine the initiation of failure and a user-defined fracture plane along the length of the panel, is selected for further investigations. The absence of convergence issues and improved modelling of crack propagation make it the best option among the three cases. Henceforth, the finite element model with mesh configuration 3, from Case 1, will be regarded as the representative model for XFEM (MAXPS Criterion) in this report.

8.4.3. Out-of-plane Displacement

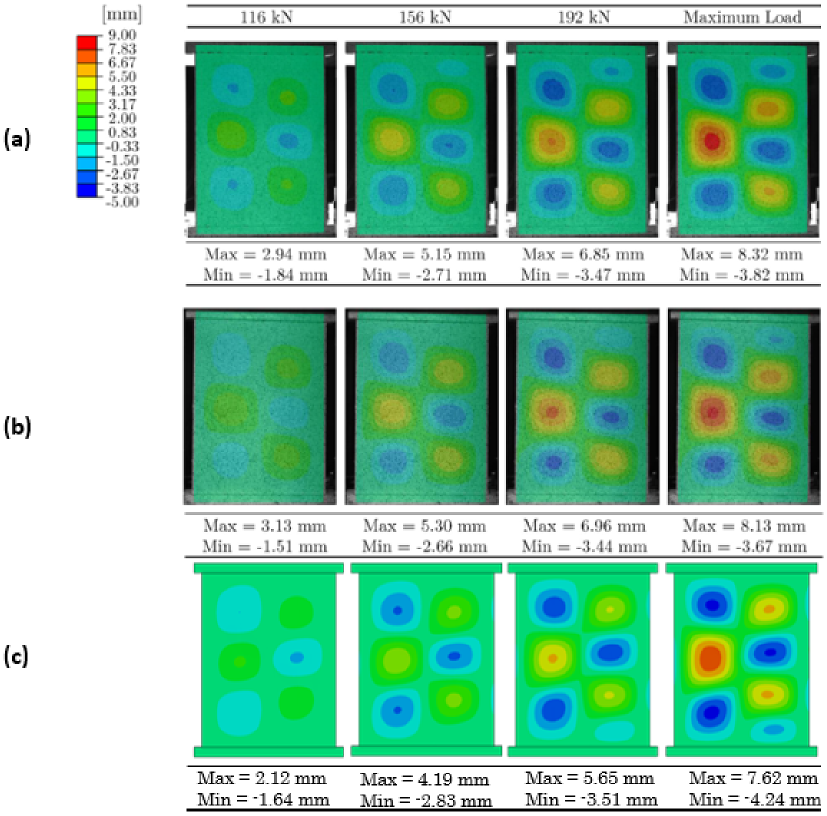

Figure 8.44: Out-of-plane displacement: (a) Test Panel 1; (b) Test Panel 2 and (c) FE Model (Maximum Principal Stress - Case 1)

In this subsection, the out-of-plane deformations predicted by the model selected in subsection 8.4.2 are evaluated. The out-of-plane displacement contours were captured at four load levels: 116 kN, 156 kN, 192 kN, and the maximum load of 245.795 kN. The displacement contours were compared with those from test panels 1 and 2, as shown in Figure 8.44. After buckling, the finite element model successfully predicted the formation of three half-waves in each bay. The position of these half-waves was in good agreement with the test panels. Additionally, at higher loads, the model replicated the initiation of the fourth half-wave in the right bay of the panel. However, the model predicted the fourth half-wave to form at the bottom of the right bay, whereas in the test panels, it forms on the top of the right bay. The magnitude of inward deformations (positive), towards the stringer was underestimated at all load levels, while the magnitude of outward deformations (negative), away from the stringer was overestimated at all load levels. This could be linked to the interaction of the out-of-plane deformations, the skin-stringer separation in the post-buckling field, and the geometric imperfections introduced to the model.

8.4.4. Hashin Failure Criterion

After analysing the composite skin sections of the panel using the Hashin fibre and matrix failure criterion contours captured from the front view of the panel at the final failure load, it is clear that there is fibre compression failure in the skin section that is in contact with the middle stringer. This result was expected based on the previous models. The composite sections' layups, panel geometry, and out-of-plane deformations were similar in the models being considered, and thus the damage observed within the composite sections is also similar.

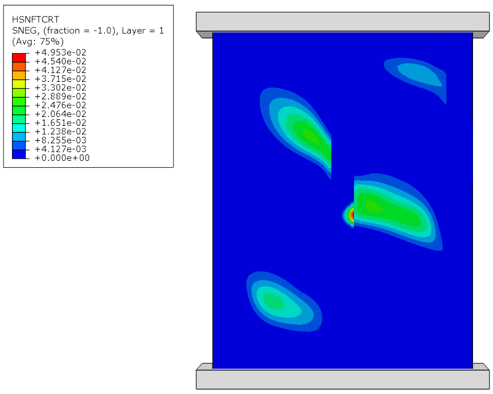

Figure 8.45: Hashin fibre tension criterion contour at the final failure load (MAXPS Model - Case 1)

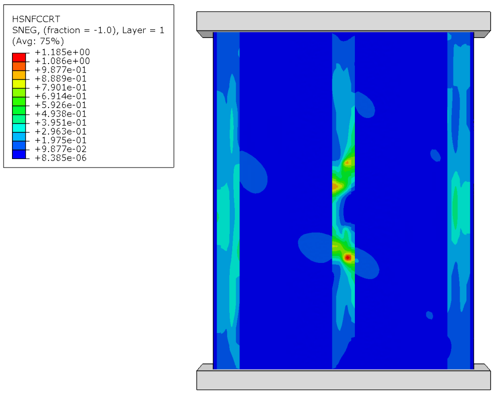

Figure 8.46: Hashin fibre compression criterion contour at the final failure load (MAXPS Model - Case 1)

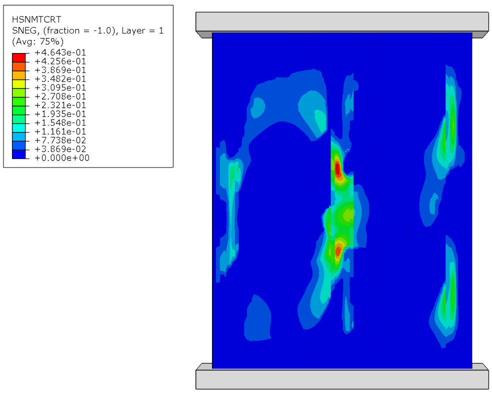

Figure 8.47: Hashin matrix tension criterion contour at the final failure load (MAXPS Model - Case 1)

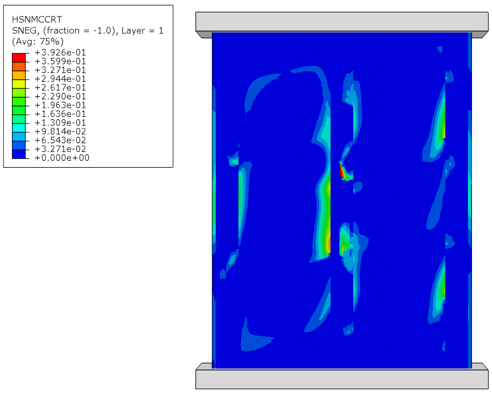

Figure 8.48: Hashin matrix compression criterion contour at the final failure load (MAXPS Model - Case 1)

8.5. Comparison of VCCT and XFEM Based Models

So far, the post-buckling behaviour and the skin-stringer separation behaviour obtained from three damage modelling algorithms of VCCT, XFEM (QUADS Criterion), and XFEM (MAXPS Criterion) have been evaluated individually. This section compares these models based on the resultant skin-stringer separation behaviour, load-displacement curves, computational efficiency and issues related to numerical stability.

8.5.1. Load Displacement Curves

Analysing the load-displacement curves in Figure 8.49, the following observations can be made:

1. The finite element models predict the linear stiffness of the test panels very well.
2. The finite element models overestimate the stiffness of the test panels in the post-buckling domain. This is likely due to one of the idealisations made while modelling the stiffened panel. The model did not consider the skin-stringer separation in the outer stringers. Furthermore, the model did not consider the separation between the webs and the caps. Lastly, delamination in the skin sections was also not considered. Modelling them would result in additional loss of stiffness in the post-buckling domain.
3. The VCCT and XFEM (QUADS criterion) finite element models show a slight overestimation of the final failure load of the test panels. On the other hand, the XFEM (MAXPS Model) predicts the final failure load to be 245.795 kN, which is 10.22% and 13.84% higher compared to the final failure load observed for test panels 1 and 2, respectively. This overestimation of the final failure loads by the finite element models is likely related to underestimating the loss of stiffness in the non-linear region.

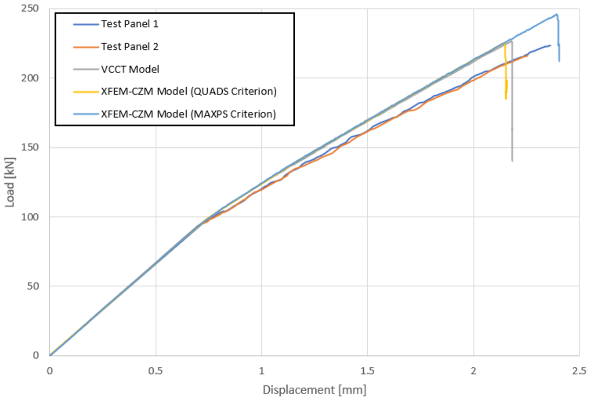

Figure 8.49: Load-displacement curves obtained from the test panel and the finite element models

Based on the analysis of the curves, it can be inferred that both VCCT and XFEM (QUADS Criterion) damage modelling techniques are equally reliable in predicting the load-displacement curves of the stiffened panels under consideration. While the XFEM (MAXPS Criterion) model is equally reliable in predicting the load-displacement curve in the linear and non-linear region, it significantly over-predicts the final failure load of the stiffened panel under consideration. This could be related to using a user-defined fracture plane in the XFEM (MAXPS Criterion), which may not account for the physical behaviour at the skin-stringer interface well. Further comparisons between the models are made in the subsections that follow.

8.5.2. Skin-Stringer Separation Behaviour

The behaviour of skin-stringer separation was evaluated using three damage modelling techniques: VCCT, XFEM (QUADS Criterion), and XFEM (MAXPS Criterion). The corresponding crack length evolution curves for these models were plotted, as shown in Figure 8.50. The test panels showed a skin-stringer separation of 196.5 mm at the final failure load. However, the damage modelling techniques used in this study underestimated the crack length at the final failure load. VCCT provided the closest prediction, with a crack length of 178 mm. The XFEM (QUADS criterion) model underestimated the crack length by approximately 26.4%, with a prediction of 144.5 mm. Despite this discrepancy, the final failure load and the transition from relatively stable crack growth to the unstable crack growth phase occurred nearly at the same load level. On the other hand, the crack length evolution curve predicted by the XFEM (MAXPS Criterion) model shows a similar trend to that of the VCCT-based model, wherein the crack length evolution is primarily stable. Compared to the XFEM (QUADS Criterion) model, the error in the prediction of the crack length at the final failure load is reduced in the case of the XFEM (MAXPS Criterion) model, but at 169.8 mm, it is still underestimated.

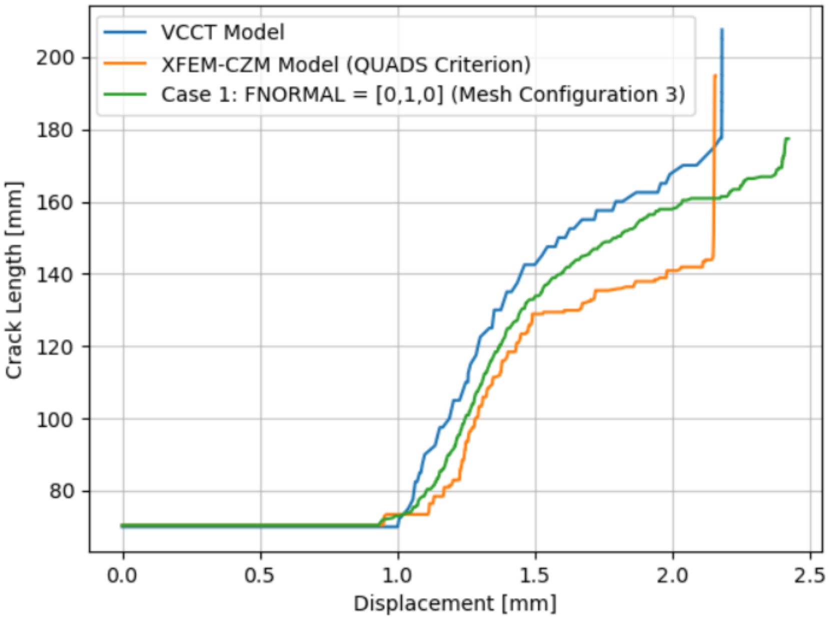

Figure 8.50: Comparison of the crack length evolution predicted by different damage modelling techniques

The underestimation of the crack length could be due to the lack of geometric imperfections for modelling the test panels. Literature suggests that geometric imperfections introduced to the models could influence the buckling load of the modelled panels. Generally, adding imperfections causes the panel to buckle at a lower load level. Since the skin-stringer separation behaviour is driven by the mode 1 opening of the initial 70 mm delamination, the load level at which buckling occurs influences when the skin-stringer delamination begins to grow.

The crack length underestimation by the XFEM (QUADS criterion) and XFEM (MAXPS criterion) could also be attributed to the parameters used to define the two damage modelling techniques under consideration. Firstly, additional parameters, i.e., the nominal stress values (normal and shear stresses) for XFEM (QUADS criterion) and the critical principal stress for XFEM (MAXPS), are considered when modelling cracks using the XFEM. These values are used when initiating crack growth at the skin-stringer interface. While the BK-fracture criterion parameters used for delamination using VCCT and the damage evolution in the XFEM techniques were experimentally obtained for the PEKK-SFRP material under consideration, the nominal and critical stress values used to initiate the damage in the XFEM techniques were approximated based on a material characterisation study carried out for a similar material. This approximation could have influenced damage initiation within the enriched elements in the post-buckling field. An additional approximation was made for the XFEM (MAXPS) criterion model wherein the interface section was idealised as an isotropic, homogeneous material, making it stiffer in the transverse directions when compared to the original PEKK SFRP material.

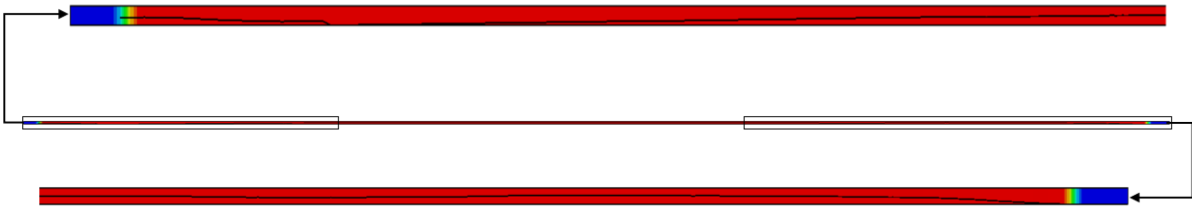

Figure 8.51: STATUSXFEM Contour captured from the XFEM (QUADS Criterion) at the final failure load (Cap side of the interface section)

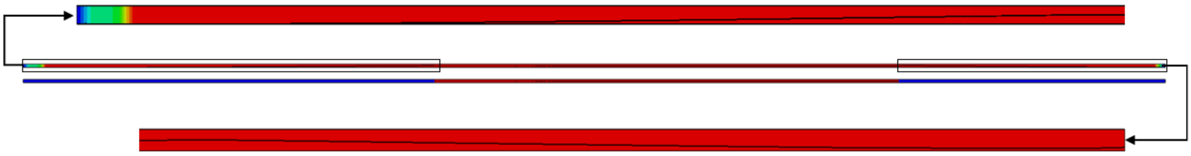

Figure 8.52: STATUSXFEM Contour captured from the XFEM (MAXPS Criterion) at the final failure load (Cap side of the interface section)

Lastly, the term 'crack length' in this context considers the distance between the farthest nodes of the failed elements. The way these techniques model damage must also be considered. VCCT models the delamination along a 2D interface between the skin and the filler, while XFEM models the crack through the solid interface. The three-dimensional crack growth behaviour is evident from Figure 8.51 and Figure 8.52, where the STATUSXFEM contour captured from the cap-side of the interface section at the final failure load is shown. This means the fracture surface modelled using XFEM is a complex 3D surface, unlike the 2D fracture surface modelled by VCCT. Therefore, it could be the case that the fracture surface area in both cases is similar. However, this could not be verified during this thesis study, as the resultant ODB files do not contain the necessary information to compute the fracture surface area.

All three models predict semi-elliptical damage in the skin-stringer interface. This is because of the buckling mode shape of the panel, where an outward half-wave in the skin bay on the cap side creates a mode 1 opening of the initial crack at the skin-stringer interface. A thin strip of the interface remains attached to the skin due to the presence of an inward half-wave in the adjacent skin bay. At higher loads, a smaller fourth half-wave is formed, which pushes the initial half-waves in the skin bay on the cap side upwards of the stiffened panel. As a result, the crack front grows more upwards. Beyond the formation of the fourth half-wave, the filler attached to the skin on the non-cap side begins to detach from the skin as the magnitude of out-of-plane deformations increases. This enables the formation of a tunnel under the middle stringer, which drives unstable crack growth at the skin-stringer interface and results in a significant loss of load-bearing capacity of the stiffened panel. Consequently, beyond this point, a load drop is observed. The predicted skin-stringer separation and the out-of-plane deformations in the stiffened panel at the maximum load of the models (VCCT, XFEM (QUADS Criterion) and XFEM (MAXPS Criterion)) are compared in Figure 8.53.

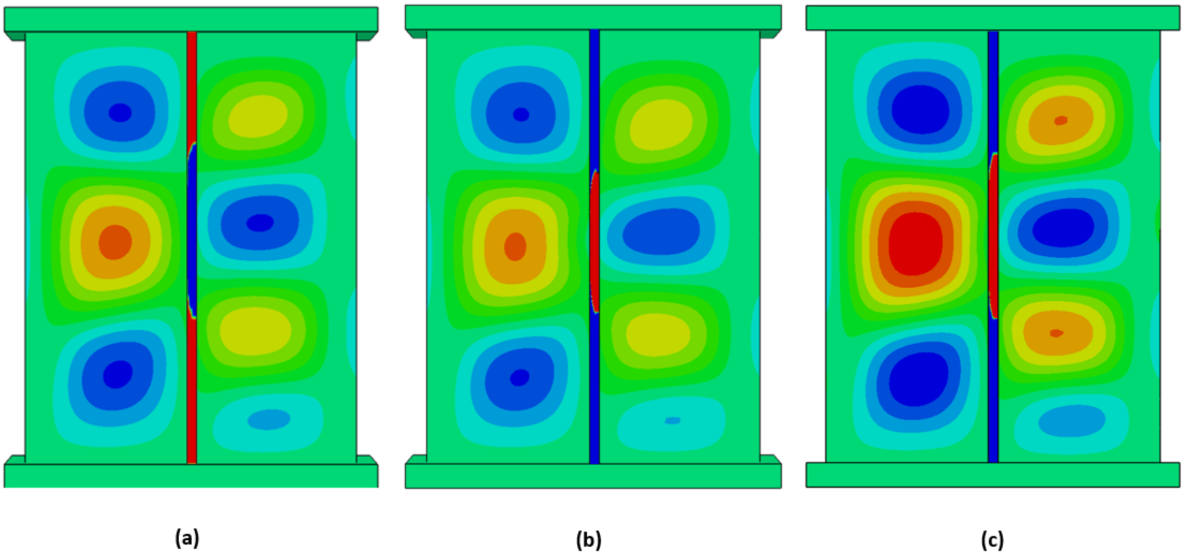

Figure 8.53: Out-of-plane displacement and STATUSXFEM contours at maximum load: (a) VCCT Model; (b) XFEM (QUADS Criterion) Model and (c) XFEM (MAXPS Criterion) Model

8.5.3. Post-Buckling Deformations

This subsection compares the out-of-plane deformations obtained from the finite element models (refer to Figure 8.54) to those found in the test panels (refer to Figure 8.55). It is evident that the finite element models tend to underestimate the magnitude of inward (positive) deformations towards the stringer while they overestimate the outward (negative) deformations away from the stringer. This could be due to the geometric imperfections introduced in these models. Also, loading imperfections present in the test panels could influence the out-of-plane deformations. At load levels 116 kN, 156 kN, and 192 kN, the magnitude of out-of-plane deformations predicted by the finite element models are closer to each other when compared to those at the maximum loads. At the maximum load, the VCCT and XFEM (QUADS Criterion) models show closer magnitudes of deformations, while the XFEM (MAXPS Criterion) has a higher magnitude of deformations. This can be explained by the fact that the maximum load in the VCCT and XFEM (QUADS Criterion) models are close to each other, while the maximum load in the XFEM (MAXPS Criterion) is higher. It, therefore, can be established that the magnitude of the out-of-pane deformations depends on the geometric imperfections introduced to the model and the load level at which they are captured.

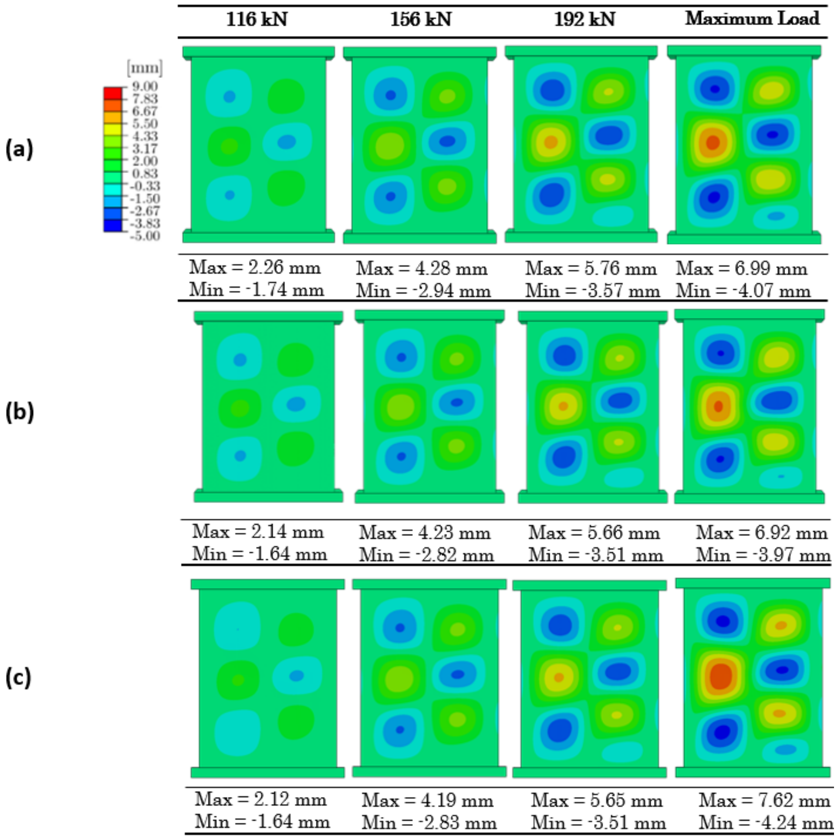

Figure 8.54: Out-of-plane displacement contours obtained from the finite element models: (a) VCCT; (b) XFEM (QUADS Criterion) and (c) XFEM (MAXPS Criterion)

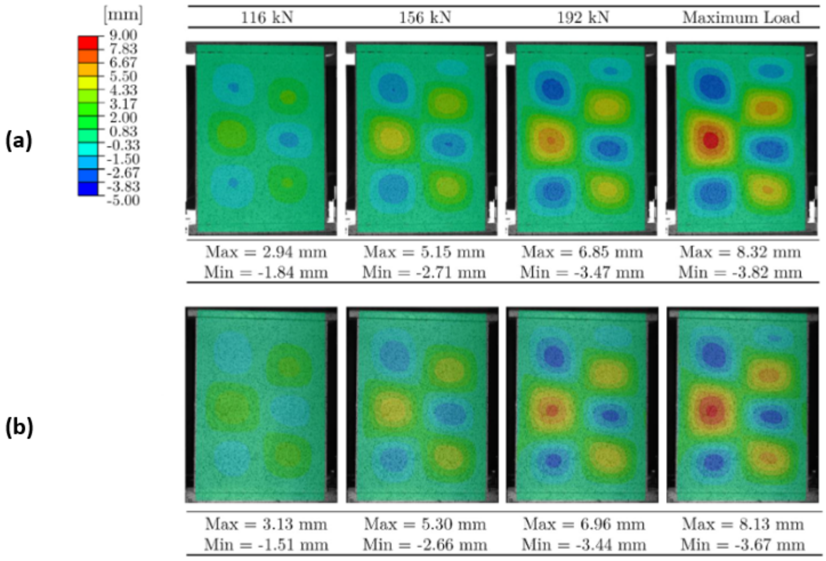

Figure 8.55: Out-of-plane displacement contours: (a) Test Panel 1 and (b) Test Panel 2 [50]

The finite element models accurately predict the formation of three half-waves in each skin bay in terms of their shape and position. They also predict the formation of a smaller fourth half-wave in the right bay, but its position is at the bottom of the panel instead of the top, as observed in the test panels. This can be related to the geometric imperfections introduced to the models that could have influenced the post-buckling deformations. Furthermore, it was later discovered that there is a discrepancy in the stacking sequence of the layup reported by Dooren et al. and the test panels. This discrepancy lies in the skin sections, where +45° and -45° were interchanged. Unfortunately, due to time constraints, changes resulting from this discovery could not be incorporated into the existing models of the thesis project.

8.5.4. Computational Efficiency

The total CPU time taken by each finite element model was noted from the message file and tabulated in Table 8.4 to evaluate their computational efficiency. Comparing the VCCT and XFEM (QUADS Criterion) based models, it can be observed that the use of the XFEM technique increased the computation time. However, the increase was not significant. It is important to note that the mesh used in the outer skin and the outer stringer section of the XFEM (QUADS Criterion) is relatively coarse compared to the VCCT-based model. Despite this, the results obtained from both models were comparable.

Model	**CPU Time [s]**
VCCT Model	172553
XFEM (QUADS Criterion) Model	174785
XFEM (MAXPS Criterion) Model	253209

Table 8.4: Total CPU times corresponding to each finite element model

In the case of the XFEM (MAXPS Criterion) model, the increase in CPU time compared to the VCCT-based model and the XFEM (QUADS Criterion) model is significant. Given that the mesh configuration used in the XFEM (QUADS Criterion) and XFEM (MAXPS Criterion) is the same, this increase in CPU time can be associated with the higher failure load and the numerical instabilities while modelling damage using XFEM (MAXPS Criterion).

8.5.5. Discussion on numerical stability

Based on the modelling experience during the implementation of the finite element models, the following observations were made for each of the damage modelling techniques in terms of their numerical stability:

1. VCCT Based Model: The implementation of VCCT in Abaqus did not present challenges regarding

numerical instabilities. While modelling, it was observed that the minimum increment size defined in the load step plays a huge role in determining the numerical stability of the model. Based on experience, it was observed that a minimum increment size of around 1E-08 performed better compared to smaller values. This is because when the fracture criterion exceeds the defined tolerance, Abaqus performs a cut-back in the increment size to half of the minimum increment size. The use of significantly smaller increment sizes gave rise to numerical instabilities.

2. XFEM (QUADS Criterion): The implementation of XFEM (QUADS Criterion) in Abaqus did not present any convergence issues. While to improve solution convergence, the maximum number of cutbacks allowed for an increment was changed from the default value of 5 to 15, during the analysis, it was observed that the maximum number of cutbacks performed by the solver was not more than 6.

3. XFEM (MAXPS Criterion): The commercial implementation of Abaqus for XFEM (MAXPS Criterion) was unreliable in predicting the mixed-mode damage behaviour within the skin-stringer interface. The model presented the issue of crack tip impingement on the surface of the interface section, and once the impingement occurred, the model could not initiate a new crack or continue the growth of the existing one. To overcome this issue, the UDMGINI subroutine was used. However, modifying the solution-based fracture plane created issues in crack front connectivity, resulting in numerical convergence issues. Additionally, it was found that when the damage in the enriched region becomes complex due to the user-defined damage initiation criterion, the implementation of damage evolution in Abaqus cannot model it well. Unfortunately, Abaqus does not provide a provision to introduce a user-defined damage evolution algorithm. Hence, a compromise had to be made by defining a uniform fracture plane along the length of the stiffened panel (FNORMAL = [0,1,0]).

In summary, the numerical stability of the finite element models in Abaqus was influenced by the damage modelling technique. The VCCT and XFEM (QUADS Criterion) based models showed robust stability, benefiting from an adjustment in the maximum number of cutbacks. However, the XFEM (MAXPS Criterion) faced several issues, including crack tip impingement and limitations in damage evolution implementation, leading to numerical convergence problems.

8.5.6. Conclusion

The comparative analysis of VCCT, XFEM (QUADS Criterion), and XFEM (MAXPS Criterion) models offers crucial insights into their applicability for predicting the behaviour of stiffened panels in the post-buckling domain. Skin-stringer separation analysis exposes challenges in predicting crack length for all models, with VCCT providing the closest approximation. The observed discrepancies in the case of XFEM techniques emphasise the importance of incorporating experimentally obtained nominal stress values to model damage initiation. In general, however, the STATUSXFEM contours captured from finite element models reveal the prediction of a three-dimensional crack along the interface section. This highlights the potential of the XFEM technique over the VCCT-based model, which models the skin-stringer separation as a two-dimensional fracture surface. Regarding computational efficiency, VCCT and XFEM (QUADS Criterion) demonstrated comparable results, with XFEM introducing a marginal increase in computation time. Numerical stability discussions reveal robust performance from VCCT and XFEM (QUADS Criterion) models. In contrast, XFEM (MAXPS Criterion) faces challenges such as crack tip impingement and limitations in damage evolution, impacting its stability. While a workaround was implemented using the UDMGINI subroutine for this thesis study, the fracture plane used to model cracks is not solution-based and is pre-defined by the user. Developing a physics-based solution is necessary to overcome the challenges of the Abaqus implementation. However, this was out of the scope of this thesis study and could potentially be focused on in future studies.

Part IV

Conclusion and Recommendations

9

Conclusion

This thesis study investigated whether the XFEM damage modelling technique can accurately and efficiently model the skin-stringer separation behaviour in a butt-joint PEKK-FC thermoplastic stiffened panel. The stiffened panel under consideration was chosen from the literature where the authors tested two PEKK-FC thermoplastic stiffened panels with three stringers and a 70 mm initial debond at the skin-stringer interface. The authors also created a VCCT-based model. Hence, for this thesis study, the VCCT-based model was replicated and considered for comparison with XFEM. The investigation was done in two stages. First, to become familiar with the damage modelling techniques of VCCT and XFEM, simple DCB specimen models were constructed and analysed using the geometric, material and fracture properties reported in the characterisation study performed by Tijs et al. [55]. Based on the experience gained by creating coupon-level models, multi-stringer thermoplastic stiffened panel models were created using the panel specifications reported by Dooren et al. [50].

The modelling exercise involving the DCB specimens provided key insights into the characteristics of the damage modelling techniques of VCCT and XFEM. It must be noted that the MAXPS criterion was used to define damage initiation in the XFEM-based DCB model. The key findings are outlined below:

1. Both techniques replicated the rounding of the delamination front, which is observed in experimental test coupons. In the case of VCCT, the rounding of the delamination front is enabled by using the RAMP release option. Although there is no equivalent option in the case of the XFEM technique, the observed rounding of the delamination front is due to the nature of the stress state along the width of the specimen. Near the centre of the width of the specimen, the plane strain condition dominates the stress state, while near the free edges of the DCB specimen, the plane stress condition dominates the stress state. The resultant plastic zone ahead of the crack tip is larger in the case of the plane stress condition when compared to the plane strain condition. A larger plastic zone limits the crack growth behaviour. Hence, the crack growth near the free edges tends to be slower than the specimen's centre. Since the XFEM technique considers the stress in the enriched elements for damage initiation and evolution, the rounding of the delamination front is replicated.
2. Upon examining the load-displacement curves obtained, it was observed that both damage modelling techniques exhibited small oscillations. These oscillations are a consequence of the way in which these techniques model damage evolution. In the case of VCCT, the bond is gradually released from one boundary of the element to the other when the fracture criterion is met. In contrast, when the damage initiation criterion is met in XFEM, a crack is initiated while the element's stiffness is degraded based on a traction separation law. In both cases, the resulting damage evolution behaviour results in a slight stiffness mismatch in the non-linear region where quasi-static delamination occurs.
3. The VCCT-based model predicted the specimen behaviour without any issues. However, the XFEM model faced challenges due to its current implementation in Abaqus, which can only model cracks through solid-brick elements. This necessitated the introduction of an interface section with matrix properties between the two beam sections. The thickness of this interface section significantly influenced the predicted load-displacement behaviour.
4. In section 6.3, it was noted that the XFEM model took 2.723 times more CPU time than the VCCT-based model. The VCCT-based model predicted the delamination along the interface between the two beam sections, i.e. along a predetermined fracture plane. On the other hand, the XFEM-CZM model could predict the delamination growth along a solution-based crack path. However, the resultant crack path was straight along the DCB specimen's length because a pure mode 1 fracture is present in the DCB

specimen. Therefore, the added computational expense was considered unnecessary in the case of the DCB specimen, and it was concluded that a VCCT-based model would be sufficient for this particular case.

While the use of the XFEM technique was considered to be overkill in the case of a DCB specimen, it was still considered to be useful in modelling the skin-stringer separation behaviour in the multi-stringer thermoplastic stiffened panel where a mixed mode fracture is expected to occur. After learning how to construct models using VCCT and XFEM damage modelling techniques, multi-stringer panels were modelled. The results of the finite element models and test panels 1 and 2 will help answer the main and sub-research questions. To answer the main research question, the sub-questions must be tackled first, as outlined below:

1. **Does using XFEM to model skin-stringer separation behaviour influence the prediction of post-buckling deformations and the final failure load?**

   Both the VCCT and XFEM models were able to accurately predict the initial buckling mode shape of three half-waves in each skin bay, including their shape and position. However, as the loads increased, the models predicted the formation of a fourth half-wave in a different location than what was observed in the test panels. This could be associated with the geometric imperfections introduced to the models and the discrepancy between the skin layup used in the models and the actual layup used in the test panels. Furthermore, at higher loads, the upper outwards half-wave on the right bay differed when comparing the VCCT and XFEM-based models. Therefore, in conclusion, it can be said that the method used to model the damage had a minimal effect on the post-buckling deformations.

   In terms of the final failure load, both the VCCT and XFEM (QUADS Criterion) models predicted similar loads of 226.57 kN and 225.239 kN, respectively, which were slightly higher than the final failure loads of test panels 1 and 2 (223 kN and 225.90 kN respectively). However, the XFEM (MAXPS Criterion) model significantly over-predicted the final failure load at 245.795 kN. Judging by the observed crack length evolution curves, it is evident that the final failure occurs when the unstable crack growth occurs (indicated by a spike in the crack length). This depends on the technique used to evaluate damage along the skin-stringer interface.

2. **Considering the focus on the thermoplastic stiffened panel examined by Dooren et al. and noting the authors used VCCT to model skin-stringer separation behaviour in their study, how does the predicted skin-stringer separation behaviour using XFEM compare with that obtained through the VCCT model?**

   This thesis study used the XFEM technique to model the skin-stringer separation in combination with the QUADS and MAXPS damage initiation criteria. The damage modelling techniques could predict the semi-elliptical shape of the damage at the skin-stringer interface, similar to the VCCT-based model. However, the models showed differences in crack length evolution curves.

   Firstly, it was observed that the XFEM-based models underestimated crack growth behaviour compared to the VCCT-based model. Secondly, the crack length at the final failure load for test panels 1 and 2 was 196.5 mm. However, the VCCT-based model predicted it to be 178 mm, an under-prediction. Furthermore, the XFEM-based models showed an even greater underestimation of the crack length at the final failure load. The XFEM (QUADS Criterion) model predicted it to be 144.5 mm, and the XFEM (MAXPS Criterion) model predicted it to be 169.8 mm. Thirdly, the XFEM (QUADS Criterion) model predicted a spike in the crack length curve beyond the final failure load, which indicates unstable crack growth. The VCCT-based model also showed unstable crack growth. On the other hand, the XFEM (MAXPS Criterion) model had relatively slower unstable crack growth. This could be due to the use of a user-defined fracture plane. These differences in the crack-length evolution curves could be associated with the assumption made in the case of the damage initiation parameters used to define the XFEM models. This was done due to the lack of experimentally obtained parameters for the PEKK-SFRP material used in the butt-joint filler.

   Compared to the VCCT-based model, where the skin-stringer separation was limited to a 2D interface between the butt-joint filler and the skin, the XFEM-based models could model a complex three-dimensional fracture surface. This offers more insights into the crack growth behaviour at the skin-stringer interface compared to the VCCT-based model.

3. **How does the computational efficiency of XFEM compare to that of VCCT?**

   It was found that the XFEM technique is more computationally expensive than VCCT. This is due to using a relatively finer mesh and the additional degrees of freedom in the enriched region, which increases the number of unknowns in the system of equations and requires more computational resources to obtain a solution. When the CPU time of the VCCT and XFEM (QUADS Criterion) models with similar meshes was compared, the CPU time of the XFEM model was found to be 28.86% higher than the VCCT-based model. However, the increase in the computational cost can be minimised by using smarter meshing techniques. It can be done by assigning a finer mesh in the critical regions where the skin-stringer separation is expected while using a relatively coarser mesh in the non-critical regions. Doing so, it was observed that the CPU time of the XFEM (QUADS Criterion) based model was only 1.2% higher than the VCCT-based model. In contrast, the CPU time observed for the XFEM (MAXPS Criterion) model was 46.74% higher than the VCCT-based model. This could be associated with the higher failure load and the numerical instabilities while modelling damage using XFEM (MAXPS Criterion).

4. **How do the XFEM and VCCT damage modelling tools, as implemented in Abaqus, compare in terms of ease of use for the user?**

   Based on modelling experience and challenges faced while creating finite element models using damage modelling techniques of VCCT, XFEM (QUADS Criterion), and XFEM (MAXPS Criterion), the VCCT and XFEM (QUADS Criterion) were found to be very reliable and did not present any challenges during the analysis. However, the implementation of XFEM (MAXPS Criterion) in Abaqus had two key limitations. Firstly, it presented the issue of crack tip impingement at the surface of the enriched section. Secondly, when the crack tip reached the bottom or top surface of the enriched section, it was found that the model could not predict further crack growth or the initiation of a new crack. A user-defined damage initiation criterion was introduced using the UDMGINI subroutine to overcome this issue. When modifying the fracture plane in the UDMGINI subroutine, using a bias factor or a crack tip deflection strategy, the resultant complex crack front resulted in errors when the complex crack front was supposed to merge at a certain element. In contrast, using a pre-defined fracture plane along the length of the panel, similar to the definition in the QUADS criterion, proved to be an effective strategy that overcame challenges posed by the implementation in Abaqus. However, the implementation of the XFEM (MAXPS Criterion) algorithm in Abaqus is not reliable in the case of mix-mode fracture, as found in the Multi-Stringer panel analysis part of this thesis project. In the case of pure mode 1 fracture, it can provide acceptable results, although the challenges related to numerical convergence are still present, as was reported in the DCB Specimen Analysis part of this thesis.

Having answered the sub-research questions, the primary research question: "Can the XFEM damage modelling technique accurately and efficiently model the skin-stringer separation behaviour in a Butt-Joined PEKK-FC thermoplastic stiffened panel?" can now be addressed. When the XFEM damage modelling technique is paired with the QUADS damage initiation criterion, it proves efficient in modelling the skin-stringer separation behaviour in a butt-joined PEKK-FC thermoplastic stiffened panel. However, judging the model's accuracy is complex and depends on several factors. In the case of test panels 1 and 2, the damage evolution at the skin-stringer interface involves skin deformation and debonding of the butt-joint filler from the skin surface. It was noted that parts of the filler remained attached to the skin surface post-separation, indicating that the cracks traversed the filler material. The finite element analysis results depend on the assumptions made during the model definition. For the XFEM (QUADS Criterion) model, it was assumed that the crack would grow only within a section of the filler material, implying that the bond at the interface between the skin and the filler remains undamaged. Another assumption was made when defining the damage initiation parameters for the quadratic stress criterion. Due to the lack of test data for the PEKK SFRP material, the values reported for PEKK-FC material were used based on the characterisation study by Tijs et al. [55]. The resultant crack length at the final failure load (144.5 mm) was lower than the test panels (196.5 mm). This discrepancy could be due to the assumptions made for the damage initiation parameters and the absence of skin-delamination and debond between the filler and the skin within the resultant models. Despite these limitations, the model could predict the load-displacement curve of the stiffened panels and estimate the final failure load fairly accurately. It's important to note that the observed final failure load and the crack length can vary between test panels in real life due to geometric imperfections and manufacturing defects. From a structural design perspective, the XFEM (QUADS Criterion) model can provide reliable insights into the post-buckling behaviour of the stiffened panels under consideration.

When the XFEM damage modelling technique is combined with the MAXPS damage initiation criterion, issues related to crack tip impingement and numerical convergence are observed with the Abaqus algorithm implementation. For this study, a workaround was introduced by pre-defining the fracture plane along the length of the panel, but it hasn't been scientifically validated against experimental data. In this case, the Abaqus algorithm did not accurately and efficiently model the skin-stringer separation behaviour in a butt-joined PEKK-FC thermoplastic stiffened panel. This leaves room for developing a user-subroutine for the MAXPS damage initiation criterion, which can overcome the limitations of the Abaqus algorithm while being based on scientific theory and extensively validated. Until then, the XFEM (QUADS Criterion) damage model offers a commercially available interim solution. It's important to note that while it models crack growth in a 3D fracture plane, it does not completely define it along a solution-based direction.

10

Recommendations

This thesis focused on developing finite element models using the commercial implementation of XFEM in Abaqus. Through this process, the advantages and disadvantages associated with the Abaqus algorithm were highlighted. One of the major disadvantages was related to the problems that crack tip impingement faced at the stiffened panel's multi-material interface. Given the timeline of the master thesis, it was not possible to evaluate every idea to tackle this problem. Therefore, four recommendations were framed based on the learnings from this thesis study. These recommendations are listed below and could serve as a guide for future projects.

1. Throughout this thesis study, one of the main challenges encountered was related to the limitations in implementing the XFEM (MAXPS Criterion) in Abaqus. Among the damage initiation criteria available in Abaqus, only the MAXPS criterion showed potential for determining the fracture plane independent of any user-defined bias. However, it was not suitable when modelling mixed-mode fracture. As a proof of concept, during this thesis study, the UDMGINI subroutine was used to introduce a user-defined damage initiation criterion. This demonstrated the potential for developing a better algorithm for the maximum principal stress criterion that can account for the location of the crack tip within the interface section while being based on scientific theory. Future studies could also explore the development of a UDMGINI subroutine based on a different damage initiation criterion, such as the maximum energy dissipation criterion. Furthermore, Ponnusamia et al. successfully demonstrated crack deflection behaviour in the presence of particles ahead of the crack tip in a matrix using a 2D model [66]. This study could serve as a starting point and could be extended for 3D applications in future studies.
2. There is a lack of experimentally determined critical stress values that are used to define the initiation of damage in the PEKK SFRP filler material. This could be one of the reasons why the crack length along the skin-stringer interface is underestimated. To model the damage in the butt-joint material using XFEM, it is crucial that a series of experiments be carried out in the future to determine the damage initiation parameters experimentally.
3. The current implementation of XFEM in Abaqus limits the crack growth within a solid interface. As observed with test panels 1 and 2, the creation of delamination between the skin and the butt-joint filler is also a likely scenario in the case of skin-stringer separation. Future studies could focus on modelling the behaviour of skin-stringer separation by investigating the potential of modelling debonding along the interface, along with the crack growth within the solid section. A potential starting point for this could be introducing a cohesive contact at the interface and developing a model that creates an interaction between the damage modelled using XFEM and the debond predicted using the cohesive contact.
4. Lastly, the delamination within the skin was completely ignored for the models created during this thesis study. It could be interesting to add cohesive elements between the skin plies to model damage not just at the skin stringer interface but also within the skin sections.

References

1. Orifici, A. C., De Zarate Alberdi, I. O., Thomson, R. S. & Bayandor, J. Compression and post-buckling damage growth and collapse analysis of flat composite stiffened panels. Composites Science and Technology **68,** 3150–3160. `https://doi.org/10.1016/j.compscitech.2008.07.017` (Dec. 2008).
2. Marsh, G. Airbus takes on Boeing with reinforced plastic A350 XWB. Reinforced Plastics **51,** 26–29. `https://doi.org/10.1016/s0034-3617(07)70383-1` (Dec. 2007).
3. Barile, M., Lecce, L., Iannone, M., Pappadà, S. & Roberti, P. Thermoplastic composites for aerospace applications 87–114. `https://doi.org/10.1007/978-3-030-35346-9_4` (Jan. 2020).
4. Offringa, A., Van Ingen, J. & Buitenhuis, A. Butt-joined, thermoplastic stiffened-skin concept development. SAMPE Journal **48,** 7–15 (2012).
5. Van Ingen, J. Thermoplastic orthogrid fuselage shell. Sampe J **52,** 7–15 (2016).
6. Tijs, B. et al. Virtual testing of thermoplastic composites: towards a hybrid simulation-physical testing pyramid in ECCM18-18th European Conference on Composite Materials, Athens, Greece (2018), 24–28.
7. Ahmed, T., Stavrov, D., Bersee, H. & Beukers, A. Induction welding of thermoplastic composites—an overview. Composites Part A: Applied Science and Manufacturing **37,** 1638–1651. `https://doi.org/10.1016/j.compositesa.2005.10.009` (Oct. 2006).
8. Pappadà, S. et al. Fabrication of a thermoplastic matrix composite stiffened panel by induction welding. Aerospace Science and Technology **43,** 314–320. `https://doi.org/10.1016/j.ast.2015.03.013` (June 2015).
9. Teplyk, Y., Hapon, V. & Tuz, M. Thermoplastic materials-a new stage in the life of aircraft construction. Proceedings of National Aviation University **84** (2020).
10. Arnt, O., van Ingen, J. & Buitenhuis, A. Development of a butt jointed thermoplastics stiffened shin concept in Proceedings of the SAMPE Conference, Long Beach, CA, USA (2011), 23–26.
11. Van Ingen, J. W., Lantermans, P. & Lippers, I. Impact behaviour of a butt jointed thermoplastic stiffened skin panel in SAMPE International Symposium and Exhibition, Baltimore, United States (2012).
12. Sudhin, A., Remanan, M., Ajeesh, G. & Jayanarayanan, K. Comparison of properties of carbon fiber reinforced thermoplastic and thermosetting composites for aerospace applications. Materials Today: Proceedings **24,** 453–462. `https://doi.org/10.1016/j.matpr.2020.04.297` (Jan. 2020).
13. Yap, J. W., Scott, M., Thomson, R. S. & Hachenberg, D. The analysis of skin-to-stiffener debonding in composite aerospace structures. Composite Structures **57,** 425–435. `https://doi.org/10.1016/s0263-8223(02)00110-1` (July 2002).
14. Kong, C.-W., Lee, I.-C., Kim, C.-G. & Hong, C. S. Postbuckling and failure of stiffened composite panels under axial compression. Composite Structures **42,** 13–21. `https://doi.org/10.1016/s0263-8223(98)00044-0` (May 1998).
15. Dávila, C. G. & Bisagni, C. Fatigue life and damage tolerance of postbuckled composite stiffened structures with initial delamination. Composite Structures **161,** 73–84. `https://doi.org/10.1016/j.compstruct.2016.11.033` (Feb. 2017).
16. Kootte, L. J. & Bisagni, C. A methodology to investigate Skin-Stringer separation in postbuckled composite stiffened panels. AIAA Scitech 2020 Forum. `https://doi.org/10.2514/6.2020-0477` (Jan. 2020).
17. Turón, A., González, E., Sarrado, C., Guillamet, G. & Maimí, P. Accurate simulation of delamination under mixed-mode loading using a cohesive model with a mode-dependent penalty stiffness. Composite Structures **184,** 506–511. `https://doi.org/10.1016/j.compstruct.2017.10.017` (Jan. 2018).
18. Vescovini, R., Dávila, C. G. & Bisagni, C. Failure analysis of composite multi-stringer panels using simplified models. Composites Part B: Engineering **45,** 939–951. `https://doi.org/10.1016/j.compositesb.2012.07.030` (Feb. 2013).

19. Gao, S.-L. & Kim, J. K. Cooling rate influences in carbon fibre/PEEK composites. Part II: interlaminar fracture toughness. Composites Part A: Applied Science and Manufacturing **32,** 763–774. https://doi.org/10.1016/s1359-835x(00)00188-3 (June 2001).

20. Lee, W. I., Talbott, M. F., Springer, G. Ś. & Berglund, L. A. Effects of cooling rate on the crystallinity and mechanical properties of thermoplastic composites. Journal of Reinforced Plastics and Composites **6,** 2–12. https://doi.org/10.1177/073168448700600101 (Jan. 1987).

21. Rybicki, E. & Kanninen, M. F. A finite element calculation of stress intensity factors by a modified crack closure integral. Engineering Fracture Mechanics **9,** 931–938. https://doi.org/10.1016/0013-7944(77)90013-3 (Jan. 1977).

22. Rybicki, E., Schmueser, D. & Fox, J. An energy release rate approach for stable crack growth in the Free-Edge delamination problem. Journal of Composite Materials **11,** 470–487. https://doi.org/10.1177/002199837701100409 (Oct. 1977).

23. Baran, İ., Warnet, L. & Akkerman, R. Assessment of failure and cohesive zone length in co-consolidated hybrid C/PEKK butt joint. Engineering Structures **168,** 420–430. https://doi.org/10.1016/j.engstruct.2018.04.089 (Aug. 2018).

24. Yap, J. W., Thomson, R. S., Scott, M. & Hachenberg, D. Influence of post-buckling behaviour of composite stiffened panels on the damage criticality. Composite Structures **66,** 197–206. https://doi.org/10.1016/j.compstruct.2004.04.038 (Oct. 2004).

25. Benzeggagh, M. & Kenane, M. Measurement of mixed-mode delamination fracture toughness of unidirectional glass/epoxy composites with mixed-mode bending apparatus. Composites Science and Technology **56,** 439–449. https://doi.org/10.1016/0266-3538(96)00005-x (Jan. 1996).

26. Standard test method for mode I interlaminar fracture toughness of unidirectional fiber-reinforced polymer matrix composites (ASTM International, 2007).

27. Davidson, B. D., Sun, X. & Vinciquerra, A. J. Influences of Friction, Geometric Nonlinearities, and Fixture Compliance on Experimentally Observed Toughnesses from Three and Four-point Bend End-notched Flexure Tests. Journal of Composite Materials **41,** 1177–1196. https://doi.org/10.1177/0021998306067304 (May 2007).

28. Standard test method for mixed mode I-mode II interlaminar fracture toughness of unidirectional fiber reinforced polymer matrix composites (ASTM International, 2006).

29. Krueger, R. An Approach to Assess Delamination Propagation Simulation Capabilities in Commercial Finite Element Codes. Technical report, NASA. https://ntrs.nasa.gov/api/citations/20080015439/downloads/20080015439.pdf (Apr. 2008).

30. Reeder, J. R. 3D mixed-mode delamination fracture criteria - An experimentalist's perspective in American Society for Composites 21st Annual Technical Conference (2006).

31. Xu, J., Zhao, Q. & Qiao, P. A critical review on buckling and post-buckling analysis of composite structures. Frontiers in Aerospace Engineering **2,** 157 (2013).

32. Bertolini, J., Castanié, B., Barrau, J.-J. & Navarro, J.-P. Multi-level experimental and numerical analysis of composite stiffener debonding. Part 1: Non-specific specimen level. Composite Structures **90,** 381–391. https://doi.org/10.1016/j.compstruct.2009.04.001 (Oct. 2009).

33. Bertolini, J., Castanié, B., Barrau, J.-J., Navarro, J.-P. & Petiot, C. Multi-level experimental and numerical analysis of composite stiffener debonding. Part 2: Element and panel level. Composite Structures **90,** 392–403. https://doi.org/10.1016/j.compstruct.2009.04.002 (Oct. 2009).

34. Kolanu, N. R., Raju, G. & Ramji, M. A unified numerical approach for the simulation of intra and inter laminar damage evolution in stiffened CFRP panels under compression. Composites Part B: Engineering **190,** 107931. https://doi.org/10.1016/j.compositesb.2020.107931 (June 2020).

35. Orifici, A. C. et al. Degradation investigation in a postbuckling composite stiffened fuselage panel. Composite Structures **82,** 217–224. https://doi.org/10.1016/j.compstruct.2007.01.012 (Jan. 2008).

36. Masood, S., Gaddikeri, K. M. & Viswamurthy, S. R. Experimental and finite element numerical studies on the post-buckling behavior of composite stiffened panels. Mechanics of Advanced Materials and Structures, 1–14. https://doi.org/10.1080/15376494.2019.1701151 (Dec. 2019).

37. Ye, Y., Zhu, W., Jiang, J., Xu, Q. & Ke, Y. Computational modelling of postbuckling behavior of composite T-stiffened panels with different bonding methods. Composites Part B: Engineering **166,** 247–256. https://doi.org/10.1016/j.compositesb.2018.11.137 (June 2019).

38. Riccio, A., Raimondo, A., Di Felice, G. & Scaramuzzino, F. A numerical procedure for the simulation of skin–stringer debonding growth in stiffened composite panels. Aerospace Science and Technology **39,** 307–314. https://doi.org/10.1016/j.ast.2014.10.003 (Dec. 2014).

39. Moës, N., Dolbow, J. E. & Belytschko, T. A finite element method for crack growth without remeshing. International Journal for Numerical Methods in Engineering **46,** 131–150. https://doi.org/10.1002/(sici)1097-0207(19990910)46:1%3C131::aid-nme726%3E3.0.co;2-j (Sept. 1999).

40. Systemes, D. ABAQUS/Standard User's Manual, Version 6.9. Abaqus/Standard User's Manual (2017).

41. Ventura, G. & Benvenuti, E. Equivalent polynomials for quadrature in Heaviside function enriched elements. International Journal for Numerical Methods in Engineering **102,** 688–710. https://doi.org/10.1002/nme.4679 (May 2014).

42. Bisagni, C., Brambilla, P. & Bavila, C. G. Modeling Delamination in Postbuckled Composite Structures Under Static and Fatigue Loads. Technical Report, NASA. https://ntrs.nasa.gov/api/citations/20130013696/downloads/20130013696.pdf (May 2013).

43. Raimondo, A., Doesburg, S. & Bisagni, C. Numerical study of quasi-static and fatigue delamination growth in a post-buckled composite stiffened panel. Composites Part B: Engineering **182,** 107589. https://doi.org/10.1016/j.compositesb.2019.107589 (Feb. 2020).

44. Tong, L. An assessment of failure criteria to predict the strength of adhesively bonded composite double lap joints. Journal of Reinforced Plastics and Composites **16,** 698–713. https://doi.org/10.1177/073168449701600803 (May 1997).

45. Hashin, Z. Fatigue failure criteria for unidirectional fiber composites. Journal of Applied Mechanics **48,** 846–852. https://doi.org/10.1115/1.3157744 (Dec. 1981).

46. Zou, D. & Bisagni, C. Study of skin-stiffener separation in T-stiffened composite specimens in post-buckling condition 2 (2018).

47. Riccio, A., Raimondo, A. & Scaramuzzino, F. A robust numerical approach for the simulation of skin–stringer debonding growth in stiffened composite panels under compression. Composites Part B: Engineering **71,** 131–142. https://doi.org/10.1016/j.compositesb.2014.11.007 (Mar. 2015).

48. Riccio, A., Russo, A., Raimondo, A. & Sellitto, A. A numerical assessment of fibre bridging influence on composite panels Skin-stringer debonding. Procedia Engineering **167,** 56–63. https://doi.org/10.1016/j.proeng.2016.11.669 (Jan. 2016).

49. Tamužs, V., Tarasovs, S. & Vilks, U. K. Progressive delamination and fiber bridging modeling in double cantilever beam composite specimens https://doi.org/10.1016/s0013-7944(00)00131-4 (Mar. 2001).

50. Van Dooren, K., Tijs, B., Waleson, J. & Bisagni, C. Skin-stringer separation in post-buckling of butt-joint stiffened thermoplastic composite panels. Composite Structures **304,** 116294. https://doi.org/10.1016/j.compstruct.2022.116294 (Jan. 2023).

51. Bisagni, C. & Dávila, C. G. Experimental investigation of the postbuckling response and collapse of a single-stringer specimen. Composite Structures **108,** 493–503. https://doi.org/10.1016/j.compstruct.2013.09.018 (Feb. 2014).

52. Action, J., Leone, F. A. & De Carvalho, N. Progressive damage analysis of a Multi-Stringer Post-Buckled panel. AIAA Scitech 2020 Forum. https://doi.org/10.2514/6.2020-1481 (Jan. 2020).

53. Šedek, J., Vlach, J. & Růžek, R. Analysis of Compressive Behaviour of Pristine and Cracked 5-Stringer Butt-Joint Panels Made from Carbon Fibre Reinforced Thermoplastic Polymer. Procedia Structural Integrity **42,** 398–403. https://doi.org/10.1016/j.prostr.2022.12.050 (Jan. 2022).

54. Wang, B., Chen, X., Wang, W., Yang, J. & Zhang, R. Post-buckling failure analysis of composite stiffened panels considering the mode III fracture. Journal of Composite Materials **56,** 3099–3111. https://doi.org/10.1177/00219983221109946 (June 2022).

55. Tijs, B., Abdel-Monsef, S., Renart, J., Turón, A. & Bisagni, C. Characterization and analysis of the interlaminar behavior of thermoplastic composites considering fiber bridging and R-curve effects. Composites Part A: Applied Science and Manufacturing **162,** 107101. `https://doi.org/10.1016/j.compositesa.2022.107101` (Nov. 2022).

56. Hashemi, S., Kinloch, A. J. & Williams, J. The analysis of interlaminar fracture in uniaxial fibre-polymer composites. Proceedings of the Royal Society of London **427,** 173–199. `https://doi.org/10.1098/rspa.1990.0007` (Jan. 1990).

57. Nassir, N. et al. The perforation resistance of glass fibre reinforced PEKK composites. Polymer Testing **72,** 423–431. `https://doi.org/10.1016/j.polymertesting.2018.11.007` (Dec. 2018).

58. Campilho, R., Banea, M. D., Pinto, A. M. G., Da Silva, L. F. M. & De Jesus, A. M. Strength prediction of single- and double-lap joints by standard and extended finite element modelling. International Journal of Adhesion and Adhesives **31,** 363–372. `https://doi.org/10.1016/j.ijadhadh.2010.09.008` (July 2011).

59. Campilho, R., Banea, M. D., Chaves, F. J. P. & Da Silva, L. F. M. eXtended Finite Element Method for fracture characterization of adhesive joints in pure mode I. Computational Materials Science **50,** 1543–1549. `https://doi.org/10.1016/j.commatsci.2010.12.012` (Feb. 2011).

60. Campilho, R., Banea, M. D., Neto, J. & Da Silva, L. F. M. Modelling adhesive joints with cohesive zone models: effect of the cohesive law shape of the adhesive layer. International Journal of Adhesion and Adhesives **44,** 48–56. `https://doi.org/10.1016/j.ijadhadh.2013.02.006` (July 2013).

61. Fernandes, T. A., Campilho, R., Banea, M. D. & Da Silva, L. F. M. Adhesive selection for single lap bonded joints: experimentation and advanced techniques for strength prediction. Journal of Adhesion **91,** 841–862. `https://doi.org/10.1080/00218464.2014.994703` (Jan. 2015).

62. Stuparu, A. et al. Cohesive and XFEM evaluation of adhesive failure for dissimilar single-lap joints. Procedia Structural Integrity **2,** 316–325. `https://doi.org/10.1016/j.prostr.2016.06.041` (Jan. 2016).

63. Stuparu, A., Constantinescu, D. M., Apostol, D. A. & Sandu, M. A Combined Cohesive Elements—XFEM approach for analyzing crack propagation in bonded joints. Journal of Adhesion **92,** 535–552. `https://doi.org/10.1080/00218464.2015.1115355` (Nov. 2015).

64. Mubashar, A., Ashcroft, I. & Crocombe, A. Modelling damage and failure in adhesive joints using a combined XFEM-Cohesive element methodology. Journal of Adhesion **90,** 682–697. `https://doi.org/10.1080/00218464.2013.826580` (Apr. 2014).

65. Stein, N., Dölling, S., Chalkiadaki, K., Becker, W. & Weißgraeber, P. Enhanced XFEM for crack deflection in multi-material joints. International Journal of Fracture **207,** 193–210. `https://doi.org/10.1007/s10704-017-0228-9` (July 2017).

66. Ponnusami, S. A., Krishnasamy, J., Turteltaub, S. & Van Der Zwaag, S. Elucidating the effect of cohesive zone length in fracture simulations of particulate composites. Engineering Fracture Mechanics **268,** 108431. `https://doi.org/10.1016/j.engfracmech.2022.108431` (June 2022).